Structure and function study of HCN1 channel by forming a lattice on the membrane

Dissertation

zur Erlangung des Doktorgrades (MN/PhD)

der Medizinischen Fakultät

der Rheinischen Friedrich-Wilhelms-Universität

Bonn

Jianqing Li

Aus Hubei, China

2020

Angefertigt mit der Genehmigung

der Medizinischen Fakultät der Universität Bonn

1. Gutachter: Prof. Dr. Heinz Beck
2. Gutachter: Prof. Ulrich Benjamin Kaupp

Tag der Mündlichen Prüfung: 17.08.2020

Aus der Institut für Experimentelle Epileptologie und Kognitionswissenschaften

Direktor: Prof. Dr. Heinz Beck

Index

List of abbreviations

2D	two dimension
3D	three dimension
cAMP	cyclic adenosine 3′, 5′-monophosphate
CLEM	correlative light and electron microscopy
CNBD	cyclic nucleotide-biding domain
cryo-EM	cryo-electron microscopy
cryo-ET	cryo-electron tomography
CTF	contrast transfer function
DMSO	dimethyl sulfoxide
DMEM	Dulbecco's modified Eagle medium
EGFP	enhanced green fluorescent protein
EM	electron microscopy
ET	electron tomography
EPSPs	excitatory postsynaptic potentials
FIB	focused ion beam
fLM	fluorescent light microscopy
FM	fluorescence microscopy
GFP	green fluorescent protein
h	hour
HCN	hyperpolarization-activated cyclic nucleotide-gated
Int_C	intein C
Int_N	intein N
LCP	lipidic-cubic phase
min	minute
MD	molecular dynamics
NMR	nuclear magnetic resonance
PBS	phosphate-buffered saline
PDB	protein data bank
PFA	paraformaldehyde
QD	quantum dot

ROI	region of interest
RT	room temperature
S	second
SBDD	structure-based drug design
SE	status epilepticus
SIRT	simultaneous iterative reconstruction technique
SNR	signal-to-noise ratio
sfGFP	superfolder GFP
spGFP	split GFP
ssNMR	solid-state NMR
TEM	transmission electron microscopy
WT	wild-type
v/v	volume per volume
w/v	weight per volume
w/w	weight per weight

1. Introduction

1.1. HCN channel

1.1.1. Biophysical properties of HCN channels

Hyperpolarization-activated cyclic nucleotide-gated (HCN) channels are members of the voltage-gated pore-loop channels superfamily (**Figure 1.1a**). They are characterized by activation upon membrane hyperpolarization (Gauss et al., 1998; Ludwig et al., 1998; Santoro et al., 1998), and modulation by intracellular cyclic nucleotides, such as cyclic adenosine 3′, 5′-monophosphate (cAMP) (DiFrancesco and Tortora, 1991; Wang et al., 2002). In mammals, four subtypes of HCN channels (HCN1-4) have been identified to date (Ludwig et al., 1998), with distinct biophysical properties regarding voltage-dependence, activation kinetics, and cAMP modulation. These variable biophysical properties of subunits, together with distinct expression patterns, impart diverse biophysical characteristics of HCN channel current (I_h) in neurons, influencing a series of vital physiologic processes including neuronal pacemaking, dendritic integration, learning, and memory. Altered expression of HCN channels is associated with different neurological and psychological diseases including pain, addiction, and epilepsy (Du et al., 2013; Kim et al., 2012; Koga et al., 2015; Okamoto et al., 2006; Shin et al., 2006). Therefore, HCN channels are crucial potential drug targets for epilepsy and other neurological diseases.

HCN channels are formed as a tetramer of subunits, each compromising a transmembrane core and cytosolic C-terminal domain (**Figure 1.1b**), both modules cooperating allosterically during channel activation. The transmembrane core consists of six transmembrane segments (S1-S6), of which S1-S4 forms the voltage sensor, and S5–S6 forms the ion-conducting pore. Similar to other voltage-gated channels, in the S4 segment, there are positively charged residues (arginine or lysine) at every third position (Bezanilla, 2000; Chen et al., 2000; Jiang et al., 2003; Vaca et al., 2000). However, different from depolarization-activated channels, the inward movement of S4 charges in HCN channels leads to the opening of the channel. By introducing cysteine in the S4-S5 segment and C-linker of sea urchin sperm flagellar HCN, and thus locking the conformation by cysteine cross-linking, Prole and Yellen inferred a molecular coupling

mechanism as a possible explanation for this reverse voltage dependence of HCN channel (Prole and Yellen, 2006). Recent structural studies by Lee and MacKinnon further supported this hypothesis (Lee and MacKinnon, 2017). They hypothesized that the extraordinary size of S4, combined with the packed conformation of the S5-S6 helices, compress the pore in a closed state. When the membrane is hyperpolarized, the inward movement of S4 causes displacement of the S4-S5 linker, thus releasing the compression and pulling the pore open.

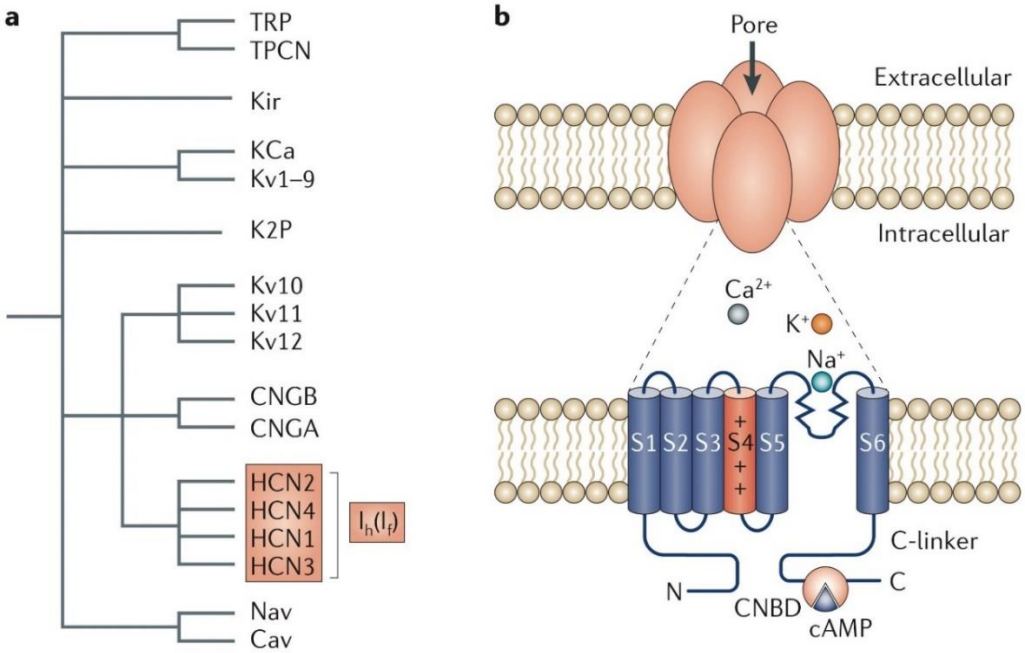

Figure 1.1 HCN channel: phylogenetic tree and transmembrane topology.

(a) A schematic phylogenetic tree representing the superfamily of pore-loop cation channels is shown, including HCN1-4 channels. (b) This diagram illustrates the transmembrane topology of HCN channels. Each subunit consists of six-transmembrane α-helices (S1-S6), with a positively-charged S4 transmembrane segment serving as the putative voltage sensor and a cyclic nucleotide-binding domain (CNBD) in the carboxyl terminus. Image from (Postea and Biel, 2011).

HCN channels open at membrane potentials more negative than -50 mV, and thus are active at normal resting membrane potentials of neurons (Shah, 2014), conducting Na^+ and K^+ ions with a ratio of 1:4 (Santoro et al., 1998). Although HCN channels contain a glycine-tyrosine-glycine (GYG) motif that confers the high selectivity for K^+ ions in potassium channels, they conduct both Na^+ and K^+ under physiological conditions. One speculation for the structural basis of sodium permeation is that the GYG motif is

coordinated less rigidly than in the K^+ channel (MacRi et al., 2012), thus allowing the entrance of cations of different sizes. Structural observations from cryo-electron microscopy (cryo-EM) studies showed that in the K^+ channel selectivity filter, all four sites were occupied, while in the HCN1 selectivity filter, only two out of four K^+ binding sites were occupied by K^+ ions (**Figure 1.2**), which allows Na^+ to penetrate the pore (Lee and MacKinnon, 2017). This observation may help to explain why HCN channels are permeable to both Na^+ and K^+ ions, even with the presence of the GYG motif.

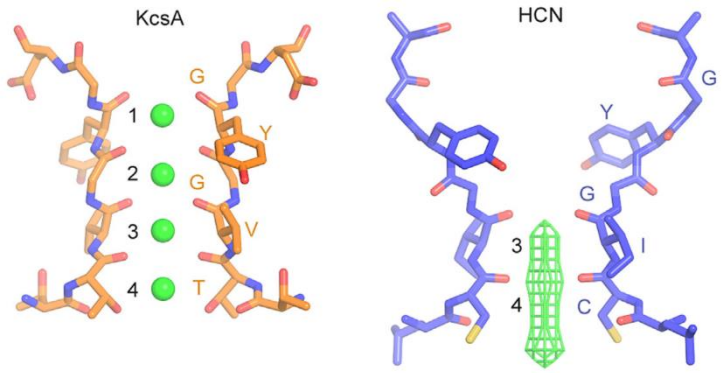

Figure 1.2 Selectivity filter structure of HCN1 channels.

Selectivity filter structures for the KscA channel (PDB: 1K4C) (left) and HCN1 channel (PDB: 5U6O) (right) are shown. Note that in the KscA selectivity filter, K^+ ions occupy all binding sites (1 to 4). The K^+ ions are represented as green spheres. In the HCN1 selectivity filter, only sites 3 and 4 are occupied. The density of K^+ ions is shown as green mesh. Image adapted from (Lee and MacKinnon, 2017)**.**

A cyclic nucleotide-biding domain (CNBD) is located at the intracellular C-terminus of HCN channels. cAMP enhances channel activity by alleviating tonic blocking by the C-linker-CNBD structure and shifts the voltage-dependent activation in depolarized direction (Craven and Zagotta, 2006; DiFrancesco and Tortora, 1991; Wahl-Schott and Biel, 2009). HCN channel subtypes are differently modulated by cAMP: while HCN2 and HCN4 exhibit strong cAMP-dependent changes in voltage-dependence and kinetics of activation, HCN1 and HCN3 are only weakly affected (Stieber et al., 2005; Ying et al., 2011; Zagotta et al., 2003). Three-dimensional (3D) structures of CNBD in the presence and absence of cAMP have demonstrated that cAMP binding can induce structural changes that may facilitate gate opening (Lee and MacKinnon, 2017; Zagotta et al., 2003) (**Figure 1.3**). However, in the absence of hyperpolarization, cAMP binding alone is not sufficient for channel opening.

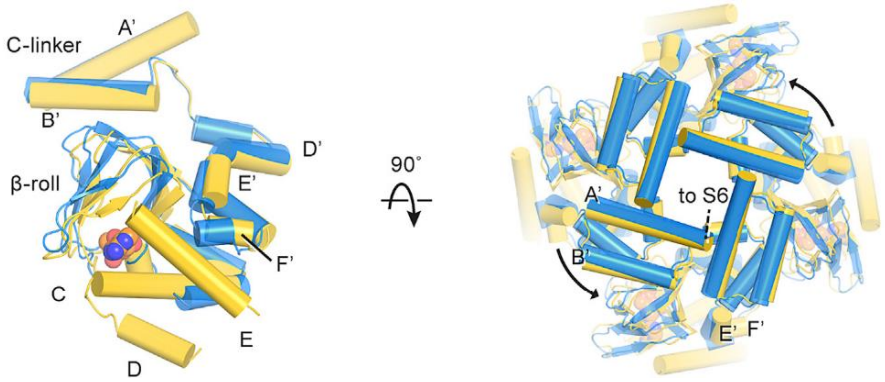

Figure 1.3 cAMP modulation of the HCN1 channel.

Superposition of C-linkers and CNBD in the cAMP-bound state (yellow) and the ligand-free state (blue) is presented. Left: only one subunit is shown for clarity. Right: the structure is viewed from the extracellular side. Image adapted from (Lee and MacKinnon, 2017)**.**

1.1.2. Physiological roles of HCN channels in Neurons

HCN channels are widely expressed in the peripheral and central nervous systems (Ding et al., 2016; Ludwig et al., 1998; Moosmang et al., 1999, 2001; Notomi and Shigemoto, 2004; Santoro et al., 1998). I_h, the inward current generated by HCN channels, has been shown to play diverse functional roles in determining resting membrane potential, action potential firing rate, dendritic integration, and synaptic transmission (He et al., 2014).

HCN channels are fractionally open at a voltage near the membrane potential and pass a depolarizing inward current (Lupica et al., 2001; Mesirca et al., 2014). These constitutively open HCN channels lower the membrane resistance (R_m) and exert a shunting effect on neuronal excitability: any given input current evokes a smaller change in membrane potential due to the presence of I_h. With membrane depolarization, the channels slowly inactivate and consequently cause a hyperpolarizing effect. Conversely, a hyperpolarizing input will activate HCN channels, generating a current that depolarizes the neuron back towards the resting membrane potential. This inherent negative-feedback property of HCN channels imparts a stabilizing effect on neuronal membrane potential. Altogether, the shunting and depolarizing properties of I_h contribute critically to the regulation of neuronal excitability in multiple ways, including affecting subthreshold

resonance, intrinsic oscillations, and synaptic integration (Biel et al., 2009; Robinson and Siegelbaum, 2003; Shah, 2014).

HCN channels are localized at a higher density in the apical dendrites than in the somas in the neocortical and hippocampal pyramidal neurons. This dendritic localization causes an additional inhibitory effect. The 'leak' currents conducted by HCN channels reduce the input resistance to the incoming synaptic inputs, leading to the decrease of the voltage change response to excitatory postsynaptic potentials (EPSPs), thus the ability of synaptic input to drive an action potential firing. Consequently, the effect of I_h is mixed: while the depolarizing properties of I_h on resting membrane potential promote hyperexcitability, the shunting effect produces an inhibitory effect on action potential firing. Several studies have shown that pharmacological blocking or genetic deletion of HCN channels results in increased excitability in neocortical and hippocampal pyramidal neurons (Berger et al., 2001; Poolos et al., 2002). However, in interneurons, the effect of I_h is predominantly excitatory, for instance, on the spontaneous firing of interneurons (Lupica et al., 2001).

Dendritic integration is a process critical for signal processing in neurons, in which multiple EPSPs must be temporally and spatially controlled to ensure high fidelity of information processing. The summation of incoming EPSPs is influenced mainly by the kinetic filtering of the dendrites, resulting in a slower rise and decay of distal EPSPs. However, in some neurons, including neocortical and hippocampal pyramidal neurons (Atherton et al., 2010), this localization dependence of temporal summation is not observed (**Figure 1.4**). The probable underlying mechanism is the somatodendritic gradient of I_h distribution in the dendrite, the density of which progressively increases with the distance from the soma. As a consequence, distal EPSPs decay faster as they spread from the site of initiation in the dendrite to the soma, resulting in almost equal temporal summation of all inputs at the soma (Williams and Stuart, 2000). Pharmacological blocking of HCN channels can restore distance-dependent time delays.

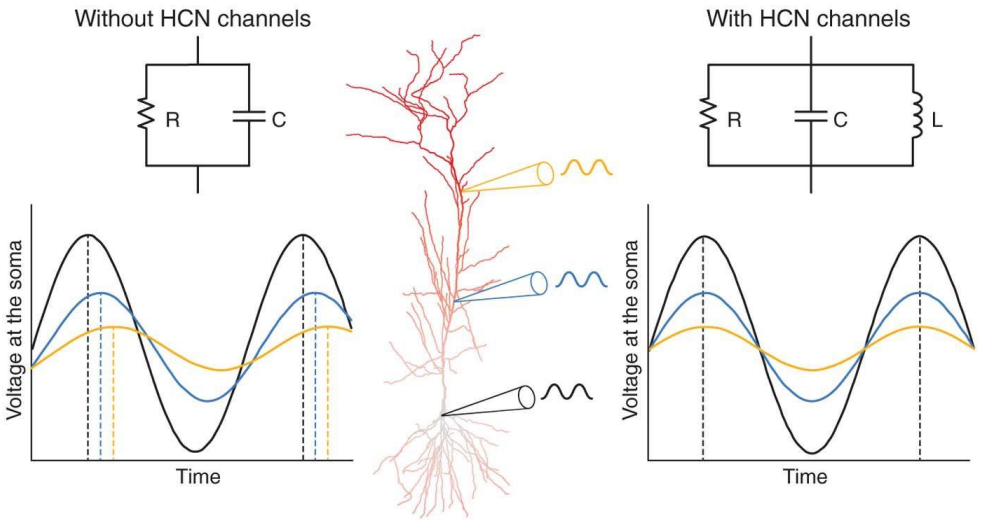

Figure 1.4 Effect of HCN channels on dendritic synchrony.

A schematic diagram shows that HCN channels contribute anomalous inductance (L) to the circuit of a CA1 pyramidal neuron. Oscillation signals are attenuated as they travel from different positions along the dendritic tree. In the presence of HCN channels, voltage response at the soma appeared almost synchronously. Color intensity represents HCN channel density along the dendrite. Image from (Williams, 2013).

The role of I_h for long-term synaptic plasticity was elucidated in brain areas such as CA1 pyramidal neurons (Nolan et al., 2005; Tsay et al., 2007). HCN1 channels have been found to function as a partial brake that constrains dendritic calcium spikes, thus constraining long-term potentiation and associated cognitive functions. Experiments on HCN1-KO mice showed improved hippocampal-dependent spatial learning and memory performance (Nolan et al., 2005; Wang et al., 2007). The mechanism behind this is the depolarizing effect of HCN channels on resting membrane potential. As the resting membrane potential becomes more positive by the activation of I_h, more voltage-gated T- and N-type channels are shifted to the inactivated states, thus reducing Ca^{2+} influx during calcium spikes, a process that is critical for induction of long-term potentiation at dendritic synapses (Biel et al., 2009).

In addition to the role in membrane potential stabilization, dendritic integration, and synaptic plasticity regulation, I_h is also crucial in modulating oscillatory activity at both cellular and network levels (**Figure 1.5**). At the cellular level, the slow kinetics and subthreshold activation of I_h enable it to filter out input at low frequencies (< 3 HZ). In cells

with high I_h density at distal dendrites, dendritic I_h-dependent resonance is more pronounced and preferentially filters signals that propagate from the soma to the dendrites (Hu et al., 2009). These filtering properties of I_h may contribute to theta oscillation in the hippocampal circuits (Nolan et al., 2004), as well as theta and spindle oscillations in the thalamocortical circuits (Ludwig et al., 2003) and other network oscillations (Hu et al., 2002). In the perforant path-CA1 circuit, enhanced theta oscillations due to HCN1 deletion has been proposed as the physiological basis for hippocampal-dependent learning and memory storage (Nolan et al., 2004). HCN currents also generate a theta-like rhythm in layer II grid cells of the entorhinal cortex in functional interplay with subthreshold, persistent Na^+ currents (Alonso and Llinás, 1989). This periodic, hexagonally-patterned firing, scaling up progressively along the dorsal-ventral axis of the medial entorhinal cortex, is critically involved in spatial navigation (Moser et al., 2015). In thalamocortical neurons, a characteristic ‘burst mode’ appears during non-REM sleep or absence seizures, due to the interplay of I_h and a low-threshold Ca^{2+} current (T-current).

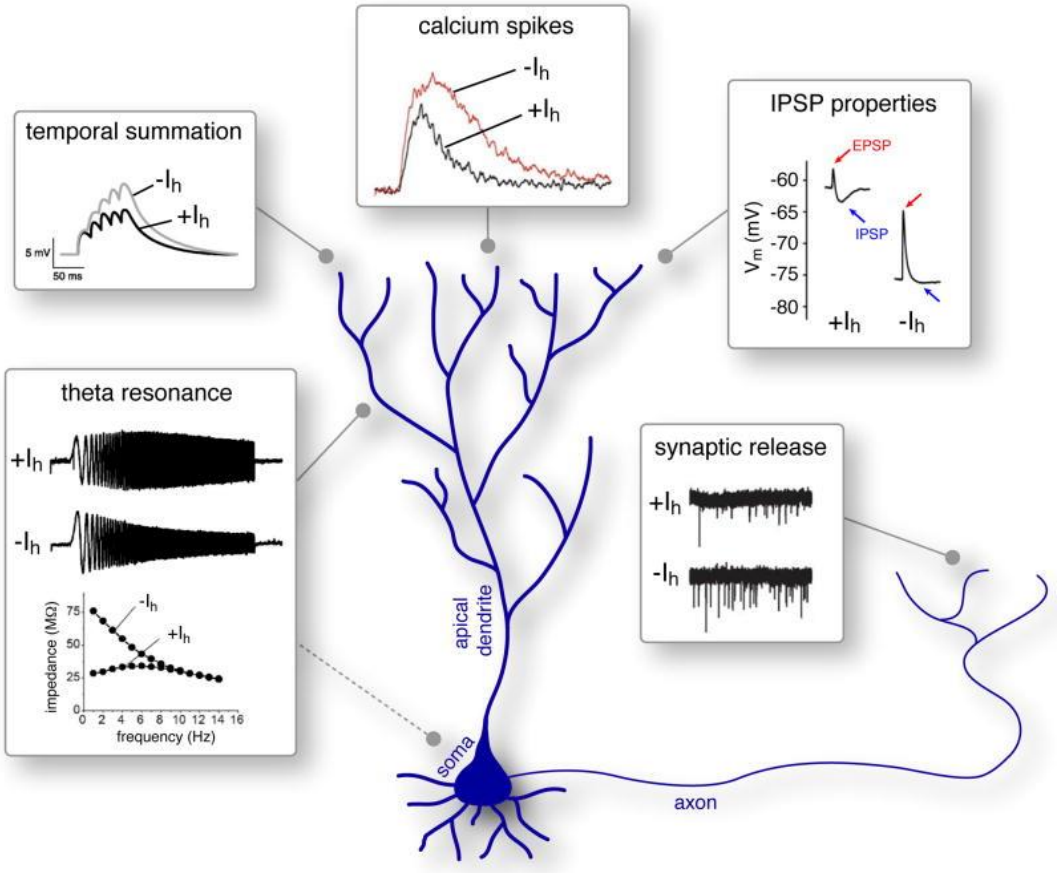

Figure 1.5 The multiple roles of I_h on neuronal activity.

A schematized neuron depicts the principal effects of I_h on neuronal activity in distinct subcellular domains. In dendrites, I_h reduces temporal summation, represses dendritic calcium spikes, and affects the integration of inhibitory postsynaptic potentials. In axon terminals, I_h reduces synaptic release through interplay with calcium channels. In both soma and dendrites, I_h augments theta-frequency resonance. Image from (Noam et al., 2011).

1.1.3. Dysregulation of HCN channels in epilepsy

Given the complex roles of I_h in fine-tuning membrane potential, synaptic plasticity, and network oscillation, it is not surprising that dysregulation of I_h has been implicated in epilepsy. Nevertheless, the role of HCN dysfunction in epilepsy is dynamic and intricate. Accumulating evidence showed that multiple mechanisms, including transcriptional control, subcellular distribution, and post-translational modification, act at different temporal and spatial scales to modulate I_h in epilepsy.

In experimental epilepsy models, acute and chronic loss of HCN1 channel expression, coupled with a reduction of I_h has presented as the most common finding in experimental epilepsy (Brewster et al., 2002; Jung et al., 2007; Marcelin et al., 2009; Powell et al., 2008; Shah et al., 2004). In the post status epilepticus (SE) model, dendritic loss of I_h can occur as rapidly as one-hour post-SE and last for a month till the chronically epileptic symptoms of the animals (Dubé et al., 2006; Jung et al., 2007; Williams et al., 2009). During this process, the pilocarpine model tends to produce more rapid development of epilepsy than kainite or experimental SE, which may be due to the severity of the resulting epilepsy phenotype.

Several mechanisms underlying loss of HCN channel expression following an epileptic insult have been elucidated. In pyramidal neuronal dendrites, loss of surface expression of HCN1 subunits was observed within the first hour following SE, whereas the total protein expression of HCN1 channel was unchanged, suggesting internalization of HCN1 channels following SE (Jung et al., 2011). The reduction of the HCN1 mRNA level was also detected in several models. Besides, the hyperpolarizing shift in the gating, which reduces the fraction of channels open at neuronal resting potential, also contributes to the loss of I_h in epilepsy (Chen et al., 2001; Jung et al., 2007). This down-regulation of HCN channel gating is strongly correlated with the decreased phosphorylation mediated by the p38 mitogen-activated protein kinase or the protein phosphatase 2B. Pharmacological regulation of these phosphorylation signaling pathways led to the normalization of HCN channel gating (Jung et al., 2010), suggesting an additional role of post-translational mechanisms underlying HCN channelopathy in epilepsy.

In knockout and genetic model studies, the deletion of HCN2 in mice led to generalized, spike-wave electroencephalographic discharges, typical clinical hallmarks of absence epilepsy (Ludwig et al., 2003). The deletion of the HCN1 gene in mice did not produce an epileptic phenotype. However, it resulted in increased cortical excitability and seizure susceptibility, which suggests a lack of HCN1 channel gives rise to increased dendritic input resistance in cortical neurons and thus greater synaptic integration and firing (Huang et al., 2009; Santoro et al., 2010). Nevertheless, the compensatory expression of other HCN subtypes as a response to abnormal excitability should be considered.

Human mutation studies have advanced our understanding of the potential role of HCN channel mutations in human genetic epilepsy. In patients with febrile seizures related syndromes, a triple proline deletion of the HCN2 gene was identified and was associated with augmented I_h when recombinant channels were exogenously expressed (Dibbens et al., 2010). In another study that conducted genetic screening of the families with epilepsy for mutations in HCN1 and HCN2, a recessive loss-of-function point mutation (E515K) in HCN2 was identified in a patient with sporadic idiopathic generalized epilepsy (DiFrancesco et al., 2011). The mutation was found to be located in the C-linker, a region of the channel known to affect channel gating. Subsequent functional analysis revealed that this homomeric mutant strongly inhibited function by hyperpolarizing shift of voltage-dependent activation with slowed activation kinetics. However, there is also evidence showing enhanced levels of HCN1 expression and dendritic localization in granule cells of the dentate gyrus in the resected hippocampal tissue from patients with temporal lobe epilepsy (Bender et al., 2003). Given the importance of I_h in attenuating dendritic postsynaptic potential, increased levels of HCN1 expression may represent a protective mechanism to reduce neuronal hyperexcitability (Dibbens et al., 2010).

Considering the multi-faceted roles of the HCN channels, the effects resulting from dysregulation of HCN channels in epilepsy are complex. Biophysical studies that elucidate the structural basis underlying altered function can aid in the understanding of the structure-function relationship of HCN channels, and thus the development of novel therapeutic compounds targeting HCN channels.

1.1.4. HCN channel as pharmacological targets for epilepsy

The complexity of the mechanism underlying HCN regulation in epilepsy makes it very challenging to develop a general rationale for drug design. Indeed, both pharmacological blockers and activator of HCN channels were reported to be useful in the context of epilepsy. As an example, I_h blocker ZD7288 was effective in reducing hippocampal epileptiform discharges in rabbits (Kitayama et al., 2003). Conversely, two well-established antiepileptic drugs — lamotrigine and gabapentin — upregulated HCN current (Poolos et al., 2002; Surges et al., 2003). Further structural studies are required to elucidate drug-channel interactions in complicated clinical settings.

For structural-based drug design (SBDD), one priority to consider is the drug binding site within HCN channels. Blockers that target the intracellular side of the HCN channel, such as Ivabradine, generally require drug penetration through the membrane. Some drugs are trapped in the ion-conducting pore, leading to very slow off-kinetics; in the case of ZD7288, an almost irreversible block was produced. For an optimal drug-channel interaction, drugs should access HCN channels from the extracellular side in a reversible manner. Besides, it is of essential importance to develop HCN subtype-specific drugs to minimize side effects. As an illustration, compounds that selectively inhibit HCN1 channels should have minimum side effects on cardiac rhythmic activity. Last, with growing evidence suggesting a critical role of HCN1-HCN2 heteromer formation in the pathogenesis of epilepsy (Brewster et al., 2005), it is tempting to assume that drugs targeting the heteromeric over homomeric channels would be potential therapeutic alternatives for epilepsy.

The high-resolution structure of the HCN1 channel solved by single-particle cryo-EM (Lee and Mackinnon, 2017), has provided unprecedented insight into the structure details of HCN1 channels. Nevertheless, the structural determinator that governs the altered pharmaceutic response is still unknown. Further studies to map the structure-function relationship of HCN1 channels remain a challenge.

1.2. Structure determination of membrane proteins

1.2.1. Membrane proteins and their membrane environments

Membrane proteins are central to a variety of critical cellular and physiological functions, including signal transduction, energy conversion, and transport of ions and metabolites, constituting up to 40% of eukaryotic and prokaryotic proteomes (Uhlen et al., 2015; Wallin and Heijne, 2008). Dysfunction of membrane proteins is implicated in diseases as diverse as neurological disorders and cancer; therefore, membrane proteins have long been important drug targets, of which G protein-coupled receptors and ion channels comprise the most abundant groups (Moraes et al., 2014).

Unlike soluble proteins, membrane proteins are inserted into lipid hydrophobic bilayer. As a result of the amphipathic nature of the membrane, two orders of magnitude

variation in dielectric constant occur across the membrane (Nymeyer and Zhou, 2008; Stern and Feller, 2003), which has a profound effect on the magnitude of electrostatic interactions across the lipid bilayers. Additionally, there is also a dramatic change in water concentration across the membrane (Mathai et al., 2001; Simon et al., 1982). Furthermore, the amphipathic nature of lipid molecules also contributes to the stabilization of the bilayer structure, demonstrating as the lipid pressure profile with the positive lateral pressure in the hydrophobic core and negative lateral pressure in the lipid interfacial region. The biophysical properties and lipid components of membrane exert fundamental effects on the structure and function of membrane proteins. Recent studies have suggested that lipid-binding sites within membrane proteins can influence protein folding and structural integrity (Lingwood and Simons, 2010). Besides, water molecules within the membrane are essential components of many protein-ligand complexes that mediate hydrogen bonding and impact the free energy of protein-ligand complexes. The lipid pressure profile has been found to spectacularly influence mechanosensitive channel gating (Gullingsrud and Schulten, 2004).

The past 60 years have witnessed exciting advances of structural biology in providing atomic-resolution structural details, yet only a few atomic structures of membrane proteins have thus far been solved compared with the number solved for soluble ones. As of early 2020, the protein data bank (PDB) deposits over 160,000 protein structures, while less than 4% are classified as membrane proteins (http://blanco.biomol.uci.edu/mpstruc/). The primary technical challenge facing membrane protein structure determination is to extract membrane protein from its native cellular environment and purify and solubilize it in detergents without loss of function.

1.2.2. Expression and purification: a bottleneck step

Membrane proteins are naturally expressed at low levels; therefore, overexpression is often a necessary step to ensure high concentrations of protein for structural analysis. Advances in this field are the primary keys to structural determination in many cases. So far, both prokaryotic (e.g., bacterial) and eukaryotic (e.g., yeast, baculovirus-infected insect cells, mammalian cells) expression systems, or even cell-free expression systems (Kuruma and Ueda, 2015), are used to achieve protein overexpression, each with its characteristics and limitation. The bacterial expression is

widely used as a quick screening method for its fast and inexpensive production of proteins. However, it frequently leads to misfolding and aggregation of eukaryotic proteins, likely due to differences in folding environment and lack of post-translational modification machinery; therefore, eukaryotic recombinant expression systems play an increasingly more critical role (Assenberg et al., 2013).

The extensive screening of the expression system can be quite labor-intensive and time-consuming. Conventional approaches mainly rely on altering external parameters to optimize protein production, such as using weak promoters and adjusting culture conditions. More targeted approaches, such as modification of protease or secretion pathway (Song et al., 2015), have been applied to achieve high yields of recombinant membrane protein expression. More recently, the cell-free expression system (Endo and Sawasaki, 2006; Sawasaki et al., 2002) has emerged as a state-of-the-art approach. As host cells are no longer required, this approach eliminates the toxic side-effect attributed to the over-expression of recombinant proteins. Besides, it allows manipulation of the reaction condition by adding lipids or detergent to protect or stabilize the produced recombinant protein. With the methodological progress in molecular cloning, automation, and bioinformatics, expression systems have become more high-throughput, enabling challenging structures of considerable amounts of membrane proteins to be solved.

Another challenge of membrane protein structure determination lies in the purification of membrane protein in a stable form. As the lipid composition and biophysical properties of the native membrane are crucial for retaining the structure and function of membrane protein (Simons and Sampaio, 2011), the use of detergent to extract membrane protein in its functional state is often challenging. When solubilized in detergents, many membrane proteins are vulnerable, and even slight structure perturbation may lead to protein denaturation and aggregation. This problem is particularly acute for membrane protein from higher eukaryotes; therefore, most membrane proteins whose structures have been solved, came from bacterias so far.

Furthermore, in x-ray crystallography, detergents generally make crystallization notoriously tricky, and protein engineering is often required to facilitate this process. However, this can cause the protein structure solved to be far from, or even unrelated to its full function state. Although cryo-EM enables membrane proteins to be imaged directly

solubilized in detergents or more natural environments such as nano-discs (Schuler et al., 2019), liposomes (Wang and Sigworth, 2010), and saposin-lipoprotein nanoparticle system (Frauenfeld et al., 2011) (**Figure 1.6**), the searching for optimal detergents, which can maintain the essential lipid required for preserving the functional and structural integrity of membrane protein within the lipid-protein-detergent complex, is a time-consuming process with trial and error (Hunte, 2005).

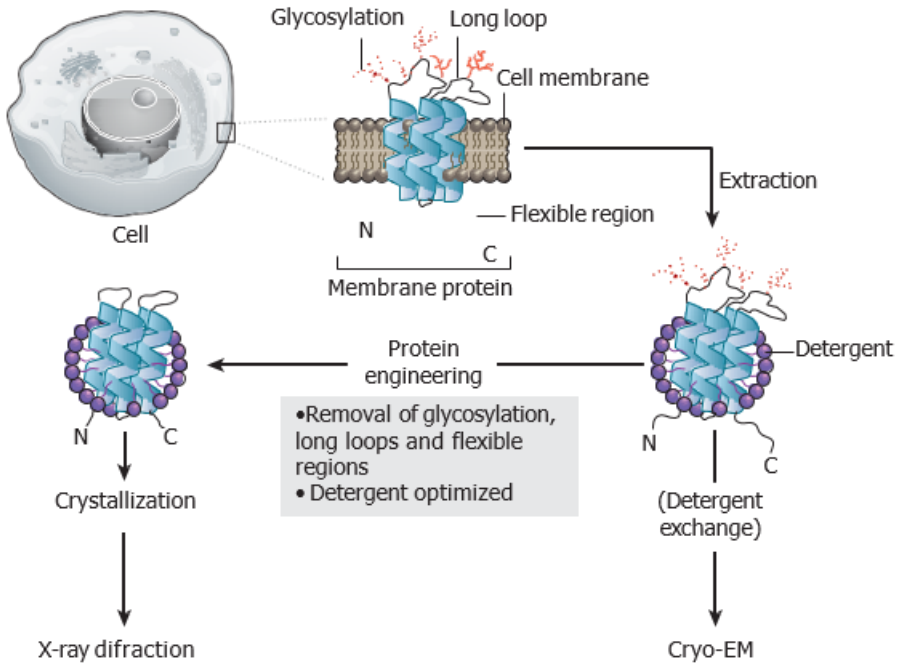

Figure 1.6 Extraction of membrane proteins.

Proteins must be extracted and solubilized from the membrane before structure determination. The crystallization of membrane proteins for X-ray crystallography often requires protein engineering to remove glycosylation, long loops, and flexible regions. Meanwhile, cryo-EM enables membrane proteins to be imaged directly in detergents or nano-discs. Image from (Fernandez-Leiro and Scheres, 2016).

1.2.3. Biophysical methods to study membrane proteins

1.2.3.1. **Membrane protein crystallography**

Since the structure determination of myoglobin in 1957 (Kendrew et al., 1958), X-ray crystallography has been the anchoring tool of structural biology and delivered a wealth of 3D atomic-level structural information of vital macromolecules. Before 2013,

most atomic-structures deposited in the PDB come from X-ray crystallography. Although it has become a routine method after a hundred years of maturation and development, structure determination by this technique remains challenging.

The main bottleneck comes from the growth of well-ordered 3D crystals of sufficient size, in order to obtain a high-resolution X-ray crystallography protein structure. Membrane proteins, especially those containing multiple domains and flexible regions, are recalcitrant to crystallization. Finding a crystallizable protein domain often requires many trials of protein engineering, each involving different truncation, mutations, side-chain modification, or proteolysis of the target protein (Li et al., 2013; Sobolevsky et al., 2009). Besides, the presence of detergents within the protein-lipid-detergent complex may undergo a phase separation with increasing concentration of precipitant, thus making the crystallization of membrane protein more challenging compared to soluble ones. For proteins with small extracellular domains, the presence of detergent can restrict crystal contacts, which often requires the adding of monoclonal antibodies to facilitate crystal formation. All these parameters make the condition screening for crystallization more time-consuming and expensive.

Over the past two decades, reagents and tools for crystallization have enormously improved (McPherson and Gavira, 2014). Crystallization robots reduce protein amounts substantially and permit thousands of crystallization conditions to be coarse-screened simultaneously. Besides, an automatic system has enabled condition screening and crystal search more high-throughput. Furthermore, the lipidic cubic phase (LCP) crystallization has emerged as a good alternative for membrane protein crystallization (Caffrey, 2009). In this method, proteins are initially embedded in a stabilizing medium, and crystallization is then driven by lateral diffusion after the addition of precipitants (Cherezov, 2009). In this lipidic bilayer, protein-protein interaction is mediated by monooleins in the LCP medium, whereas the interaction perpendicular to the plane is controlled more by the precipitant. As a result, a network with sufficient rigidity for exceptional diffraction pattern is formed. The ability to crystallize membrane protein in a membrane-like environment opens the possibility of exploring protein-lipid interactions, which is vital for the activities of membrane proteins.

Another challenge inherent to protein crystallography is the ‘phase problem.’ Conventional methods to address these problems include molecular replacements, multiple isomorphous replacements, and multiple anomalous dispersion. However, these methods are limited by the crystal fragility, a lack of access to the labeling sites, and non-specific interaction of hydrophobic heavy-atom compounds with the detergent. Advances in X-ray sources, diffraction methods, in conjunction with fast detectors, have revolutionized macromolecular crystallography for the data collection. The very high flux densities (photons per second per mm^2) of the synchrotron beamline allow the use of weakly diffracting microcrystals for structure determination (Smith et al., 2012). With the capability to deliver X-ray beamline matching in size to microcrystals, microdiffraction beamlines are ideal for use with LCP-growth crystals of membrane proteins. Another innovative improvement in phasing software (e.g., the SHELX) has made the experimental phasing with very weak anomalous signals feasible (Sheldrick, 2008). The SHELX suites are so fast and robust that they are often employed in pipelines for high-throughput phasing. When combining data collected from multiple crystals at relatively lower energy, the signal-to-noise ratio (SNR) in the slight anomalous scattering from native structures is vastly enhanced (Liu et al., 2012).

Concurrent with the developments in hardware and software, computational tools for structure solution have rapidly advanced over the past decade. Crystallographic software, such as CCP4 (Winn et al., 2011) and PHENIX (Afonine et al., 2012), has now enabled the automation of the process from data collection through electron density map calculation, model building, and structure refinement. Once diffraction and phasing information are available, a protein model can be built and refined to match the electron density maps optimally, using the robust automatic model-building software. For manual model building and validation of biological macromolecules, programs such as Coot (Emsley et al., 2010) are tremendously efficient in refinement and rebuilding. Lipids and detergents that bind to the compound can also be identified from residual electron densities, the locations of which offer unique information regarding lipid-protein interactions.

1.2.3.2. **Single-particle cryo-EM**

For membrane protein that is refractory to crystallization or challenging to crystallize in a specific functional state, single-particle cryo-EM has emerged as a transformative approach to solve protein structures at near-atomic resolution (Amunts et al., 2017). Rather than determining structures from the diffraction of 3D crystals, singe-particle cryo-EM works by computationally averaging images of many individual particles (Frank et al., 1978; Henderson, 2004). It is possible to image membrane protein directly solubilized in detergents or amphipols, or stabilized in a more natural environment such as nanodiscs (Cheng et al., 2015) or the saposin-lipoprotein system (Frauenfeld et al., 2016). In this approach, samples of purified molecules are plunge-frozen in a thin layer of vitreous ice that preserves the native structure (Taylor and Glaeser, 1974), reduces radiation damage (Stark et al., 1996) and prevents sample dehydration within the vacuum of the transmission electron microscope (TEM). Two-dimensional (2D) projections of individual particles are aligned, classified, and averaged to increase SNR and produce a 3D reconstruction. An atomic model can then be built by fitting the known sequences into the density map from the 3D reconstruction (**Figure 1.7**). The structural resolution depends on multiple factors, including microscope performance (illumination coherence, detector efficiency), sample homogeneity, orientation distribution of the particles, and computation robustness.

In theory, cryo-EM can determine the atomic structure of macromolecules as small as 100 kDa in the molecular weight (Henderson, 1995). However, to achieve such a resolution remains challenging, as the contrast between the particles and their support medium is becoming increasingly difficult. For any electron micrographs, both amplitudes and phases are modulated by the contrast transfer function (CTF), which is mostly a sine function with an envelope that reduces the amplitude at high resolution**.** The overall envelop function combines multiple factors, including the spatial and temporal coherence of the electron beam, specimen motion, and the modulation transfer function of the imaging recording device. For frozen-hydrated biological molecules, especially for small molecules, images are captured at a defocus to generate phase contrast in the image, yet at the cost of a reduction in the high-resolution information. This delicate balance between contrast and resolution is the primary resolution limitation of single-particle cryo-EM

reconstruction. In recent years, the application of phase plates and energy filters has considerably enhanced the image contrast for small protein complexes (Thompson et al., 2016).

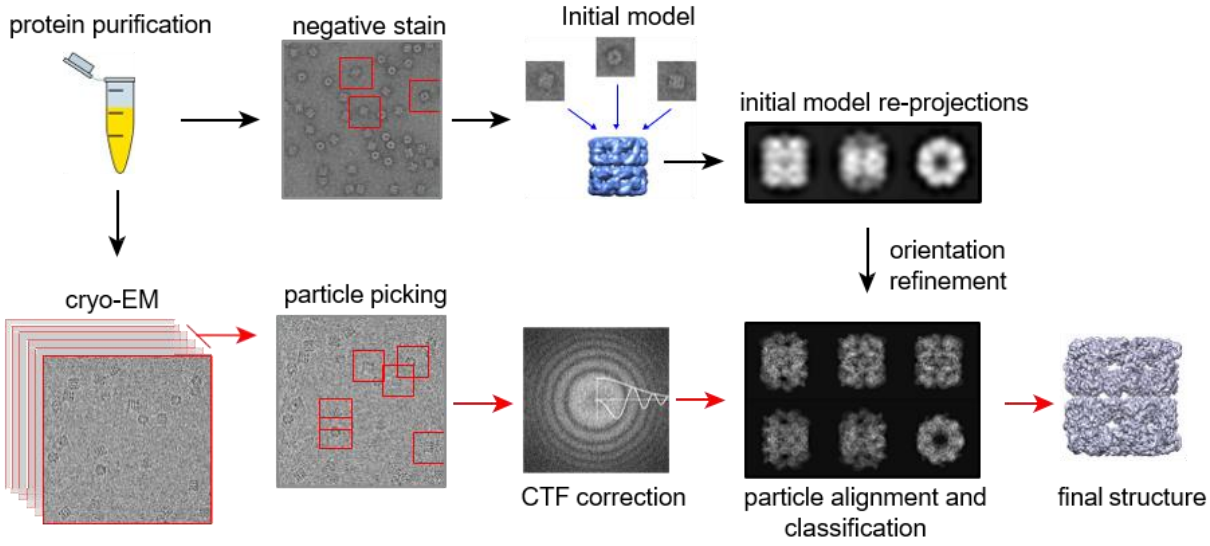

Figure 1.7 Schematic of single-particle reconstruction.

The negative stain is useful to check protein sample homogeneity. Particles picked from the micrographs are classified and averaged to obtain a low-resolution initial model by standard lines or tilt methods. In cryo-EM, the vitrified sample is imaged by collecting movie frames that are then motion-corrected, aligned, and averaged. After defocus determination and CTF correction on motion-corrected averaged images, particles are aligned and classified and assigned orientations by projections matching to the initial model. This orientation refinement is performed iteratively until the final structure converges. Image from (Carroni and Saibil, 2016).

Recent advances in instrumentation and computational image analysis have led to a breakthrough in achievable resolution, namely the ‘resolution revolution’ (Kühlbrandt, 2014). With the new generation of detectors, high-resolution images can be built from fewer particles. The development of software for image processing enables us to deal with conformational and compositional heterogeneity among the particles (Behrmann et al., 2015; Frank, 2013; Loerke et al., 2010; Zhao et al., 2015). Whereas dynamic protein complexes would need to be trapped in a single state to facilitate crystallography, the maximum likelihood-based classification algorithms (Scheres et al., 2007; Scheres, 2010), or the latest multi-body refinement methods (Nakane et al., 2018) of cryo-EM allow the presence of multiple functional states of proteins in one image. By determining the

structure of highly dynamic protein complexes, cryo-EM is providing unprecedented insight into the function of large macromolecular machines. Last, automation of data acquisition and processing has dramatically reduced the amount of time it takes from sample preparation to structure determination. The technology of single-particle cryo-EM is still moving-forward rapidly. With the potential of solving structure at a resolution beyond 3 Å, cryo-EM structure-based drug design will become routine for targets that are extremely difficult to characterize using alternative techniques. Also, in cases where single-particle cryo-EM fails to provide high-resolution maps, a hybrid method combining protein crystallography and cryo-EM can be applied to visualize macromolecules at the pseudo-atomic resolution as described in Natesh (Natesh, 2014).

1.2.3.3. **Structure dynamics by NMR**

Membrane proteins are naturally dynamic and may interconvert among several distinct conformational states to accomplish complicated biological functions. Elucidating the interaction between structure and dynamics can provide novel mechanistic insight into the complex functionality of membrane proteins. Nuclear magnetic resonance (NMR) spectroscopy applied to biological samples is emerging as an increasingly important tool for probing the structure and dynamics of membrane proteins. This method occupies a unique niche as it permits the determination of structure and dynamics of proteins and peptides in the range of 10~40 kDa, which is especially challenging to crystallize, or structurally determined by current EM-techniques.

NMR bypasses the need for crystallization, yet it still faces particular challenges that are not encountered by soluble proteins, including sample preparation, size limitation, and spectral crowding. There are two main technical approaches: solution NMR and solid-state NMR (ssNMR) (Zhou and Cross, 2013). While solution NMR methods can be applied to study proteins embedded in micelles, bicelles, and nanodiscs, with fast rotational diffusion (<100 ns), ssNMR methods are utilized to study static samples or samples with high-speed mechanical rotation. Therefore, ssNMR is more favored for the study of membrane protein as the samples are inserted in the close-to-native lipid bilayers. However, due to the spectral crowding of uniform labeling, most proteins studied by ssNMR are limited to the molecular masses less than 10 kDa.

Despite these limitations, NMR spectrometry has proved to be a unique method that can provide residue-specific dynamics information on macromolecules ranging from picoseconds to seconds at atomic resolution. Various biological processes, such as conformational change, ligand binding, and protein-protein interaction can be characterized at the residue level through techniques varying from chemical shift changes to docking protocols, without the need to solve the structure of the corresponding complex (Zamoon et al., 2005). NMR experiments based on selective labeling are also of noticeable interest in drug design and are expected to develop soon.

1.2.3.4. **Molecular dynamics simulations**

To fully understand membrane protein function, it is essential to accurately 'transplant' membrane protein structure into a lipid bilayer and monitor its dynamic behavior in the native environment. Molecular dynamics (MD) simulations provide the possibility of probing the dynamics and conformational changes of membrane proteins, adding to our understanding of channel gating and transport dynamics (**Figure 1.8**) (Bostick and Brooks, 2007; Noskov et al., 2004; Tajkhorshid et al., 2002). Besides, this approach can be used to characterize the protein-lipid interaction and the lipid-binding sites on the protein surface (Hansen et al., 2011).

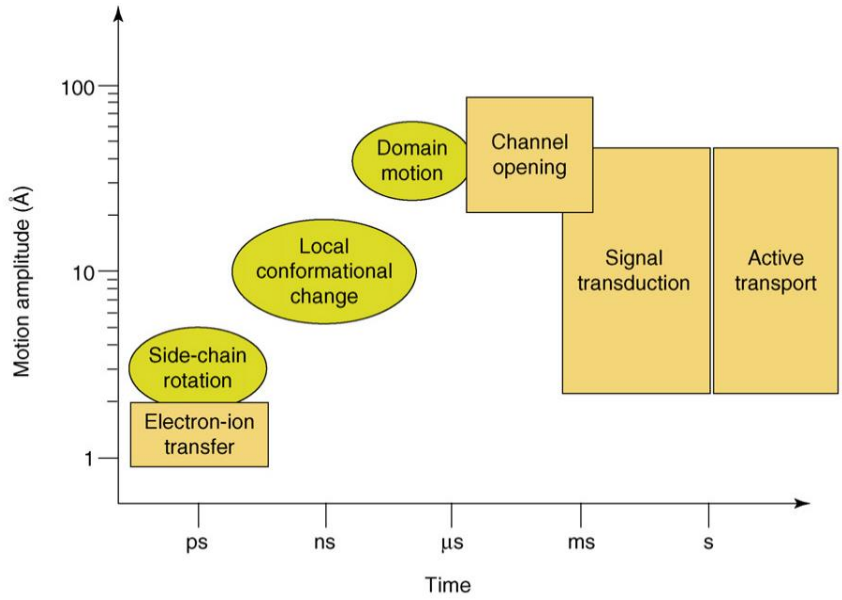

Figure 1.8 Time scale and amplitude motion in membrane proteins.
Image adapted from (Lacapère et al., 2007)

Because of advancements in hardware and software, longer timescale (1 μs and beyond) and larger systems are explored by MD simulations at the atomic level, which has enabled the observation of side-chain rotation and ligand-binding induced local conformational changes, yet exploration of large-scale conformational changes remains challenging. Methods to enhance the exploration of the energy landscape, such as metadynamics (Leone et al., 2010) or dynamics importance sampling (Perilla et al., 2011), have been applied to overcome these limitations. Computational methods, such as coarse-grained molecular dynamics simulations (Perlmutter et al., 2011; Negami et al., 2014), have been used to describe the protein-lipid interaction in a wide range of membrane proteins.

1.3. Electron tomography: toward structural biology in situ

The advancements of electron microscopy for structural biology go well beyond single-particle cryo-EM. Electron tomography (ET), a 3D imaging technique, so far is the only technique to study membrane protein 'in situ.' It captures the transient and dynamic state of proteins and protein complexes in the context of a native cellular network. In combination with advanced computational methods, cryo-ET is currently representing the most promising technique to map macromolecular architecture inside the native cellular environment.

Similar to single-particle cryo-EM, samples are quickly frozen to ensure optimal structural preservation and to minimize radiation damage (Bai et al., 2015). Besides, techniques of cryo-sectioning (Al-Amoudi et al., 2004) or focused ion beam (FIB) milling (Rigort et al., 2010) are applied to render access to thick mammalian cells (> 500 nm) (Adrian et al., 1984). For the acquisition of tomographic tilt series, the sample is rotated relative to the electron beam, and a set of 2D projection images are collected (**Figure 1.9**). Due to specimen thickness and stage mechanics, the angular range is often limited to ± 70 º, which is known as the 'missing wedge' problem. This 'missing wedge' in the Fourier space leads to inhomogeneous data distribution and poor resolution along the beam axis, which makes the sub-tomogram averaging more challenging, further reducing the achievable resolution (Schmid and Booth, 2008). Acquisition of a double-tilt series (Winkler and Taylor, 2013), whereby two tilt-series with a relative 90º in-plane rotation are performed, can correct this shortcoming. Besides, computational approaches are making

new headway to counteract this ‘missing wedge’ artifact (Kupsch et al., 2016; Yan et al., 2019).

Another crucial problem inherent in ET is the radiation damage. Electron dose applicable to the sample is limited below 100 $e^-/Å^2$ to preserve the macromolecular structure (Conway et al., 1993; Glaeser, 1971). For tilt series, this dose is further fractionated over multiple images, resulting in poor SNR ratios compared to a typical 2D image. This poor SNR can be mitigated through approaches, including (i) a ‘dose-symmetric tilt-scheme,’ which begins at low angles and then alternates between increasingly positive and negative tilts (Hagen et al., 2017); (ii) coating the specimen with a thin layer of carbon (Egerton et al., 2010); and (iii) using a nearby area for image alignment, thus reducing the unnecessary radiation exposure during imaging (Scott et al., 2012).

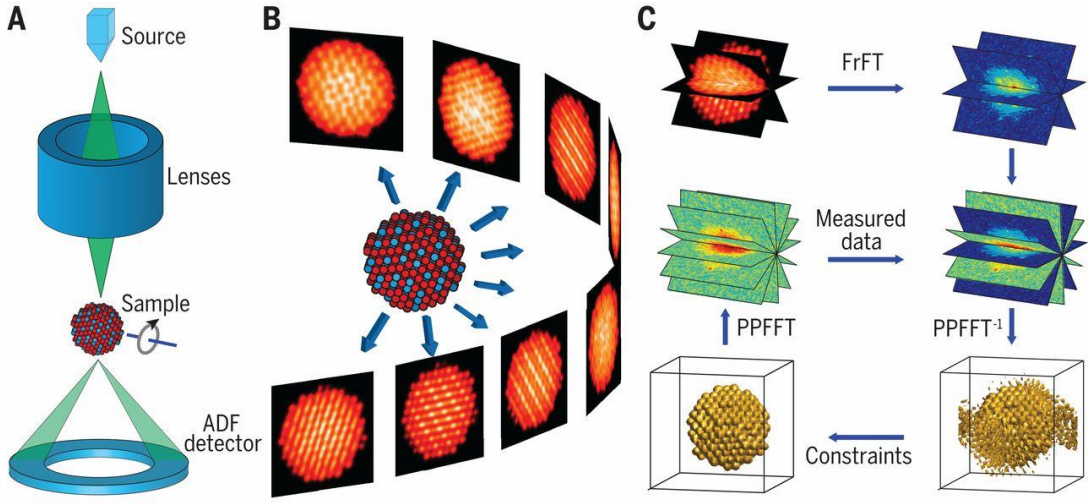

Figure 1.9 Schematic layout of electron tomography.

(A) An electron beam is focused on the sample to form a 2D projection. (B) A series of 2D projections are collected at different tilt angles. (C) After alignment, a series of 2D projections are inverted to Fourier slices by the fractional Fourier transform (FrFT), from which a 3D reconstruction is computed. Image from (Miao et al., 2016).

After the acquisition of the tilt series, sample drift and scanning distortion are corrected to minimize the alignment error (Xu et al., 2015). Before reliable biological information can be extracted, advanced denoising algorithms are often implemented to increase the SNR and visualize component details at the molecular resolution level (Dabov et al., 2007; Huang et al., 2018; Narasimha et al., 2008). The precise alignment

of tilt-series can be performed either by the use of high-contrast fiducial markers in the samples to determine the relative orientation of the 2D projections, or by using the marker-free ‘patch tracking,’ which relies on the calculation of cross-correlation between images patches across the tilt-series (Castaño-Díez et al., 2010; Fernandez et al., 2018). Generating a high-quality tomogram from a tilt series was initially an interactive, labor-intensive process. Several automated image alignment schemes have been developed for efficient data collection (Castaño-Díez et al., 2010; Han et al., 2015; Sorzano et al., 2009).

After alignment, tomographic 3D reconstruction is achieved by either Fourier-space algorithms, such as weighted backprojection (Radermacher, 1988), or real space algorithms, such as the Simultaneous Iterative Reconstruction Technique (SIRT) (Gregor and Benson, 2008). Backprojection is the conceptually most straightforward approach based on the central slice theorem. In this approach, the Fourier transform of each projection corresponds to a planar slice through the Fourier transform of the 3D volume, which is then back-projected by reverse Fourier transform to yield a real-space 3D reconstruction (De Rosier and Klug, 1968). Meanwhile, real-space reconstruction methods, such as SIRT, are more suited to tackle the incomplete data issue caused by the ‘missing wedge’ artifact and is generally slower than weighted backprojection. SIRT and various related iterative techniques, such as the algebraic reconstruction technique (Gordon et al., 1970), and the simultaneous algebraic reconstruction technique (Andersen and Kak, 1984), compute a 3D reconstruction by iteratively calculating a system of linear equations, in which constraints can be incorporated easily to reduce artifacts.

Similar to single-particle reconstruction, subtomogram averaging, which works by iteratively aligning a large number of images of the particles, is applied to increase the SNR and achievable resolution. One crucial distinction from single-particle reconstruction is that it deals with 3D volumes rather than 2D projections (Wan and Briggs, 2016). With specialized tilt schemes and methods, even near-atomic resolution can be achieved using subtomogram averaging (Schur et al., 2016). High-resolution structures obtained from other structure methods can also be implemented to fit tomograms into detailed models of macromolecules in the cellular context.

Tomographic 3D reconstruction represents a snapshot of the cell. It can capture the transient and dynamic events that could be missed out when using purification methods, yet the interpretation of 3D volume at the ultrastructure level, as well as annotating molecular components of interest from the crowded intracellular environment, requires the decomposition of a tomogram into structural components. Individual molecular machines within the cellular context can be identified by their structure signatures determined by other biophysical approaches. By utilizing template-matching methods, an extensive volume cross-correlation search is performed between the molecular volume and the cellular tomogram to find the location and orientation of the proteins inside the cell. Although molecular crowding and low tomogram resolution pose a limitation on the applicability of this technique (Beck et al., 2009), considerable advancement in computational approaches (Chen et al., 2017) has made it possible for revealing the spatial relationship of molecules in their functional states (Mahamid et al., 2016).

1.4. Correlative light and electron microscopy

Within the field of biology, fluorescence microscopy (FM) allows the study of fluorescently tagged molecules in live or fixed biological samples; however, the resolution is limited to submicrometer, which is incapable of resolving biomolecules ranging from 0.1 to 10 nm. On the other hand, high-resolution structural details can be achieved with electron microscopy (EM), but specific labeling of molecules by EM is challenging, making the detection of rare events in time and space scale nearly impossible. Correlative light and electron microscopy (CLEM), a powerful tool to combine the strength of EM with fluorescent light microscopy (fLM), can bridge the resolution gap between both imaging modalities and help to identify areas of interest within the crowded cellular landscape on high-magnification scales (**Figure 1.10**).

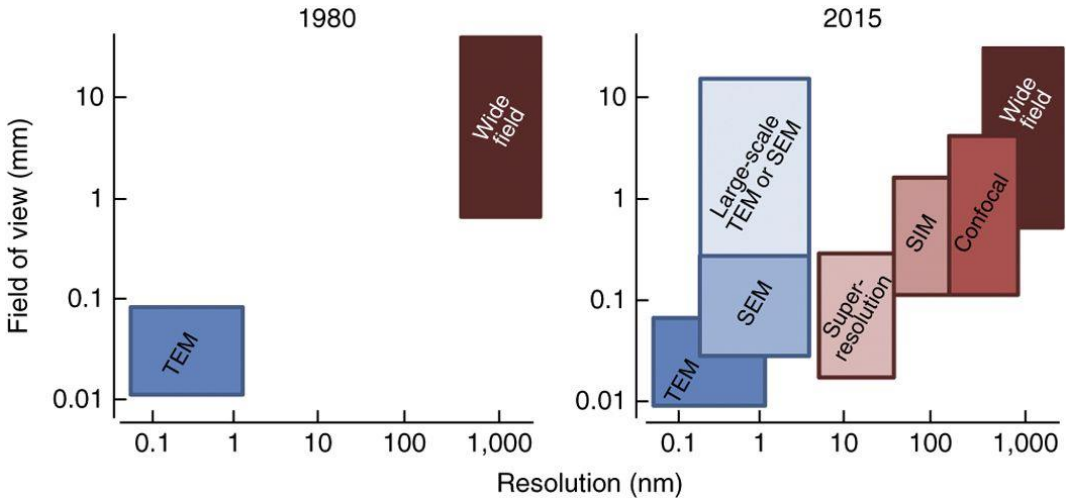

Figure 1.10 Matching scales of FM and EM.

The resolution gap between FM (red) and EM (blue) has been filled by the increased field view of EM, and the emergence of super-resolution fluorescence microscopy. Note that all FM and EM imaging techniques depicted here can be applied in the CLEM. Image from (De Boer et al., 2015).

Correlation can be performed either in a two-step LM-EM approach (**Figure 1.11**) (Celler et al., 2016; Hampton et al., 2017), or on an integrated set-up (Faas et al., 2013; Wang et al., 2017). The appropriate approach taken depends on the scientific question to be addressed. If a transient or dynamic intracellular trafficking event is being studied, then a live-cell imaging approach at the LM stage is necessary to capture the dynamic events before the sample is immobilized and processed for EM. On the other hand, an integrated light and electron microscopy enables the imaging of LM and EM samples at cryogenic temperatures in a single microscope, which removes the needs for sample transfer and thus complicated correlation procedures.

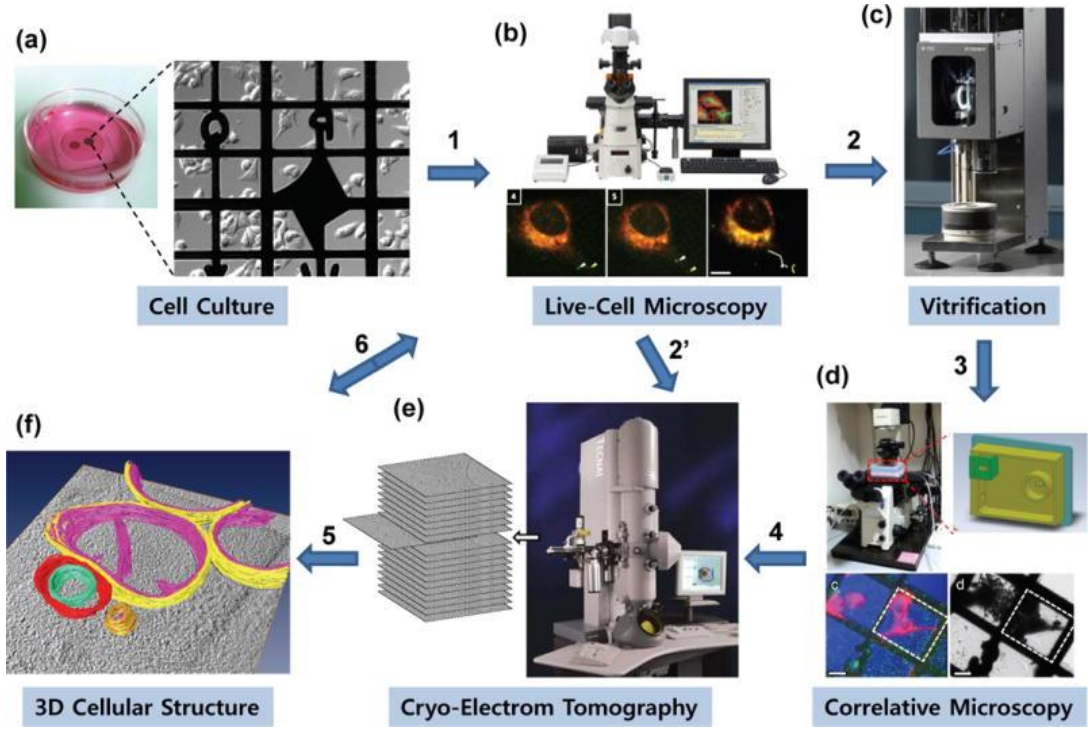

Figure 1.11 A general flowchart for cryo-CLEM procedures.

These steps include: (a) culturing cells on carbon-coated EM grids; (b) live-cell imaging; (c) vitrification of the sample at near-native state; (d) localizing the target of interest using CLEM techniques for subsequent cryo-ET; (e) cryo-ET data acquisition and 3D reconstruction; (f) 3D structural analysis, correlating high-resolution cellular structure with the fluorescently labeled proteins. Image from (Zhang, 2013)**.**

Classical EM sample preparation, which involves fixation, heavy metal staining, plastic embedding, and sectioning, can lead to fluorescence reduction. On the other hand, protocols that help preserve fluorescence in the EM sample may come at the expense of ultrastructure preservation. Thus, particular precaution during sample preparation is required to preserve both fluorescence and ultrastructures. Cryo-CLEM, in which samples are rapidly vitrified, thereby avoiding chemical fixation and embedding, provides an alternative for maximal preservation of both fluorescence and ultrastructure.

Targeted proteins are generally labeled with CLEM probes, which are fluorescent and electron-dense at both fLM and EM stages, to allow for easy detection. For high-resolution CLEM, the development of probes specifically for high precision correlation is fundamentally important. Different fiducial markers, including nanoparticles (Kopek et al., 2012; Sochacki et al., 2014), polymer beads (Kukulski et al., 2012), and quantum dots

(QDs) (Masich et al., 2006), have been used for this purpose. Although localization can be performed with a precision of ~40 nm using fLM (Schorb and Briggs, 2014), targeting specific molecules inside crowded cellular landscape requires fluorescence microscopy with higher resolution (Wolff et al., 2016). Several super-resolution fluorescence microscopy techniques have been developed, including techniques that sharpen the excitation point-spread function with saturated depletion, such as stimulated emission depletion microscopy (Hell and Wichmann, 1994; Klar and Hell, 1999), and techniques based on single-molecular localization, such as stochastic optical reconstruction microscopy (Rust et al., 2006) and photoactivation localization microscopy (Betzig et al., 2006). When applied in CLEM, these super-resolution fluorescence microscopy techniques can provide more correlated structural information that is not attainable by conventional fLM techniques. Future development in this area will allow functional imaging of cellular landscape at nanoscale resolution.

1.5. Structure-based drug design

Conventional methods, such as high-throughput screening methods (MacArron et al., 2011; Wildey et al., 2017), computational methods (Jorgensen, 2004; Sliwoski et al., 2014), and functional assays (Zhang and Xie, 2012; Kepp et al., 2019), have been applied in drug discovery. Nevertheless, only high resolution 3D structural studies can detail drug binding sites, conformational dynamics, and protein-drug interaction, thus enabling improved selectivity and pharmacological properties (Blundell et al., 2002; Deschamps, 2005; Murray and Blundell, 2010).

The field of SBDD is a rapidly growing area that leads to the successful discovery of many new drug leads. It involves the design and optimization of a drug candidate for clinical testing based on the 3D structure of the drug and the interaction with its biological target, enabling the visualization of the ligand-binding process and the prediction of key binding pocket sites as well as the affinity of ligands to their target macromolecular. Such information is critical for designing high-affinity ligands with desired pharmacological and therapeutic effects (Ferreira et al., 2015; Macalino et al., 2015).

SBDD consists of several critical procedures, including protein structure preparation, binding site identification, ligand library preparation, and molecular docking.

Over the past two decades, technical advances in the main biophysical approaches — X-ray crystallography, cryo-EM and NMR — have accelerated the process of structure determination of macromolecules and contributed tremendously to the development of highly potent and selective drugs; nevertheless, the drug development process is still time-consuming and expensive. To expedite drug development more cost-effectively, computer-aided drug discovery techniques, which can screen thousands of compounds instantly and select efficient candidates against the desired target proteins, are applied in various stages of drug development (Krivák and Hoksza, 2015).

However, challenges remain in this field. First of all, protein structures are naturally dynamic, and as ligand binds to the bioactive pockets, proteins can undergo substantial conformational changes; therefore, target flexibility in molecular docking should be accounted for throughout the modeling phase. Techniques such as flexible docking (Bolia et al., 2014; Elokely and Doerksen, 2013) are applied to handle these flexibility issues. Moreover, it is important to include water molecular in ligand-protein docking simulation to ensure the accuracy of molecular docking. Last, conformational intermediates are especially crucial in MD simulations as they may function as potential drug targets.

1.6. Aim of this study

Given the multi-faceted roles of HCN channels in tuning neuronal excitability, synaptic strength, and network oscillation, it is not surprising that its abnormal expression and function have been shown to play a crucial role in epilepsy. Growing evidence on altered expression level, subcellular distribution, and post-translational modification has added to our understanding of the HCN channel in the development of epilepsy, yet the structural basis underpinning its altered function is still poorly understood. The goal of this study is to unravel the structure-function relationship of HCN1 channels in the native cellular environment. To achieve this, we have generated membrane preparation potentially suitable for EM studies. Currently, nearly all the structure methods have relied on membrane mimetics, the deficiencies of which may cause structural perturbations (Zhou and Cross, 2013); therefore, this study can serve as a starting point for the establishment of a generalized method for studying membrane protein in its native membrane environment. It is hoped that the forthcoming high-resolution structural information can aid in structure-based drug design for the treatment of epilepsy.

2. Materials and Methods

2.1. Materials

2.1.1. Materials and reagents for cell culture

Product	Company
0.05% Trypsin-EDTA	Life Technologies, Waltham, USA
Blasticidin S HCl (10 mg ml^{-1})	Thermo Fisher Scientific, USA
Cell culture plate, 6-well, 12-well, 24-well, 96-well	VWR, Radnor, USA
Cell culture flask, T-25, T-75	Greiner Bio-One, Frickenhausen, Germany
Cell culture dishes, Ø 60 mm, Ø 90 mm	VWR, Radnor, USA
Cryovials	Thermo Fisher Scientific, USA
DMEM High Glucose Pyruvate	Thermo Fisher Scientific, USA
DMEM, High Glucose, GlutaMAX™ supplement	Thermo Fisher Scientific, USA
DPBS w/o Ca^{2+} and Mg^{2+} (PBS)	Life Technologies, Waltham, USA
DMSO	Sigma-Aldrich, USA
Falcon, 15 ml, 50 ml	Greiner Bio-One, Frickenhausen, Germany
Fetal bovine/calf serum	Life Technologies, Waltham, USA
Glass coverslips Ø 12mm	VWR, Radnor, USA
Geneticin (50 mg ml^{-1})	Thermo Fisher Scientific, USA
HEK-293 cell (CRL-1573)	ATCC, Virginia, USA
Lipofectamine 3000 regents	Thermo Fisher Scientific, USA
MEM no ess. Amino acids	Thermo Fisher Scientific, USA
Opti-MEM® I Reduced Serum Medium	Life Technologies, Waltham, USA
Penicillin-Streptomycin	Life Technologies, Waltham, USA
Pipette tips, 10 µl, 200 µl, 1000 µl	Greiner Bio-One, Frickenhausen, Germany
Poly-D-lysine	Sigma-Aldrich, USA
Puromycin Dihydrochloride	Thermo Fisher Scientific, USA

Sodium pyruvate	Thermo Fisher Scientific, USA
Syringe filter 0.2 µm cellulose acetate	VWR, Radnor, USA
Trypan blue solution	Thermo Fisher Scientific, USA

2.1.2. Material and reagents for cell labeling and imaging

Product	Company
Aqua-Poly/Mount mounting medium	VWR, Radnor, USA
CellMask Green plasma membrane stain	Thermo Fisher Scientific, USA
CellMask Orange plasma membrane stain	Thermo Fisher Scientific, USA
CellMask Deep Red plasma membrane stain	Thermo Fisher Scientific, USA
CellMask Green plasma membrane stain	Thermo Fisher Scientific, USA
DRAQ5 labeling solution	Thermo Fisher Scientific, USA
Hoechst 34580 labeling solution	Thermo Fisher Scientific, USA
Live Cell Imaging Solution	Thermo Fisher Scientific, USA
MitoTracker Orange CMTMRos	Thermo Fisher Scientific, USA
Microscope slide coverslip	Thermo Fisher Scientific, USA
QD705 ITK™ Amino (PEG) Quantum dots	Thermo Fisher Scientific, USA
TMA-DPH staining solution	Thermo Fisher Scientific, USA
Vybrant™ DiO cell-labeling solution	Thermo Fisher Scientific, USA

2.1.3. Materials and reagents for molecular biology

2.1.3.1. Materials and reagents for cloning

Product	Company
10× ligation buffer	Thermo Fisher Scientific, USA
10× pfu buffer with MgSO4	Thermo Fisher Scientific, USA
10× restriction buffer	Thermo Fisher Scientific, USA
6× loading buffer	Thermo Fisher Scientific, USA

Agarose	Biozym, Hessisch Oldendorf, Germany
Alkaline Phosphatase	New England Biolabs, Ipswich, USA
DNA Clean and Concentrator kit	Zymo Research, Irvine, USA
EndoFree Plasmid Maxi kit	Qiagen, Venlo, Netherlands
Gel DNA recovery kit	Zymo Research, Irvine, USA
GeneRuler 1 kb	Thermo Fisher Scientific, USA
GenJET Plasmid Miniprep kit	Thermo Fisher Scientific, USA
In-fusion Cloning kit	Takara, Kyoto, Japan
MilliQ water	Corning, USA
Nanodrop	Thermo Fisher Scientific, USA
NucleoSpin Gel and PCR Clean-up kit	Macherey-Nagel, Düren, Germany
PeqGreen DAN/RNA Dye	VWR, Radnor, USA
Phusion High-Fidelity DNA Polymerase	Thermo Fisher Scientific, USA
Restriction enzyme: BglII, EcoRI	Thermo Fisher Scientific, USA
Restriction enzyme: BbvCI, BamHI, PstI, FesI	VectroBuilder, USA
T4 DNA ligase	Thermo Fisher Scientific, USA

2.1.3.2. **Cloning primers**

Primer	**Sequence (5´- 3´)**	
$sfGFP_N$	FW	TCCCGGCCCTaGATCTATGTCCAAGGGAGA AGAGTTGTTTACT
	REV	CTGAGGCACGTCCCTTTCTCATTAGGGTCCT
SspInt_N	FW1	AGGGACGTGCCTCAGTTTTGGCACCG
	REV1	GGCACAGTCGGAATTCTTATTTAATTGTCCC AGCGT
$EGFP_N$	FW	TCCCGGCCCTaGATCTATGGTGAGCAAGGG CGAG
	REV	CTGAGGCAgtattctgcgaaCTTCTGCTTGTCG
SspInt_N	FW2	agaatacTGCCTCAGTTTTGGCACCGAA
	REV2	GGCACAGTCGGAATTCTTATTTAATTGTCCC AGCGT
SspInt_C::$sfGFP_C$	FW	TCCCGGCCCTaGATCTATGGTTAAAGTTATC

		GGTCGTCGT
	REV	GGCACAGTCGGAATTCttatgtgatgccagcagcgt
*Ssp*Intc::EGFP$_C$	FW	TCATTTTGGCAAGCTTATGGTTAAAGTTATC GGTCGTCGT
	REV	GACACCATAGGGCCGGGATTCTCCT
*Ssp*Intc::sfGFP$_C$::T2A	FW	TCATTTTGGCAAGCTTATGGTTAAAGTTATC GGTCGTCGT
	REV	GACACCATAGGGCCGGGATTCTCCT
mTagBFP2	FW1	CGGCCCTATGGTGTCTAAGGGCGAAGAGCT
	REV1	GGCACAGTCGGAATTCttaATTAAGCTTGTGC CCCAGTTTG
*Ssp*Int$_C$::EGFP$_C$::T2A	FW	TCATTTTGGCAAGCTTATGGTTAAAGTTATC GGTCGTCGT
	REV	GACACCATAGGGCCGGGATTCTCCT
mTagBFP2	FW2	CGGCCCTATGGTGTCTAAGGGCGAAGAGC
	REV2	GGCACAGTCGGAATTCttaATTAAGCTTGTG CCCCAGTTTGCT
*Npu*Int$_N$	FW	TCCCGGCCCTaGATCTATGTCCAAGGGAGA AGAGTTGTTTACT
	REV	GGCACAGTCGGAATTCttaGTTAGGCAGGTT GT
*Npu*Int$_C$	FW	TCCCGGCCCTaGATCTATGATCAAGATCGC CACACGG
	REV	GGCACAGTCGGAATTCttatgtgatgccagcag
ER-exit	FW	ctgaccgccacccaggacac
	REV	aaaGGCCGGCCTCACACCTCGTTCTCGTAG CAGAAgctggcggcgctgggcttc

2.1.4. Solutions and buffers

Name	Composition
CellMask Green plasma membrane stain	1:1000 dilution in PBS
CellMask Orange plasma membrane stain	1:1000 dilution in PBS
Cytosolic-like buffer	120 mM C5H8KNO4, 20 mM C2H3KO2, 10 mM C11H18N2O9, 4 mM MgCl2, 2 mM ATP, 0.5 mM DTT, 20 mM HEPES-KOH, pH 7.2
DRAQ5 labeling solution	1:1000 dilution in PBS

Fixing solution	4% PFA (w/v) in PBS
HEPES buffer	20 mM HEPES pH 7.4, 150 mM NaCl
Hoechst 34580 labeling solution	5 ng ml^{-1} Hoechst 34580 in PBS
MitoTracker labeling solution	200 nM MitoTracker in PBS
MitoTracker stock solution	1 mM MitoTracker in DMSO
Poly-D-lysine solution	10% (v/v) in PBS
Patch-Clamp bath solution	120 mM NaCl, 2.5 mM KCl, 25 mM NaHCO3, 2 mM CaCl2, 1 mM MgCl2, 25 mM glucose, 10 mM TEA, 2 mM 4-AP, 0.5 mM BaCl2, 1 mM NiCl2, 0.0005 mM TTX. pH 7.4, 305 mOsm
Patch-Clamp pipette solution	130 mM C6H11KO7, 20 mM KCl, 3 mM MgCl2, 1 mM CaCl2, 10 mM HEPES, 10 mM EGTA, 2 mM Mg-ATP, pH 7.25, 290 mOsm
QD labeling blocking solution 1	1% BSA
QD labeling blocking solution 2	6% BSA/10% horse serum in PBS
QD labeling blocking solution 3	10% horse serum
Quenching buffer	1 M Glycine, pH 6.5
Sonication buffer (4×)	500 mM C5H8KNO4, 80 mM CH3COOK, 40 mM EGTA, 80 mM HEPES, pH 7.2
TMA-DPH staining solution	2 µM TMA-DPH in PBS
VHH-LPETG-His (VHH Enhancer)	12.9 mg ml^{-1} in HEPES buffer

2.1.5. Materials and reagents for EM

Name	Company
Carbon Gilder Finder Grids (Cat. No. CF200F1-Au-ET, Type F1, extra thick)	Electron Microscopy Sciences, Hatfield, USA
EM gird storage box	Electron Microscopy Sciences, Hatfield, USA
Fine-tipped tweezers	Electron Microscopy Sciences, Hatfield, USA
Parafilm	VWR, Radnor, USA
Uranyl acetate	Science Service, Düsseldorf, Germany

Uranyl formate	Science Service, Düsseldorf, Germany
Whatman® qualitative filter paper (Grade 1, 4, 41, 42, 43 and 50)	Sigma-Aldrich, USA

2.1.6. Equipment

Name	Company
16/600 Superdex 200 gel filtration column	Hiload, Sweden
Amicon Ultra-15 centrifuge filter	Sigma-Aldrich, USA
Amicon Ultra-4 centrifuge filter	Sigma-Aldrich, USA
Analytical Balance	VWR, Radnor, USA
Axopatch 200B amplifier	Molecular devices, USA
Balance EG420-3NM	Kern EG, Balinaen, Germany
Cell-culture hood MERA Safe KS	Thermo Fisher Scientific, Waltham, USA
Cell-culture hood MSC-Advantage	Thermo Fisher Scientific, Waltham, USA
Cell-culture incubator	Thermo Fisher Scientific, Waltham, USA
Digidata 1440A Digitizer	Molecular devices, USA
Eppendorf tubes	Eppendorf AG, Hamburg, Germany
Fluorescence microscope	Olympus, Japan
Humidity chamber	Thermo Fisher Scientific, Waltham, USA
JEM-2200FS electron microscope	JEOL, USA
Laboclav Autoclave	Steriltechnik AK, Hückeswagen, Germany
Leica sp8 AOTF confocal microscope	Leica Microsystems GmbH, Germany
Leica sp8 Lightning confocal microscope	Leica Microsystems GmbH, Germany
Mikro 200 Centrifuge	Hettich, Kirchlengern, Germany
MiliQ-Ultrapure water Advantage A10	Millipore, Burlington, USA
NAP-5 columns	Amersham Biosciences, Little Chalfont, England
Olympus IX81 widefield microscope	Olympus, Tokyo, Japan
PCR machine MY Cycler	BioRad, Hercules, USA

PCR machine T300	Biometra, Göttingen, Germany
pH-Meter, SevenCompact	Mettler Toledo, Columbus, USA
Polymax 1040 shaker	Heidolph, Schwabach, Germany
Rotina 420R Centrifuge	Hettich, Kirchlengern, Germany
Sub-Cell GT agarose Gel Electrophoresis system	BioRad, Hercules, USA
Vibra-cell high-intensity ultrasonic processor	Sonics, Newtown, USA
Vortex-Genie 2 Vortexer	Scientific Industries Inc, New York, USA
Zeiss Axio observer A1 inverse microscope	Carl Zeiss, Oberkochen, Germany

2.2. Molecular cloning

2.2.1. Engineering of split GFP system

In this research, a split green fluorescent protein (GFP) system is established that allows easy detection of successful intein trans-splicing in living cells. Specifically, GFP is divided into two spontaneously assembling parts that form the fluorescent fluorophore: the GFP_N-fragment, which contains the three residues that constitute GFP chromophore, and the GFPc-fragment essential for chromophore maturation. These two halves of the split GFP are linked directly to the N- and C-terminal parts of the split intein, and trans-splicing interaction leads to the formation of GFP fluorophore. In this experiment, we explored the use of DnaE split intein from *Synechocystis sp. PCC6803* (named *Ssp*Int) for the intracellular reconstitution of split GFP. We examined the efficiency of the fluorophore formation by testing two different split-GFP variants: split superfolder GFP (sfGFP) dissected at the 11^{th} β-strand (addgene plasmid #34911) (Kim et al., 2012) and split enhanced GFP (EGFP) dissected at the 8^{th} β-strand (addgene plasmid #32601) (Rhee et al., 2006) (Detailed sequences of split GFP, refer to **Table 2.1**).

Table 2.1 Sequences of split GFP.

Name	Sequence
sfGFP GFP_N	ATGTCCAAGGGAGAAGAGTTGTTTACTGGCGTAGTCCCTATTCTCGTGGAACT CGATGGTGACGTGAATGGCCATAAGTTTTCTGTCAGAGGAGAGGGAGAAGGC GATGCCACCATCGGGAAACTCACGCTGAAATTCATCTGTACCACTGGAAAACT TCCCGTGCCTTGGCCAACCCTCGTGACAACACTCACCTACGGGGTGCAATGTT TCTCTCGGTACCCGGACCATATGAAGAGGCATGACTTCTTCAAGAGTGCCATG CCCGAGGGTTACGTTCAGGAGCGCACCATCTCTTTTAAGGACGATGGCAAATA TAAGACAAGAGCAGTCGTCAAGTTCGAGGGTGATACACTCGTTAACCGCATCG AGCTCAAAGGCACCGATTTTAAGGAGGACGGAAATATCCTGGGACACAAATTG GAGTACAACTTCAACAGTCACAACGTGTATATTACAGCAGATAAGCAGAAGAAT GGCATAAAGGCCAATTTCACGGTAAGACATAATGTCGAGGATGGCAGTGTCCA GCTGGCAGACCACTACCAGCAAAACACGCCCATTGGCGATGGACCTGTTCTC CTGCCAGACAACCACTACCTCAGTACCCAAACAGTCCTGTCCAAGGACCCTAA TGAGAAAGGGACG
sfGFP GFP_C	cgcgaccacatggtgctgcacgaatatgtgaacgctgctggcatcaca
EGFP GFP_N	ATGGTGAGCAAGGGCGAGGAGCTGTTCACCGGGGTGGTGCCCATCCTGGTC GAGCTGGACGGCGACGTAAACGGCCACAAGTTCAGCGTGTCCGGCGAGGGC GAGGGCGATGCCACCTACGGCAAGCTGACCCTGAAGTTCATCTGCACCACCG GCAAGCTGCCCGTGCCCTGGCCCACCCTCGTGACCACCCTGACCTACGGCGT GCAGTGCTTCAGCCGCTACCCCGACCACATGAAGCAGCACGACTTCTTCAAGT CCGCCATGCCCGAAGGCTACGTCCAGGAGCGCACCATCTTCTTCAAGGACGA CGGCAACTACAAGACCCGCGCCGAGGTGAAGTTCGAGGGCGACACCCTGGT GAACCGCATCGAGCTGAAGGGCATCGACTTCAAGGAGGACGGCAACATCCTG GGGCACAAGCTGGAGTACAACTACAACAGCCACAACGTCTATATCATGGCCGA CAAGCAGAAG
EGFP GFP_C	AACGGCATCAAGGTGAACTTCAAGATCCGCCACAACATCGAGGACGGCAGCG TGCAGCTCGCCGACCACTACCAGCAGAACACCCCCATCGGCGACGGCCCCGT GCTGCTGCCCGACAACCACTACCTGAGCACCCAGTCCGCCCTGAGCAAAGAC CCCAACGAGAAGCGCGATCACATGGTCCTGCTGGAGTTCGTGACCGCCGCCG GGATCACTCTCGGCATGGATGAACTATAC

2.2.1.1. **Cloning of mCherry::T2A::GFP$_N$::*Ssp*Int$_N$**

For cloning of mCherry::T2A::GFP$_N$::*Ssp*Int$_N$, mCherry-T2A-HypB-CAG vector harboring a 'self-cleaving' T2A peptide (thosea asigna virus 2A) was employed and restricted with BglII and EcoRI. PCR-amplified GFP$_N$ and *Ssp*Int$_N$ fragments were then inserted into the digested vectors using In-Fusion cloning technology (Life Technologies).

Primers for cloning of mCherry::T2A::sfGFP::*Ssp*Int$_N$ were:

Primer	Sequence
sfGFP$_N$ FW	5´-TCCCGGCCCTaGATCTATGTCCAAGGGAGAAGAGTTGTTTACT-3´
sfGFP$_N$ REV	5´-CTGAGGCACGTCCCTTTCTCATTAGGGTCCT-3´
*Ssp*Int$_N$ FW1	5´-AGGGACGTGCCTCAGTTTTGGCACCG-3´
*Ssp*Int$_N$ REV1	5´-GGCACAGTCGGAATTCTTATTTAATTGTCCCAGCGT-3´

Primers for the cloning of mCherry::T2A::EGFP$_N$::*Ssp*Int$_N$ were:

Primer	Sequence
EGFP$_N$ FW	5´-TCCCGGCCCTaGATCTATGGTGAGCAAGGGCGAG-3´
EGFP$_N$ REV	5´-CTGAGGCAgtattctgcgaaCTTCTGCTTGTCG-3´
*Ssp*Int$_N$ FW2	5´-agaatacTGCCTCAGTTTTGGCACCGAA-3´
*Ssp*Int$_N$ REV2	5´-GGCACAGTCGGAATTCTTATTTAATTGTCCCAGCGT-3´

2.2.1.2. **Cloning of mTagBFP2::T2A::*Ssp*Int$_C$::GFP$_C$**

To generate construct of mTagBFP2::T2A::*Ssp*Intc::GFPc, mTagBFP2-T2A-HypB-CAG vector was restricted with BglII and EcoRI, *Ssp*Intc::GFPc fragments were synthesized from Invitrogen GeneArt (for specific coding sequences refer to **Table 2.2**).

Fragment *Ssp*Intc::sfGFPc were amplified with primers:

Primer	Sequence
*Ssp*Intc::sfGFPc FW	5´-TCCCGGCCCTaGATCTATGGTTAAAGTTATCGGTCGTCGT-3´
*Ssp*Intc::sfGFPc REV	5´-GGCACAGTCGGAATTCttatgtgatgccagcagcgt-3´

Fragment *Ssp*Intc::EGFPc were amplified with primers:

Primer	Sequence
*Ssp*Intc::EGFPc FW	5´-TCATTTTGGCAAGCTTATGGTTAAAGTTATCGGTCGTCGT-3´
*Ssp*Intc::EGFPc REV	5´-GACACCATAGGGCCGGGATTCTCCT-3´

Amplified PCR fragments of *Ssp*Intc::GFPc were then subcloned into the restricted vector using In-Fusion cloning technology (Life Technologies).

Table 2.2 Sequence of *Ssp*Intc::GFPc

Name	**Sequence**
***Ssp*Int$_C$::sfGFP$_C$**	ATGGTTAAAGTTATCGGTCGTCGTTCCCTCGGAGTGCAAAGAATATTTGAT ATTGGTCTTCCCCAAGACCATAATTTTCTGCTAGCCAATGGGGCGATCGC CGCCAATcgcgaccacatggtgctgcacgaatatgtgaacgctgctggcatcaca
***Ssp*Int$_C$::EGFP$_C$**	ATGGTTAAAGTTATCGGTCGTCGTTCCCTCGGAGTGCAAAGAATATTTGAT ATTGGTCTTCCCCAAGACCATAATTTTCTGCTAGCCAATGGGGCGATCGC CGCCAATtgctttaataagtcacacAACGGCATCAAGGTGAACTTCAAGATCCGCC ACAACATCGAGGACGGCAGCGTGCAGCTCGCCGACCACTACCAGCAGAA CACCCCCATCGGCGACGGCCCCGTGCTGCTGCCCGACAACCACTACCTG

*Ssp*Int$_C$ sequence GFP$_C$ sequence

2.2.1.3. **Cloning of *Ssp*Int$_C$::GFP$_C$::T2A::mTagBFP2**

To explore whether T2A sequence would affect protein trans-splicing, construct of *Ssp*Intc::GFP$_C$::T2A::mTagBFP2 was cloned. *Ssp*Intc::GFPc::T2A fragments were synthesized from Invitrogen GeneArt (cloning sequences were listed in **Table 2.3**). For construct *Ssp*Intc::sfGFP$_C$::T2A::mTagBFP2, *Ssp*Intc::sfGFP$_C$::T2A and mTagBFP2 were amplified using the following primers:

Primer	Sequence
SspIntc::sfGFPc::T2A FW	5´-TCATTTTGGCAAGCTTATGGTTAAAGTTATCGGTCGTCGT-3´
*Ssp*Intc::sfGFPc::T2A REV	5´-GACACCATAGGGCCGGGATTCTCCT-3´
mTagBFP2 FW1	5´-CGGCCCTATGGTGTCTAAGGGCGAAGAGCT-3´
mTagBFP2 REV1	5´-GGCACAGTCGGAATTCttaATTAAGCTTGTGCCCCAGTTTG-3´

To clone *Ssp*Intc::EGFP$_C$::T2A::mTagBFP2, *Ssp*Intc::EGFP$_C$::T2A and mTagBFP2 were amplified using the following primers:

Primer	Sequence
*Ssp*Intc::EGFPc::T2A FW	5´-TCATTTTGGCAAGCTTATGGTTAAAGTTATCGGTCGTCGT-3´
*Ssp*Intc::EGFP$_C$::T2A REV	5´-GACACCATAGGGCCGGGATTCTCCT-3´
mTagBFP2 FW2	5´-CGGCCCTATGGTGTCTAAGGGCGAAGAGC-3´
mTagBFP2 REV2	5´-GGCACAGTCGGAATTCttaATTAAGCTTGTGCCCCAGTTTGCT-3´

Table 2.3 Sequence of *Ssp*Intc::GFPc::T2A

Name	Sequence
***Ssp*Intc::sfGFPc ::T2A**	ATGGTTAAAGTTATCGGTCGTCGTTCCCTCGGAGTGCAAAGAATAT TTGATATTGGTCTTCCCCAAGACCATAATTTTCTGCTAGCCAATGGG GCGATCGCCGCCAATcgcgaccacatggtgctgcacgaatatgtgaacgctgctggcat cacagagggcagaggaagtcttctaacatgcggtgacgtGGAGGAGAATCCCGGCCC CT
***Ssp*Intc::EGFPc ::T2A**	ATGGTTAAAGTTATCGGTCGTCGTTCCCTCGGAGTGCAAAGAATAT TTGATATTGGTCTTCCCCAAGACCATAATTTTCTGCTAGCCAATGGG GCGATCGCCGCCAATtgctttaataagtcacacAACGGCATCAAGGTGAACT TCAAGATCCGCCACAACATCGAGGACGGCAGCGTGCAGCTCGCCG ACCACTACCAGCAGAACACCCCCATCGGCGACGGCCCCGTGCTGC TGCCCGACAACCACTACCTGAGCACCCAGTCCGCCCTGAGCAAAG ACCCCAACGAGAAGCGCGATCACATGGTCCTGCTGGAGTTCGTGA CCGCCGCCGGGATCACTCTCGGCATGGATGAACTATACaaggagggc agaggaagtcttctaacatgcggtgacgtGGAGGAGAATCCCGGCCCT

*Ssp*Intc sequence GFPc sequence T2A sequence

2.2.2. Optimizing protein trans-splicing with *Npu* DnaE intein

We further optimized protein trans-splicing with the naturally *Nostoc punctiforme* DnaE intein (named *Npu*Int). The sequence of *Npu*Int$_N$ (residues 1-102) was amplified from the genomic DNA of *Nostoc punctiforme* (ATCC 29133). To test the effect of native boundary sequence near the splicing junction, we inserted Gly-Ser (GS) prior to the junction site of *Npu*Int$_N$, generating the construct of GFP$_N$-GS-*Npu*Int$_N$. Besides, the native

C-extein sequence of Cys-Phe-Asn-Gly-Thr (CFNGT) was inserted after the junction site of *Npu*Int$_C$, resulting in the construct of *Npu*Int$_C$-CFNGT-GFP$_C$. For the cloning of GFP$_N$-GS-*Npu*Int$_N$, *Npu*Int$_N$ was synthesized by Invitrogen GeneArt and then amplified by *Npu*Int$_N$ FW (5´-TCCCGGCCCTaGATCTATGTCCAAGGGAGAAGAGTTGTTTACT-3´) and *Npu*Int$_N$ REV (5´-GGCACAGTCGGAATTCttaGTTAGGCAGGTTGT-3´). PCR products obtained were then cloned into the hypB-CAG vector using BglII and EcoRI restriction sites. For the cloning of *Npu*Int$_C$-CFNGT-GFP$_C$, *Npu*Int$_C$::sfGFPc was synthesized by Invitrogen GeneArt synthesis and then amplified using the *Npu*Int$_C$ FW (5´-TCCCGGCCCTaGATCTATGATCAAGATCGCCACACGG-3´) and *Npu*Int$_C$ REV (5´-GGCACAGTCGGAATTCttatgtgatgccagcag-3´). PCR fragments were then digested with BglII and EcoRI, and cloned into the hypB-CAG vector. All cloned constructs were sequenced using Eurofins Tubeseq services.

2.2.3. Modifying HCN1 with N-terminus and ER-exit signal

2.2.3.1. **Cloning of HCN1 with N-terminus**

The truncated HCN1 construct (mCherry::T2A::HCN1$_{\Delta N\Delta C}$::GFP$_N$::Int$_N$) was synthesized from VectorBuilder and restricted with BbVCI and BamHI, generating a new expression vector P1V2. HCN N-terminal fragment (Met1-Pro481) was synthesized from Invitrogen GeneArt synthesis, and then restricted and subcloned into the P1V2 vector using the BbVCI and BamHI restriction sites, generating N-HCN1 construct (mCherry::T2A::HCN1$_{\Delta C}$::GFP$_N$::Int$_N$).

2.2.3.2. **Cloning of HCN1 with ER-exit signal**

To fuse ER-exit signal peptide (CFNGT) to the C-terminus of mTagBFP2::T2A::Int$_C$::GFPc::streptavidin (P2V2), the synthesized fragment P2V2 was amplified using primers of ER-exit FW (5´-ctgaccgccacccaggacac-3´) and ER-exit REV (5´-aaaGGCCGGCCTCACACCTCGTTCTCGTAGCAGAAgctggcggcgctgggcttc-3´), after which amplified PCR fragments were then digested with PstI and FseI and subcloned into the P2V2 vector.

2.3. Split GFP reconstitution assays in HEK293 cells

The split GFP reconstitution strategy is to link GFP_N with N-half of a protein splicing system (Int_N), and GFPc with C-half of a protein splicing system (Int_C). Both constructs were respectively fluorescently tagged with mCherry and mTagBFP2, generating constructs mCherry::T2A::GFP_N::Int_N and mTagBFP2::T2A::Int_C::GFP_C. For the optimization of split GFP reconstitution efficiency, various combinations of split GFP (split sfGFP and spit EGFP) as reporter system and split intein (*Ssp*Int and *Npu*Int) as trans-splicing system were tested (refer to Table 2.4).

Table 2.4 Split GFP reconstitution pairs

N-half Construct	C-half Construct
sfGFP_N - *Ssp*Int_N	*Ssp*Int_C - sfGFP_C
EGFP_N - *Ssp*Int_N	*Ssp*Int_C - EGFP_C
sfGFP_N - *Npu*Int_N	*Npu*Int_C - sfGFP_C
sfGFP_N - *Npu*Int_N	*Ssp*Int_C - sfGFP_C
sfGFP_N - *Ssp*Int_N	*Npu*Int_C - sfGFP_C

HEK293 cells (ATCC CRL-1573) were grown in 24-well plate on coverslip coated with Poly-D-lysine (Sigma-Aldrich, Cat. No. p1149) and co-transfected with N-half construct (mCherry::T2A::GFP_N::Int_N) and C-half construct (mTagBFP2::T2A::Int_C::GFPc) at a concentration ratio of 1:1. 24-48 hours (h) later, cells were live imaged or fixed with 4% paraformaldehyde (PFA) mounted onto microscope slides in Aqua-Poly/Mount mounting medium (VWR, Cat. No. 87001-902). Images were taken on an inverted Zeiss Axio observer A1 inverse microscope (Carl Zeiss, Oberkochen, Germany) with 40× and 10× objectives. Bleedthrough was checked by taking images of cells with single transfection (mCherry::T2A::GFP_N::Int_N or mTagBFP2::T2A::Int_C::GFP_C) or no transfection and acquiring dual-channel images with the same imaging setting used for co-transfected cells. Excitation power and gain were adjusted identically between the co-transfected, single-transfected, and non-transfected cells. Split GFP reconstitution efficiency was assessed as GFP fluorescence intensity relative to the fluorescence intensity of N-half construct (mCherry::T2A::GFP_N::Int_N).

2.4. Membrane expression of HCN1 channel

HEK293 cells were grown in T-75 cell-culture flask (Greiner Bio-One, Frickenhausen, Germany) with Dulbecco's Modified Eagle Medium (DMEM) supplemented with 10% fetal bovine serum, streptomycin (100 units ml^{-1}, Thermo Fisher Scientific), and penicillin (100 µg ml^{-1}, Thermo Fisher Scientific). HEK293 cell line stably expressing HCN1 lattice (A6 cell line) was cultured with antibiotic selection medium containing puromycin (3 µg ml^{-1}, Life Technology) and blasticidin (5 µg ml^{-1}, Life Technology). Flasks were incubated at 37 ℃ in 5% CO_2 and subcultured every 2-3 days when cells reached around 80% confluency. The day before transfection, cells were passaged in a T-75 cell-culture flask and counted using the standard trypan blue exclusion method before plating about 1×10^5 cells in 500 µl growth medium per well of a 24-well culture plate (VWR, Radnor, USA). The next day, cells were transfected (500 µg DNA per well) using Lipofectamine 3000 transfection reagent (Thermo Fisher Scientific, Cat. No. L3000-008) when reaching about 80% confluency. 24-48 h post-transfection, cells were live-imaged or fixed with 4% PFA. Transfection efficiency, as well as cell morphology and viability, were evaluated via fluorescence microscopes.

2.5. Confocal fluorescence imaging and analysis

For imaging of the transient expression of HCN1 lattice in HEK293 cells, cells were seeded at a density of 1×10^5 per well on Ø 12-mm glass coverslips in a 24-well plate (VWR, Radnor, USA), 24 h later cells were co-transfected with constructs of mCherry::T2A::HCN1::GFP_N::Int_N and mTagBFP2::T2A::Int_C::GFPc::streptavidin using Lipofectamine 3000 reagent (Thermo Fisher Scientific, Cat. No. L3000-008). For the determination of nuclear localization of GFP, cells were fixed either 24 h or 48 h post-transfection before fluorescent labeling with DRAQ5 labeling solution (Thermo Fisher Scientific, Cat. No. 62254). DRAQ5 was diluted 1:1000 with phosphate-buffered saline (PBS) to a concentration of 5 µm and added to the cell culture. After incubation for 5 minutes (min) at room temperature (RT) in the dark, cells were rinsed once in PBS and fixed with 4% PFA. Cell samples were then mounted onto the microscope slides in Aqua-Poly/Mount mounting medium and imaged with Leica sp8 AOTF confocal microscope (Leica Microsystems GmbH, Germany), equipped with 10×/0.40 NA dry objective, 40×/1.1

water immersion objective, and 63×/1.3 glycerol immersion objective. mTagBFP2, GFP, mCherry, and DRAQ5 were excited with Diode 405 nm, OPSL 488 nm, OPSL 552 nm, and Diode 638 nm laser line, and by using TD 488/552/638 excitation beam splitter.

2.6. Establishment of stable HCN1 lattice cell line

To generate HEK293 cell line that stably expressed HCN1 lattice constructs, HCN1::GFP_N::Int_N and Int_C::GFPc::streptavidin constructs were cloned into expression vectors carrying puromycin and blasticidin resistant genes, respectively. Both plasmids were co-transfected in HEK293 cells in 6-well culture plates using Lipofectamine 3000 reagents (Thermo Fisher Scientific, Cat. No. 62254) following the manufacturer's instructions. 48 h after transfection, cells were transferred into three 90 mm culture dishes (VWR, Radnor, USA). The next day, antibiotics with concentration gradient (blasticidin 1-5 μg ml^{-1}, puromycin 0.5-3 μg ml^{-1}, Thermo Fisher Scientific) were added to the selection culture medium. After culture in the selection medium for 4-6 weeks, resistant cell clones were picked and transferred to a 96-well culture plate (VWR, Radnor, USA). Monoclonal cell colonies with the modest expression of reconstituted GFP were isolated and expanded into larger cell culture volumes. HCN1 lattice functionality was validated by patch-clamp recording technique, after which cells were cultured in complete medium supplemented with 5 μg ml^{-1} blasticidin and 1.5 μg ml^{-1} puromycin at 37 ℃, 5% CO_2. For extended storage, cells in complete medium with 10% Dimethyl sulfoxide (DMSO) were kept in liquid nitrogen.

2.7. Electrophysiological recording

HEK293 cells were cultured on coverslips placed in a 24-well plate and transiently transfected with expression vectors encoding either of these constructs: (i) full-length HCN1, (ii) mCherry::T2A::HCN1::GFP_N::Int_N, or (iii) co-transfected with mCherry::T2A::HCN1::GFP_N::Int_N and mTagBFP2::T2A::Int_C::GFP_C::streptavidin with a concentration ratio of 1:1 using Lipofectamine 3000 reagents (Thermo Fisher Scientific, Cat. No. L3000-008) according to manufacturers' instructions. Cells were cultured in DMEM supplemented with 10% fetal bovine serum and kept at 37 ℃, 5% CO_2. After 24 h incubation, cells grown on coverslips were transferred to a recording chamber, and

currents were recorded using the whole-cell patch-clamp recording technique at RT (23 ±1 ℃). The extracellular (bath) solution contained (in mM): 120 NaCl, 2.5 KCl, 25 $NaHCO_3$, 2 $CaCl_2$, 1 $MgCl_2$, 25 glucose, 10 TEA, 2 4-AP, 0.5 $BaCl_2$, 1 $NiCl_2$, 0.0005 TTX, pH adjusted to 7.4 with NaOH; 305 mOsm. Patch pipettes were pulled from borosilicate glass and had a resistance of 3-5 MΩ when filled with intracellular (pipette) solution, which contained (in mM): 130 C6H11KO7, 20 KCl, 3 MgCl2, 1 CaCl2, 10 HEPES, 10 EGTA, 2 Mg-ATP, pH adjusted to 7.25 with KOH; 290 mOsm.

The membrane potential was held at -40 mV. For the voltage-dependent activation, cells were hyperpolarized from -140 to -30 mV in 10 mV increments for 5 seconds (s), followed by a step to -140 mV. The amplitude of I_h was measured as the difference between the steady-state current at the end of each test potential and the instantaneous current immediately following each test potential. The current density was calculated as the amplitude divided by the cell capacitance obtained by the capacitance compensation function of the amplifier. The kinetics of I_h activation (τ_{act}) contained a fast and a slow component, and was obtained by fitting bi-exponential functions of the form:

$$f(t) = \Sigma\ Ai*e^{-t/\tau i} + c.\ i=1\ or\ 2 \qquad \text{(Eq.1)}$$

where $\tau 1$ and $\tau 2$ are the fast and slow time constants of activation, respectively. The fast component $\tau 1$ is consequently referred to as τ_{act} since it accounts for > 90% of the current amplitude, thus the fast component represents the kinetics-determining component of the HCN channels (Ishii et al., 2001).

For the determination of voltage-dependent activation, tail currents (I_{tail}) were measured as the current amplitude immediately after the final step to -140 mV. The conductance was calculated according to the equation:

$$G = I_{tail}/(V_m - E_{rev}) \qquad \text{(Eq.2)}$$

where G is the conductance, I_{tail} is HCN tail current, V_m is the test pulse potential, and E_{rev} is the reversal potential of I_{tail}. The conductance-voltage curves were then fitted with a Boltzmann function of the form:

$$f(V) = 1/(1+e^{-(V-V50)/slope}) \qquad \text{(Eq.3)}$$

with V50 being the voltage of half-maximal activation.

For the determination of reversal potential (E_{rev}), cells were fully activated by hyperpolarizing from holding voltage of -40 to -130 mV for 2 s, after which a series of test pulse ranging from -100 mV to +40 mV were applied in 20 mV increments. The instantaneous current amplitudes upon the steps to more depolarized levels (tail currents) were plotted versus the corresponding command potentials and submitted to linear regression analysis in GraphPad Prism8. The intercept of the resulting line with the X-axis represents the E_{rev}.

Data were acquired with an Axopatch 200B amplifier, a Digidata 1440A digitizer, and pCLAMP10 software (Molecular Devices). The recording was sampled at 5 kHz and low-pass filtered at 1 kHz. pClamp10 and Graphpad Prism8 software were used for data analysis. All values are given as mean ± SE; *p* values < 0.05 were considered significant.

2.8. Membrane sheet preparation

2.8.1. Generation of membrane sheet by sonication

EM finder grids (Electron Microscopy Sciences, Cat. No. CF200F1-Au-ET, Type F1) were coated with Poly-D-lysine for 2 h at 37 ℃ before being washed with Mili-Q-water. One day before membrane sheeting, cells were seeded on EM grids placed in Ø 60 mm cultural dishes and cultured for 34-36 h till reaching a monolayer of cells with 80% confluency. On the day of sonication, EM grids were placed into ice-cold sonication buffer (500 mM potassium glutamate, 80 mM potassium acetate, 40 mM EGTA, 80 mM HEPES, pH 7.2) with a liquid column of 1 cm after being washed twice with ice-cold PBS. The sonication tip was adjusted to various distances above the EM grid ranging from 0.5-1 cm. Each time before sonication, tip distance was measured to ensure the reproducibility of the unroofing results. Sonication parameters, including sonication duration (ranging 0.1-1 s) in combination with 15-25% intensity (% of the maximal output power) for 1-2 cycles, were tested to optimize unroofing efficiency. The optimal sonication condition was expected to ensure membrane patch yield with good preservation of the EM carbon film, which may vary substantially for each experiment, depending on cell vitality, density, and adhesion. After sonication, EM grids were rinsed twice with cytosolic-like buffer (20 mM potassium acetate, 120 mM potassium glutamate, 10 mM 1,3-Diaminopropanol tetraacetic acid, 20 mM HEPES-KOH, 4 mM MgCl2, 2 mM ATP, 0.5 mM DTT, pH 7.2)

(Barszczewski et al., 2008) and immediately transferred to the same buffer to prevent dry-out of the membrane patches. Afterward, the membrane patches were incubated for 10 s at RT with TMA-DPH (2 µm in PBS, Thermo Fisher Scientific, Cat. No. T204) before microscopic examination.

2.8.2. Generation of membrane sheet by paper blotting

EM grids (Electron Microscopy Sciences, Cat. No. CF200F1-Au-ET, Type F1) and cells were prepared as described in the sonication method part. For the paper blotting procedures, cells were rinsed in the culture dish with a cytosolic-like buffer, after which the EM grid was then removed from the dish with tweezers, and a 6-µl drop of cytosolic-like buffer was added to the cell-side of EM gird before blotting against the filter paper. This step was repeated 1-2 times to ensure efficient membrane patches production. After paper-blotting procedures, samples were rinsed by dipping 2-3 times in the cytosolic-like buffer. Six different Whatman® qualitative filter papers with variable grammage and thickness were tested to optimize unroofing efficiency (details see **Table 3.1**). The paper blotting quality was assessed based on the membrane patch yield and the preservation of the EM grid carbon film.

2.8.3. Validation of membrane sheet

2.8.3.1. **Cell labeling for membrane sheet validation**

It is of critical importance to validate the membrane sheet before the samples processed for more time-consuming EM preparation; thus, a systematic validation system was established using wild-type (WT) HEK293 cells and further optimized in the HEK293-A6 cell line stably expressing HCN1 lattice.

For the validation of membrane sheet generated from WT HEK293 cells, cells were cultured on the EM grid (Electron Microscopy Sciences, Cat. No. CF200F1-Au-ET, Type F1) in Ø 60 mm culture dish till the cells reached 80% confluency the next day. After membrane sheeting procedures, cells were labeled with MitoTracker Orange CMTMRos (Thermo Fisher Scientific, Cat. No. M7510), CellMask Green plasma membrane stains (Thermo Fisher Scientific, Cat. No. C37608) and DRAQ5 labeling solution (Thermo Fisher Scientific, Cat. No. 62254) according to the manufacturer's protocols. MitoTracker Orange

CMTMRos was first dissolved in DMSO to a concentration of 1 mM and stored at -20 ℃ and further diluted to the final working concentration of 200 nM in PBS before use. After incubation at 37 ℃ for 20 mins, cells were washed once with PBS. For the membrane stain, CellMask Green plasma membrane stains were diluted 1:1000 with PBS and added to the cells. After incubation at 37 ℃ for 5 mins in the dark, cells were washed three times with PBS, each incubating for 10 mins. For the nucleus stain, DRAQ5 was diluted 1:1000 with PBS before adding to the cells. After incubation at 37 ℃ for 5 mins in the dark, cells were washed once with PBS.

For the validation of membrane sheet in the HEK293 HCN1-A6 cell line, cells were cultured on the EM grid in Ø 60 mm culture dishes till reaching around 80% confluency, after which cells were fluorescently labeled with Hoechst 34580 (Thermo Fisher Scientific, Cat. No. H21486) and CellMask Orange plasma membrane stain (Thermo Fisher Scientific, Cat. No. C10045) according to the manufacture's protocols. Hoechst 34580 was firstly dissolved in deionized water to create a 5 mg ml^{-1} stock solution and diluted 1:1000 in PBS before adding to the cells. After incubation at 37 ℃ for 5 mins, cells were washed three times with PBS. To fluorescently label cell membranes, CellMask Orange plasma membrane stain was first diluted 1:1000 in PBS before use. After incubation at 37 ℃ for 10 mins, cells were washed three times with PBS.

2.8.3.2. **Confocal imaging and analysis**

Membrane sheets, generated by paper blotting or sonication method, were fixed with 4% PFA and mounted on microscope slides for confocal imaging. Images were acquired on Leica SP8 Lightning super-resolution confocal microscope (Leica Microsystems GmbH, Germany), equipped with 40×/1.1 water immersion objective and 63×/1.20 water immersion objective. For imaging of membrane sheets in WT HEK293 cells, CellMask Green plasma membrane dye, MitoTracker Orange CMTMRos, and DRAQ5 were excited with the Argon laser line at 488 nm, 581 nm, and 633 nm. For imaging of membrane sheets generated from HEK293 HCN1-A6 cells, Hoechst 34580, CellMask Orange plasma membrane dye, and GFP were excited with Diode laser at 405 nm, and Argon laser line at 488 nm and 561 nm (for details see **Table 2.5**).

A montage of the entire grid was first obtained using a magnification of 10× by LAS X Navigator (Leica Microsystems GmbH, Germany) to locate a region of interest (ROI) that contained membrane patches with well-reserved carbon films. Selected mesh squares were then mapped at 63× magnification, and 2D-stack images were acquired with 40×/1.1 water immersion objective, with a voxel size of 0.135 µm on X-Y plane and a voxel size of 0.426 µm on the X-Z dimension, after which 3D reconstructions were obtained. Structures with positive membrane stain and negative nuclear stain in all Z-stack layers were validated as successful membrane patches, and structures with both positive membrane stain and nuclear stain were validated as incomplete membrane sheets or whole cells. After data collection, images were processed with LAS X integrated Lightning module to improve SNR and spatial resolution. For samples labeled with QDs, CLEM was applied for the identification of protein lattice on the membrane. Image analysis was performed with LAS X v3.5.5 and ImageJ 1.52p (NIH, USA) software.

Table 2.5 Summary of confocal imaging setting

Stain	Filter set	Ex/Em
Hoechst 34580	DAPI	392/440 nm
CellMask Orange plasma membrane dye	TRITC/RFP	554/567 nm
Cellmask Green plasma membrane dye	FITC/GFP	522/535 nm
MitoTracker Orange CMTMRos	TRITC/RFP	554/576 nm
DRAQ5 nuclear stain	DRAQ5	Ex 647 nm/Em 665 nm to infra-red
QD705	Cy5.5	Ex 350-633 nm/Em maxi 705 nm

2.9. Correlative light and electron microscopy

2.9.1. QD labeling

A variety of CLEM-probes have been developed over the years for the study of protein trafficking and localization. QDs, consisting of both the fluorescent and electron-dense components, enable an accurate correlation between the light and electron microscopy images for CLEM studies. With conjugation to antibodies, QDs allow the

specific labeling of biomolecular in fixed and live cells without compromising biomolecular function.

2.9.1.1. **QD-GFP nanobody conjugation**

250 µl QD705 (Thermo Fisher Scientific, Cat. No. Q21561MP) were transferred to Amicon Ultra-4 (100 kDa cutoff) ultrafiltration unit, and centrifuge was carried out at 4 °C, 4000 g until about 250 µl left (in 5 min steps). The ultrafiltration unit was refilled with 1× PBS and centrifuged again until the volume was reduced to the initial volume (~250 µl). QDs were then transferred to a glass vial, and 2.5 µl 100 mM BS3 (Sigma-Aldrich) (1/100 of the volume of QDs) was added to the QDs in the glass vial. After incubation at RT for 30 mins on a rotator, QD-BS3 was purified from excess cross-linker by buffer exchange on a pre-equilibrated NAP-5 column (Life Technologies) to 1× PBS. The elute was collected into a glass vial containing VHH (1.2 mg VHH in HEPES buffer), and mixed gently and incubated at RT for 2 h with a mild vortex. QD-VHH conjugate was then purified from excess VHH by gel filtration according to manufacturers' instructions (QDs were expected to lead to strong absorption at 280 nm and could be detected with the standard UV detector). Finally, unreacted BS3 sites on QD-VHH conjugates were quenched with 1 mM glycine by adding glycine to a final concentration of 50 mM and reacting for 15 mins. The QD-VHH-containing fraction was concentrated on the Amicon 100 kDa column to a final volume of 1.5 ml. After filtering through a 0.2 µm syringe filter, the final product was stored at 4 ℃. This QD-GFP nanobody conjugate was produced by the Nanobodies Core Facility, Bonn Technology Campus Life Sciences, University of Bonn.

2.9.1.2. **Cell preparation**

HEK293 HCN1-A6 cells were cultured on EM grids (Electron Microscopy Sciences, Cat. No. CF200F1-Au-ET, Type F1). Membrane sheets were generated by sonication or paper blotting methods (see details in Methods 2.8), followed by fixation (4% PFA, RT, 5 mins) and PBS wash for three times.

2.9.1.3. **QD staining**

Cells were incubated with blocking buffers for 1 h before QD labeling. For the optimization of the blocking condition, three different blocking solutions were tested: (i) 1%

BSA; (ii) 6%BSA/10% horse serum; (iii) 10% horse serum. After blocking, cells were incubated for 1 h with GFP-nanobody conjugated QD, diluted in blocking buffer with a series of titration from 1:10 to 1:10000. Afterward, cells were washed three times in PBS and labeled with Hoechst 34580 (Thermo Fisher Scientific, Cat. No. H21486) and CellMask Orange plasma membrane stain (Thermo Fisher Scientific, Cat. No. C10045) according to the manufacturer's protocol. Fluorescently labeled samples were then mounted on the microscope slides and stored in the dark at RT before imaging.

2.9.2. Fluorescence microscopy imaging

fLM images were acquired using Leica SP8 Lightning super-resolution confocal microscope (Leica Microsystems GmbH, Germany), equipped with 40×/1.1 water immersion objective and 63×/1.2 water immersion objective. QD705 was excited with Argon 633 nm laser line. An overview of the gird was first obtained by acquiring a montage using the LAS K software (Leica Microsystems GmbH, Germany). After the identification of ROI, both fluorescence images (including GFP, membrane and nuclear stain, QD705) and bright-field images were taken to indicate the position of the membrane patch on the grid. Z-stack scanning was performed to validate the generated membrane patch and to reveal the QD localization throughout the specimen.

2.9.3. EM imaging

Once fLM images were completed, the grids were processed for EM imaging. For negative staining, 2% (w/v) uranyl acetate was prepared and stored at -20 ℃ beforehand. Two droplets of staining solution were applied onto a sheet of parafilm. The sample was prestained by gently lowering the carbon grid surface to touch the first droplet, and the residual stain was blotted off with Whatman® Grade 1 filter paper. Subsequently, the sample was stained by placing on the second droplet for 20 s, and the excess stain was removed using the same type of filter paper. The grids were then air-dried for EM imaging.

Negative stained-samples were screened and imaged on the JEM-2200FS electron microscope (JEOL, USA), equipped with a 200 kV Schottky field emission gun and an F416 4 k×4 k CMOS detector (TVIPS GmBH, Germany). After the gird was inserted with a JEOL specimen quartet holder (EM-0170SQH), TEM images were

acquired either with EM-Menu 2.0 (TVIPS) or SerialEM software (https://bio3d.colorado.edu/SerialEM/). The sample was first imaged at low magnification under the low-dose condition to identify ROIs (montaging if necessary), approximately matching the field view of the fluorescence microscope. This montaged image was then roughly aligned with the fLM images using Fiji software (https://imagej.net/Fiji). Alternatively, the alignment of fLM and low-magnification TEM image could be performed by directly transporting the LM image data (fluorescence and DIC images) to the serialEM on the TEM operating computer. Selected areas in the LM images were aligned to the low-magnification TEM images acquired with SerialEM using the registration points. Following the identification of targeted subregions in the roughly CLEM images, TEM images at higher magnification were acquired to visualize the ultrastructure on the membrane.

2.9.4. Data acquisition and overlay for CLEM

In this study, a two-step LM-EM approach was applied for the CLEM study (**Figure 2.1**). First, membrane sheet with QDs labeling was imaged using a confocal microscope. After the identification of ROIs within the membrane, the sample was negative-stained and processed for EM. The final stage of the CLEM protocol involved the analysis and relocation of the same membrane patch identified at the LM stage, in the EM. This relocation process was mostly done manually with the aid of finder girds, CLEM probes, and typical cell features. To this aim, the sample was first imaged at low magnification to locate the ROIs, before increasing the magnification to visualize the ultrastructure on the membrane patch. Finally, image overlays of LM and EM images were created. Once suitable positions were determined, tomographic tilt series images could be acquired for subsequent cryo-ET analysis.

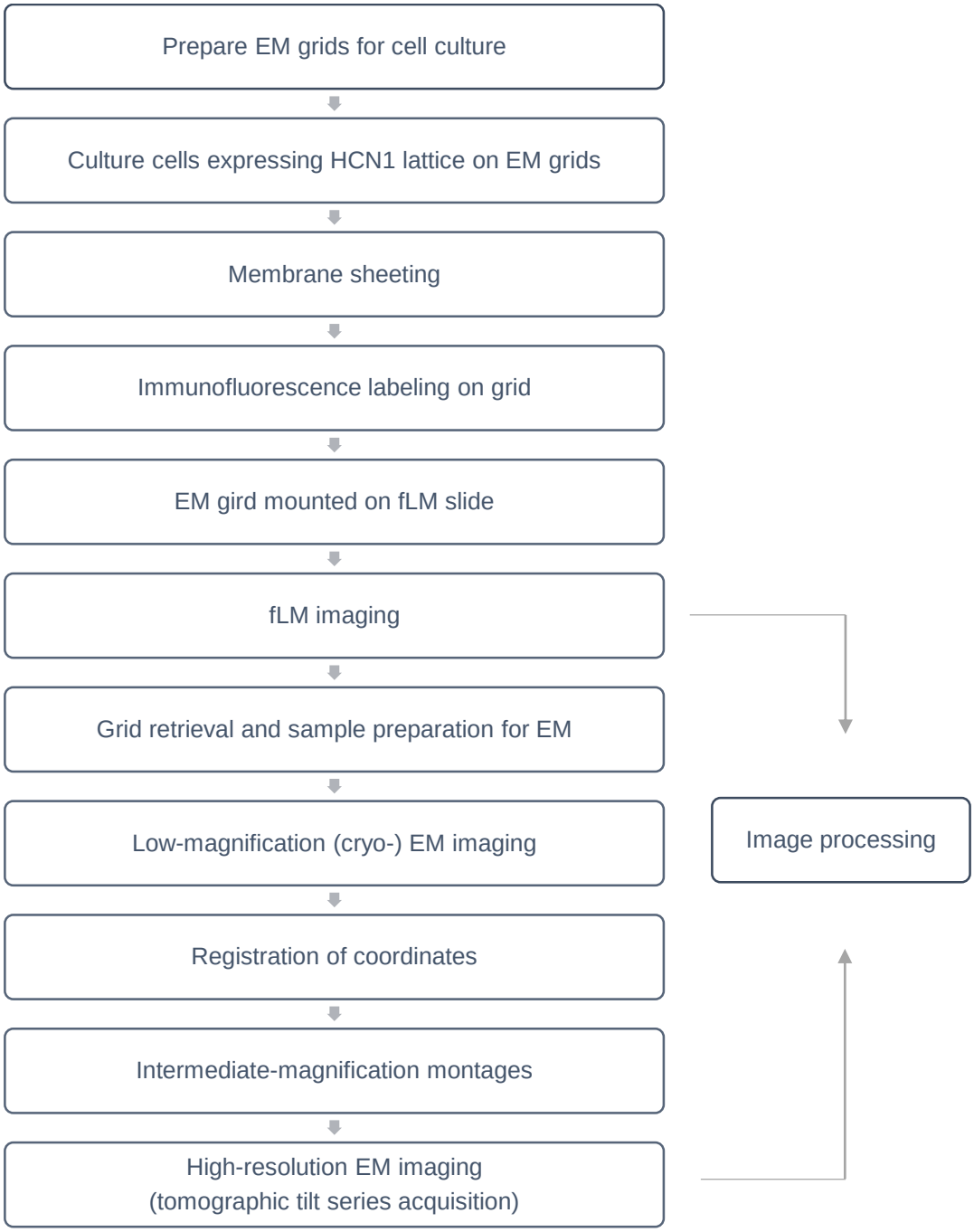

Figure 2.1 Workflow of CLEM techniques in this study.

This protocol begins with the culture of HEK293 cells on the EM grid. After membrane sheeting and immunofluorescence labeling, samples are evaluated by fLM to identify fluorescently tagged ROIs within the membrane. Next, the samples are negative-stained and prepared for TEM. Intermediate-magnification montages are acquired first. Coordinates from fLM and TEM are combined for correlation to facilitate high-resolution EM data collection. The image data from fLM and EM can be further processed for structural analysis.

3. Results

3.1. Forming of HCN1 lattice on the membrane

3.1.1. The general strategy for HCN1 lattice forming

The general strategy is to use split intein to crosslink channels into a structural lattice. In this system, the intein system is used to link tetrameric channels via their carboxy-terminal regions to a tetrameric modified streptavidin. To achieve this aim, we generated two components: the first component (channel component) is to link channel with N-half of split intein (Int_N), resulting in HCN1-$(GGS)_x$-GFP_N-Int_N, and the second component (linker component) is to generate a linker hub consisting of a streptavidin molecule coupled to the C-half of split intein moiety (Int_C), resulting in Intc-GFPc-(GGS)x-streptavidin. We applied a streptavidin dead variant containing three mutations (N23A, S27D, S45A) that block biotin-binding (Addgene plasmid # 20859). For both constructs, a GGS linker with X number of repeats, $(GGS)_x$, was applied to bridge HCN1-GFP_N and GFPc-streptavidin. Assembly of both components would be expected to lead to a symmetric, four-sided protein lattice (**Figure 3.1**).

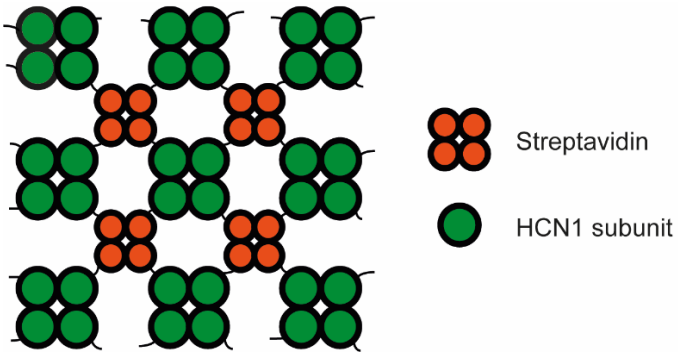

Figure 3.1 Schematic illustration of HCN1 lattice.

HCN1 channel construct was truncated at both at the N- and C-terminus to obtain a regular protein lattice structure. For the identification of boundary sequence, human HCN1 sequence (UniProt-ID #O60741) was aligned to the sequence of homologous proteins, including rat Eag1 (UniProt-ID #Q63472), C.elegans TAX-4 (Uniprot-ID #Q03611), human CNGA3 (UniProt-ID #Q16281) and human CNGB3 (Uniprot-ID #Q9NQW8), using Clustal Omega alignment. The alignment results showed that the likely

N-terminal boundary was W133 based on PDB structure, and D140 based on SSE prediction; we took Ile 135 as the start of the delta-N construct. The possible C-terminal boundary was I594 based on PDB structure, and N598 based on SSE prediction; we took human HCN1 S599 as the stop of the delta-C construct (**Figure 3.2**).

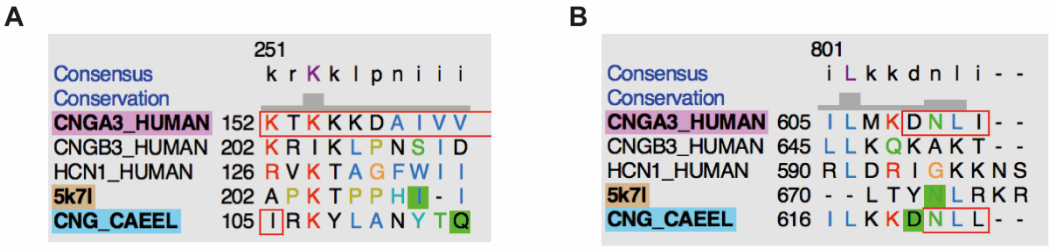

Figure 3.2 Boundary of HCN1 by sequence alignment.

Linkers are an indispensable component in the construction of stable, bioactive fusion proteins. The fusion site, as well as the length and structure of linkers, affect the stability and bioactivity of fusion proteins. As the N-terminus of the delta-N construct () was very close to the lipid-membrane surface, which could lead to steric problems, we used the delta-C construct for attaching fusion linkers.

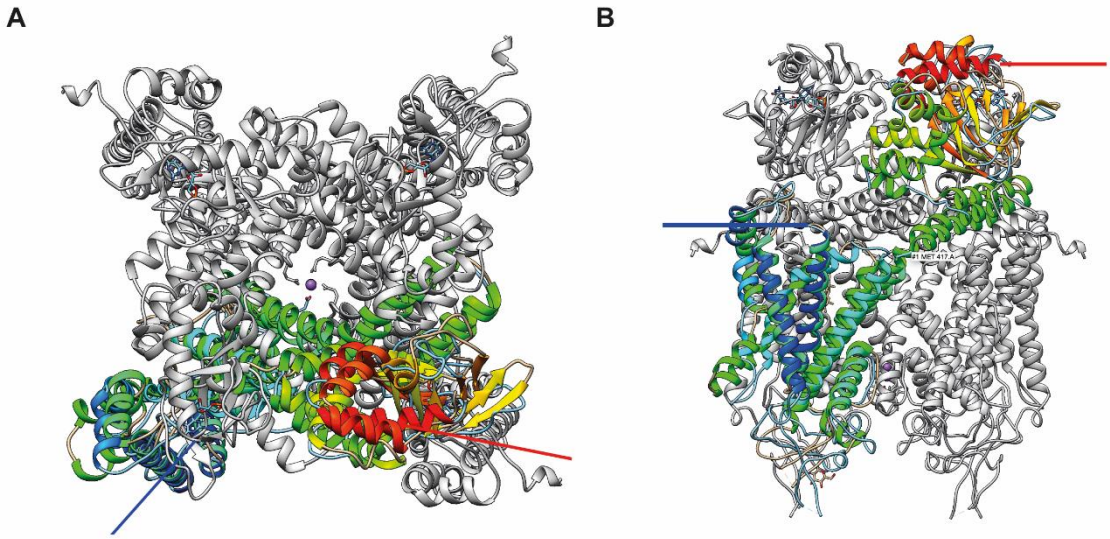

Figure 3.3 Determination of best site for attaching fusion linkers.

Top view (A) and side view (B) of HCN1 subunit. The directions of C-terminus and N-terminus (after truncation as above) are shown in red and blue. Figure by Prof. Dr. Elmar Behrmann.

To provide maximal flexibility and solubility of the functional fusion proteins, we designed a flexible 'GS' linker with the sequence of $(Gly\text{-}Gly\text{-}Ser)_X$ to bridge HCN1 and GFP. By adjusting the copy number 'X,' the length of the GS linker can be optimized to achieve appropriate separation of the functional domains. The distance HCN1-C to N-GFP should be at least 10 Å to prevent GFP from bumping on the CNBD of HCN1. Assuming the length of a GGS repeat is 0.5 nm/5 Å if equilibrated; thus, two or more GGS are needed (as shown in **Figure 3.4**), suggesting the linker length of $(GGS)_2$, $(GGS)_4$, and $(GGS)_8$ should be tested. However, in an optimal lattice, the streptavidin would sit on the corner of HCN1. Thus, likely a longer HCN1-GFP linker is required to prevent steric clashes between GFP and streptavidin. A better arrangement would be this (**Figure 3.5**): here, HCN-C to N-GFP distance is increased to ~12 Å (3×GGS), and GFP-C to N-streptavidin distance would be ~14 Å (3×GGS). Thus for both HCN-C to N-GFP, as well as for C-GFP to N-streptavidin, $(GGS)_3$, $(GGS)_6$, $(GGS)_{12}$ should be tested. In our study, the linker length of $(GGS)_6$ was tested first.

To sum up, the general strategy for forming HCN1 lattice is based on the split intein system to cross-link the channel component via the linker hub. For the optimal lattice formation, appropriate boundary sequence, as well as linker length and fusion site, are of critical importance. Split GFP with enhanced folding robustness is utilized to report on the successful trans-splicing reaction, therefore the formation of the protein lattice on the membrane.

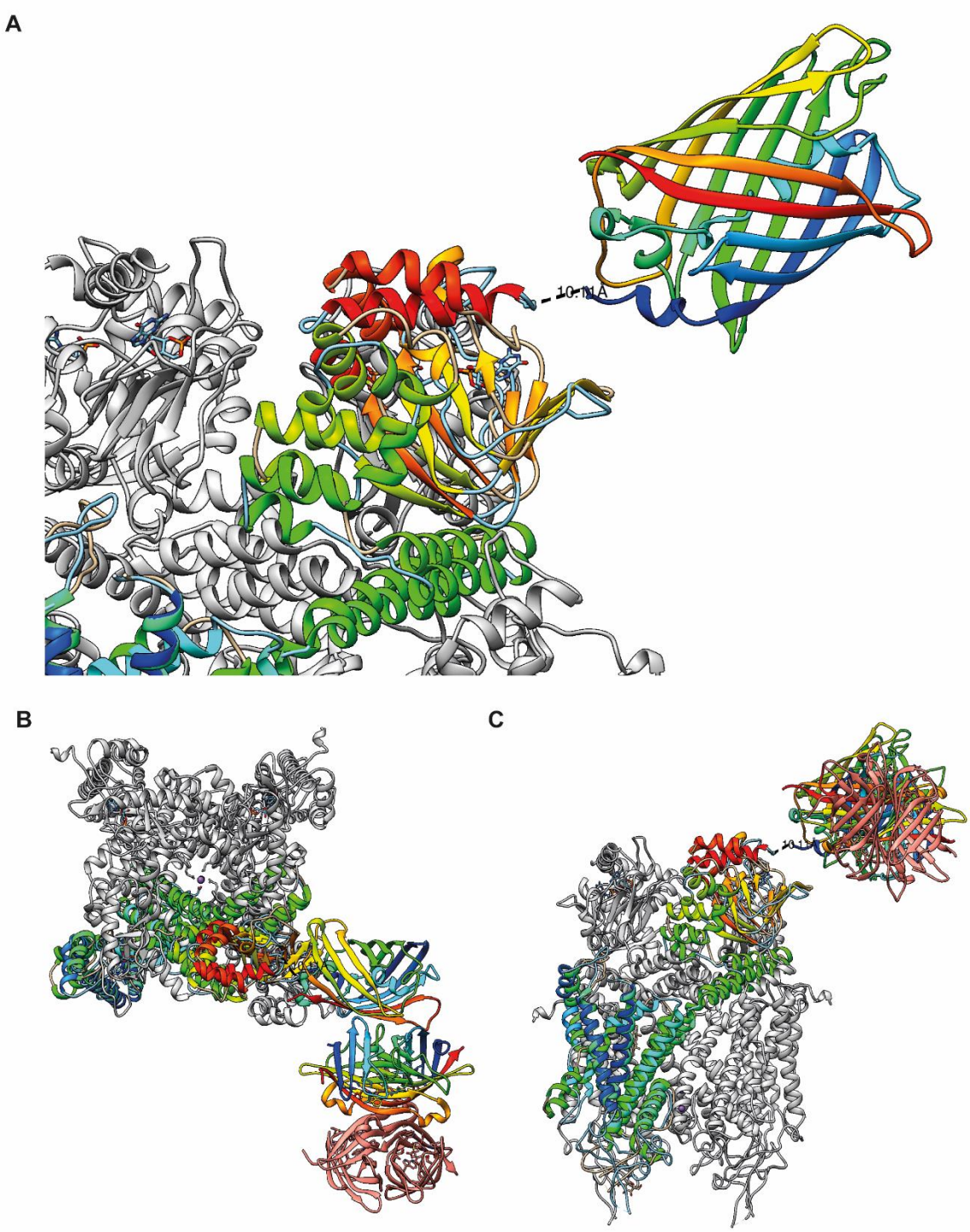

Figure 3.4 Determination of likely linker length.

(A) Minimal linker length of 10 Å is required between HCN1-C to N-GFP to prevent bumping of GFP onto CNBD of HCN1. (B-C) A longer HCN1-GFP linker is required to prevent steric clashes between GFP and streptavidin. GFP structure: PDB 1GFL. Figure by Prof. Dr. Elmar Behrmann.

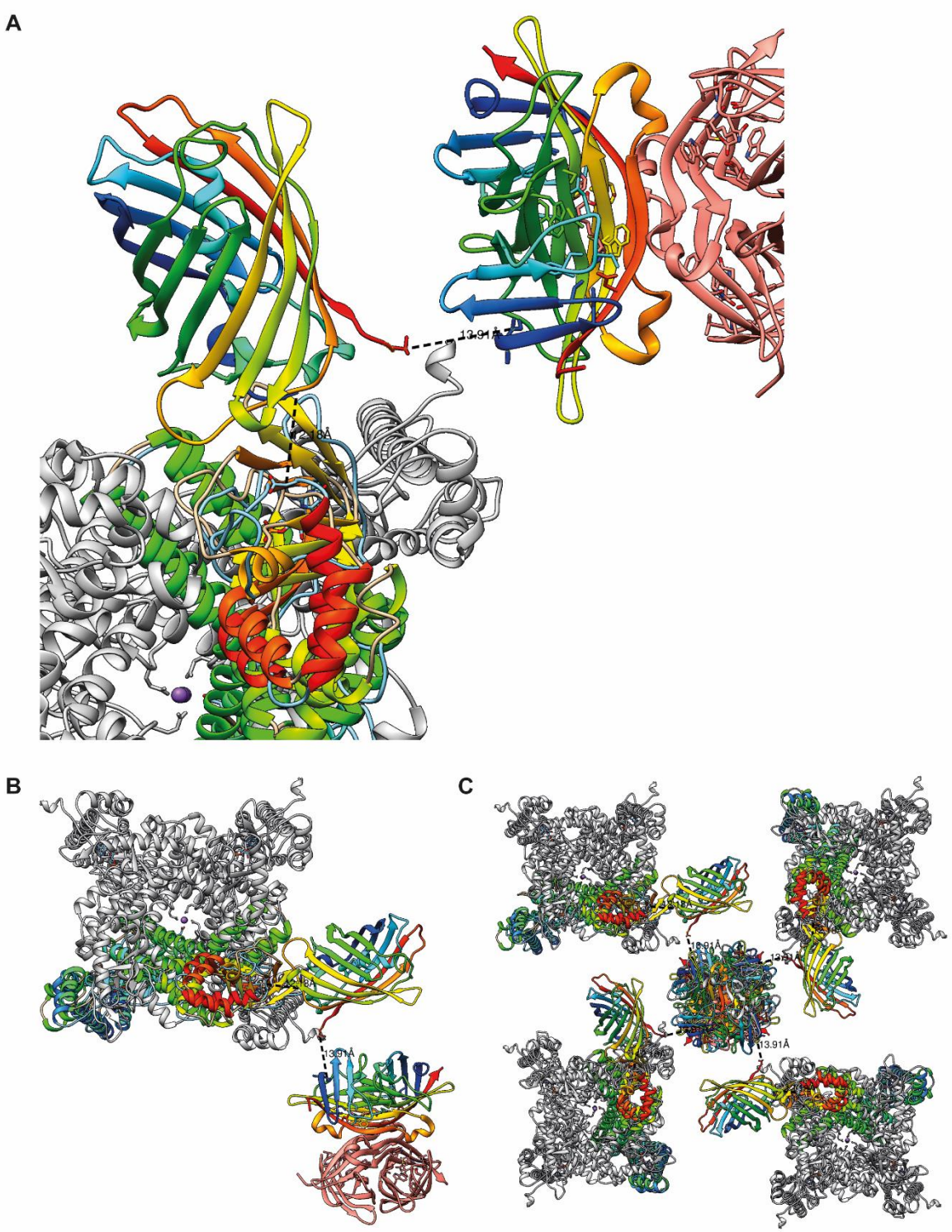

Figure 3.5 Optimal arrangement of the HCN1 lattice structure.

(A) GFP-C to N-streptavidin distance is extended to ~14 Å to prevent steric clashes between GFP and streptavidin. (B-C) An optimal lattice arrangement is shown. Figure by Prof. Dr. Elmar Behrmann.

3.1.2. Generating split GFP with enhanced folding robustness

The general strategy of split GFP is to fuse each half of the split reporter proteins to two test proteins that are expected to bind to each other. Interactions between the test proteins lead to the complementation of the reporter system, which can be utilized to investigate protein-protein interactions. In this study, we attached GFP_N to the N-terminus of *Ssp*Int_N and GFP_C to the C-terminus of *Ssp*Int_C (**Figure 3.6 A**). Besides, both constructs were respectively fluorescent-tagged with mCherry and mTagBFP2, resulting the constructs of mCherry::T2A::GFP_N::Int_N and mTagBFP2::T2A::Int_C::GFP_C. Successful protein trans-splicing led to the reconstituted functional GFP, which could be detected as an indicator of the protein lattice formation.

The reconstitution efficiency of the split GFP system, including the split sfGFP and split EGFP, was assessed in HEK293 cells. For the two variants of split GFP tested, EGFP was divided between the 7^{th} and 8^{th} β-strand, while sfGFP was split at the 11^{th} β-strand, yielding a 214-residue N-terminal fragment (GFP1-10) and a 17-residue C-terminal fragment GFP11. Strong GFP fluorescence was observed for both split sfGFP-*Ssp*Int and split EGFP-*Ssp*Int pairs when reconstituted in HEK293 cells (**Figure 3.6, B-C**). The time required for the formation of GFP after transient co-expression was about 4-6 h.

For the comparison of the relative reconstitution efficiency between these split pairs, it is essential to correct for the difference in the transfection efficiency and protein expression levels in individual cells; therefore, both the fluorescence intensities derived from GFP complementation and mCherry (as an internal control) were measured. The ratio of reconstituted GFP fluorescence over mCherry fluorescence was taken as the indicator of the split GFP complementation efficiency. Our results showed that split sfGFP possessed a significantly stronger fluorescence intensity than split EGFP upon split intein interactions (**Figure 3.6 D**).

To exclude the possibility that T2A peptide might interfere with protein trans-splicing, we attached T2A to the C-terminus of GFPc, generating the construct of *Ssp*Intc::GFPc::T2A::mTagBFP2. Both N- and C-parts of split intein were co-transfected in HEK293 cells and reconstituted GFP intensity was evaluated on fluorescence microscope 24 h post-transfection. Strong reconstituted GFP fluorescence was observed (**Figure 3.6 E**), indicating that T2A peptide does not interfere with the trans-splicing

process. As a fundamental part of this process, the trans-splicing efficiency of split intein is of critical importance. As a next step, we optimized the trans-splicing efficiency with *Ssp* DnaE and *Npu* DnaE inteins.

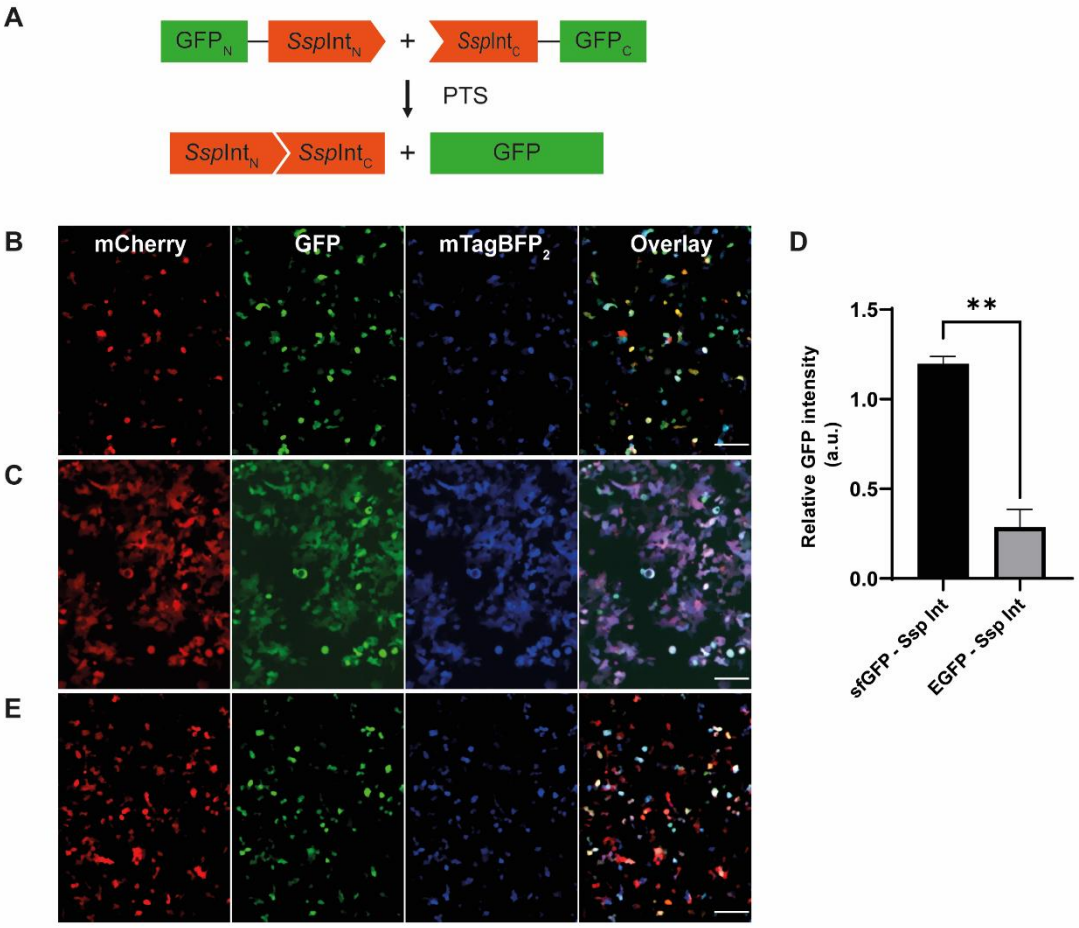

Figure 3.6 Split GFP reconstitution in HEK293 cells.

(A) Illustration of split intein trans-splicing process. (B-C) Confocal microscope images of HEK293 cells transiently transfected with mCherry::T2A::GFP$_N$::*Ssp*Int$_N$ (red) and mTagBFP2::T2A::*Ssp*Int$_C$::GFP$_C$ (blue). The reconstitution of split GFP constructs resulted in GFP fluorescence (green). In (B), the reconstitution of sfGFP$_N$-*Ssp*Int$_N$ and *Ssp*Int$_C$-sfGFP$_C$ is shown; in (C), the reconstitution of EGFP$_N$-*Ssp*Int$_N$ and *Ssp*Int$_C$-EGFP$_C$ is shown. (D) The quantification of relative GFP intensity showed split sfGFP had a higher reconstitution efficiency. (E) Same as (B) but with C-terminally tagged mTagBFP2. Scale bars: 100 µm.

3.1.3. Optimization of trans-splicing efficiency

In this study, the protein trans-splicing efficiency of the two most commonly used naturally-occurring inteins, *Npu* DnaE and *Ssp* DnaE was tested. Sequence alignment

showed that both inteins were homologous with similar sequences, with relatively long N-fragment (123-aa *Ssp* DnaE$_N$ and 102-aa *Npu* DnaE$_N$) and a short C-fragment (36 aa) (**Figure 3.7 A**). Besides the intrinsic splicing kinetics, extein residues near the junction site play a unique role in the protein trans-splicing efficiency (Evans et al., 2000). One possible assumption is that N- and C-extein sequences near the splicing junction site are likely to be involved in the active structural rearrangement of intein during protein splicing. For *Ssp* DnaE intein, the first C-extein residue (Cys+1) has been proved to be important as its side-chain thiol groups serve a nucleophile during protein splicing (Nichols and Evans, 2004). Also, amino acid substitution at the position of Phe+2 abolished the trans-splicing activity of *Ssp* DnaE entirely. Therefore, the trans-splicing efficiency of *Npu* DnaE with the three essential amino acids of C-extein (Cys-Phe-Asn) was tested (as illustrated in **Figure 3.7 B**). The results showed that trans-splicing with the *Npu* DnaE exhibited more robust trans-splicing efficiency than *Ssp* DnaE (**Figure 3.7 C**).

Interestingly, we also found out that the N-terminal part of *Npu* DnaE likely played a more dominant role in trans-splicing interaction, as the replacement of N-fragment but not the C-fragment significantly influenced trans-splicing efficiency (**Figure 3.7 D**). Additionally, cross-splicing activities in all combinations of *Npu* DnaE and *Ssp* DnaE were observed, except in the case of *Ssp* DnaE$_N$ in conjunction with *Npu* DnaE$_C$, indicating that interaction between *Npu* DnaE$_N$ and *Npu* DnaE$_C$ is less specific compared to its *Ssp* DnaE counterpart. Sequence alignment between *Npu* DnaE$_N$ and *Ssp* DnaE$_N$ showed *Npu* DnaE$_N$ was 21 amino acids shorter than *Ssp* DnaE$_N$. Considering this, we speculate that the flexibility of shorter N-fragment might contribute to the higher tolerance of varying DnaE$_C$ in *Npu* DnaE mediated trans-splicing reaction, as evidenced by random substitution studies (Cheriyan et al., 2013).

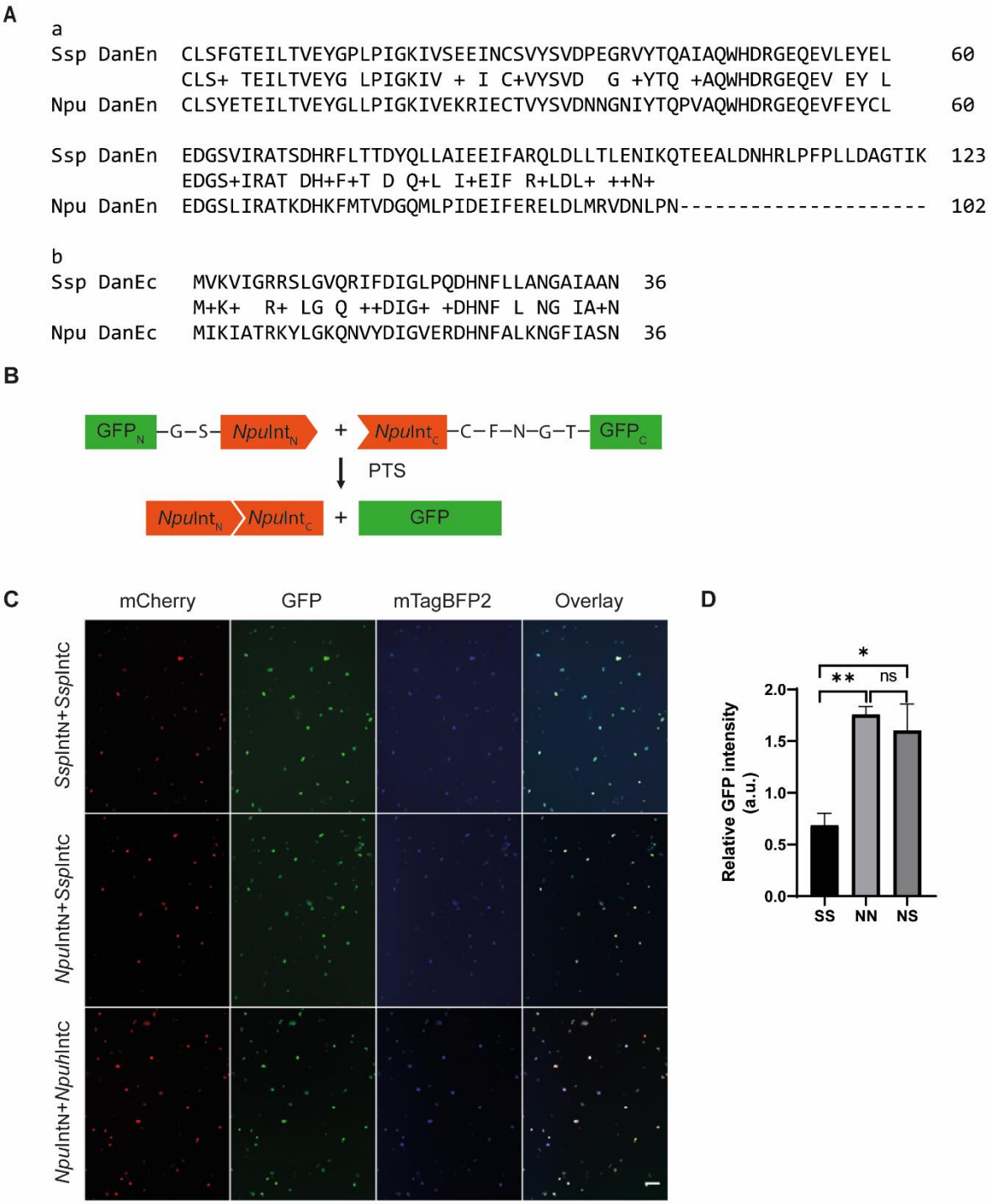

Figure 3.7 Optimized trans-splicing with *Npu* DnaE.

(A) Sequence alignment between *Ssp* DnaE and *Npu* DnaE. a) sequence alignment of *Npu* DnaE$_N$ and *Ssp* DanE$_N$; b) sequence alignment of *Npu* DnaEc and *Ssp* DnaEc. (B) Schematic illustration of the trans-splicing process, the boundary sequence GS and CFNGT are shown in one-letter code for amino acids. (C) Fluorescence imaging of cross-splicing of *Ssp* DnaE and *Npu* DnaE. Int$_N$ (red) and Int$_C$ (blue) constructs were transiently co-transfected in HEK293 cells. The resulting reconstituted GFP (green)

intensity was used for the quantification of trans-splicing efficiency in (D). Scale bar: 100 µm.

3.1.4. Expression optimization of HCN1 on the membrane

3.1.4.1. **Optimizing cultivation time for transient expression**

Membrane protein expression by transient transfection was efficient and fast, yet inhomogeneous membrane expression, even cytoplasmic aggregation, was occasionally observed. Multiple factors could affect the expression paradigm of membrane proteins, including the amount of plasmid used per transfection, promoter strength, transfection efficiency, and cultivation time.

To determine the optimal cultivation time for HCN1 transient expression, we examined the subcellular localization of GFP by confocal microscopy after co-transfecting HEK293 cells with plasmids encoding mCherry::T2A::HCN1$_{\triangle N \triangle C}$::GFP$_N$::Int$_N$ and mTagBBFP2::T2A::Int$_C$::GFP$_C$::streptavidin. Nuclear localization of GFP fluorescence was identified 48 h post-transfection, but not 24 h post-transfection (**Figure 3.8, A-B**), indicating that a longer cultivation time leads to increased GFP import into the nucleus. To exclude the possibility of fluorescence location in the nucleus above or below the optical plane, we performed a series of vertical sections of a single cell. The Z-stack scanning showed no detectable GFP signal 24 h post-transfection on every optical section plane, but positive GFP signal throughout all the optical section planes 48 h post-transfection, indicating an accurate nuclear localization (**Figure 3.8, C-D**).

3.1.4.2. **N-terminal ER-exit motif facilitates membrane trafficking**

Membrane trafficking is of essential importance to the normal function of ion channels. In eukaryotes, transport vesicles move proteins from one intracellular compartment to another continuously and dynamically. Experimental evidence suggests that the export of membrane protein from the ER to the Golgi complex is a rather selective process (Balch et al., 1994), which may be accomplished by the interaction of the ER export motif with specific components of coat-protein complexes (COP)-II coated vesicles. ER export motif functions by recruiting the COPII complex into nascent buds and deforming the ER membrane to drive vesicle formation to bud off from the ER to the Golgi

apparatus (D'Arcangelo et al., 2013). To date, several classes of ER export motifs have been identified in the cytoplasmic terminals of transmembrane proteins (Hanton et al., 2005; Nufer et al., 2002; Spear et al., 2015).

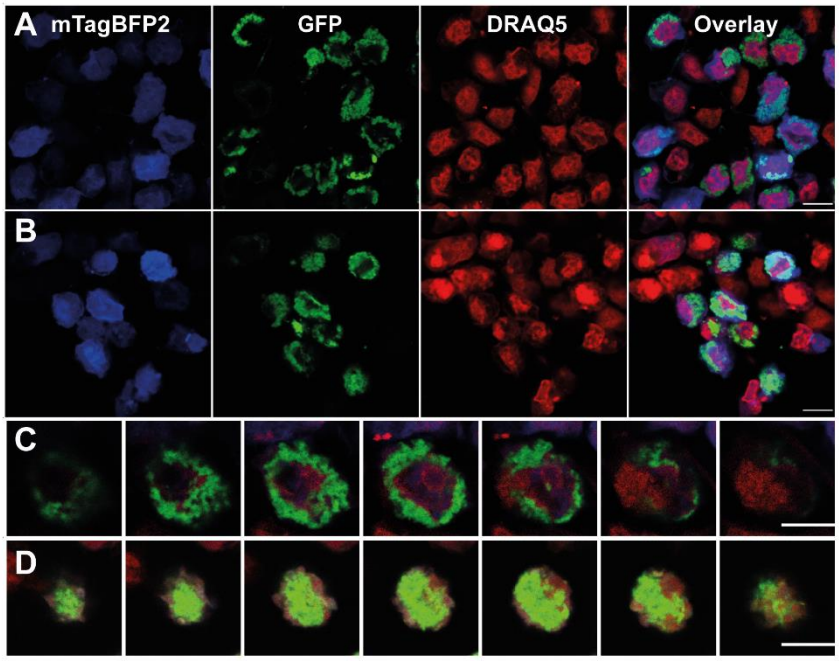

Figure 3.8 Expression of GFP-tagged HCN1 in HEK293 cells.

HEK293 cells were co-transfected with plasmids encoding mCherry::T2A::HCN1$_{\triangle N \triangle C}$::GFP$_N$::Int$_N$ and mTagBBFP2::T2A::Int$_C$::GFP$_C$::streptavidin. Cells were then fixed, stained with DRAQ5, and imaged after a cultivation period of 24 h (A) and 48 h (B). mTagBFP2, GFP, and DRAQ5 fluorescence and merged images were shown. Z-stack confocal imaging revealed negative and positive nuclear localization of GFP 24 h (C) and 48 h (D) post-transfection. Scale bars: 10 µm.

ClustalW sequence alignment of the human HCN1 channel to HCN1 channels from various animal species showed a conserved ER-export motif (VxxxSL) in the N-terminus near the first transmembrane segment (Pan et al., 2015) (**Figure 3.9 A**). To explore the role of N-terminus in the trafficking of HCN1 channels, we fused the N-terminus to the truncated HCN1 channels (HCN1$_{\triangle N \triangle C}$), generating the construct of HCN1$_{\triangle C}$. This construct was then transiently expressed in HEK293 cells, and their subcellular localization was determined using the confocal microscope. The results showed reduced membrane expression of truncated HCN1 in both transient and stable expression (**Figure 3.9, C-D**), implying a possible defect in membrane trafficking. By fusing the N-terminus to

the truncated HCN1 channel, membrane trafficking was significantly improved (**Figure 3.9, E-F**). These results indicated that HCN1 N-terminus containing the ER export motif is critical for membrane trafficking.

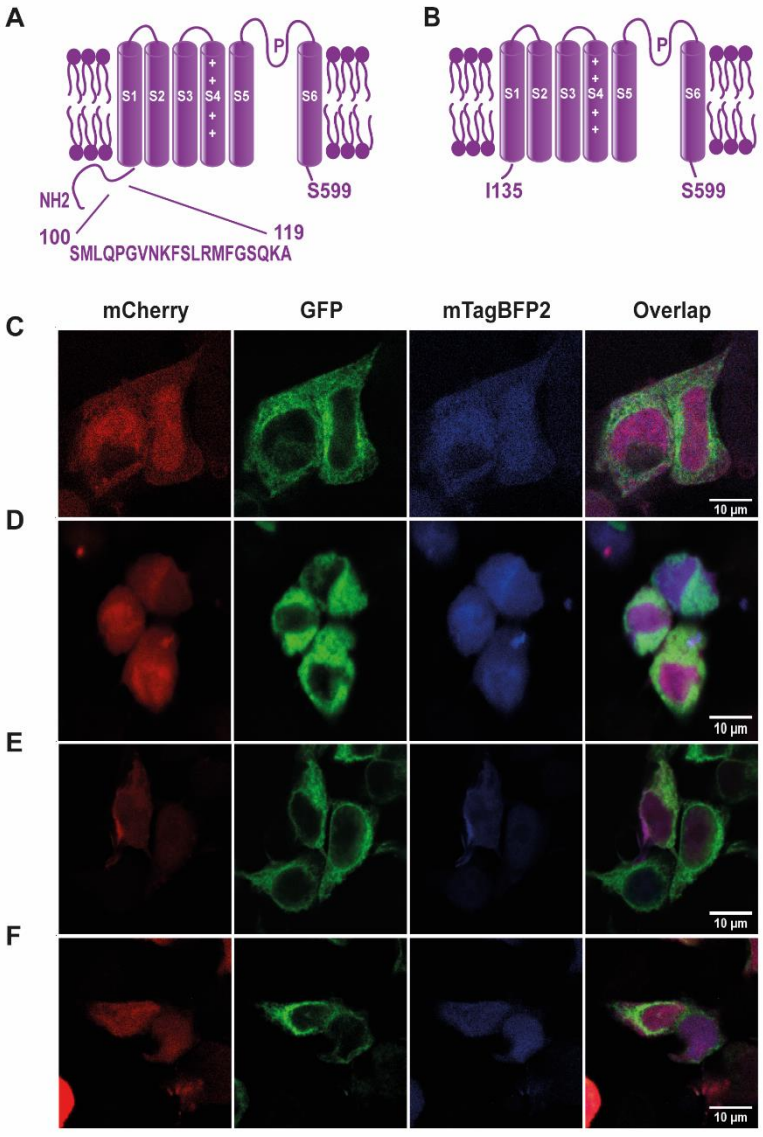

Figure 3.9 N-terminal is required for sufficient membrane trafficking of HCN1.

(A-B) Schematic illustration representing one domain of $HCN_{\triangle N \triangle C}$ and $HCN_{\triangle C}$. $HCN_{\triangle N \triangle C}$ truncated at both N-terminus (I135) and C-terminus (S599); $HCN_{\triangle C}$ truncated at C-terminus (S599). (C-D) Confocal imaging of $HCN_{\triangle N \triangle C}$ channels stably (C) or transiently (D) expressed showed both membrane and cytoplasmic expression. (E-F) Confocal imaging of $HCN_{\triangle C}$ channels stably (E) or transiently (F) expressed showed significantly improved membrane expression.

We also determined whether the addition of the ER-export motif to the C-terminus of the HCN1 lattice linker component would affect membrane trafficking. Therefore, we fused ER-exit signal peptide (FCYENEV) on the C-terminus of Int_C::GFP_C::streptavidin (**Figure 3.10 A**). Interestingly, however, confocal imaging showed GFP aggregates in the cytoplasm (**Figure 3.10 B**), indicating that adding the ER-exit signal to the C-terminus of the HCN1 lattice linker component is not sufficient to promote the ER-exit of the HCN1 channel. One possible assumption is that ER-exit motifs only function correctly with channel-specific sequence and correct position in the expressed protein complex. Mechanistic elucidation of COPII recruitment would be beneficial in further delineating the anterograde trafficking pathway of HCN1 channels.

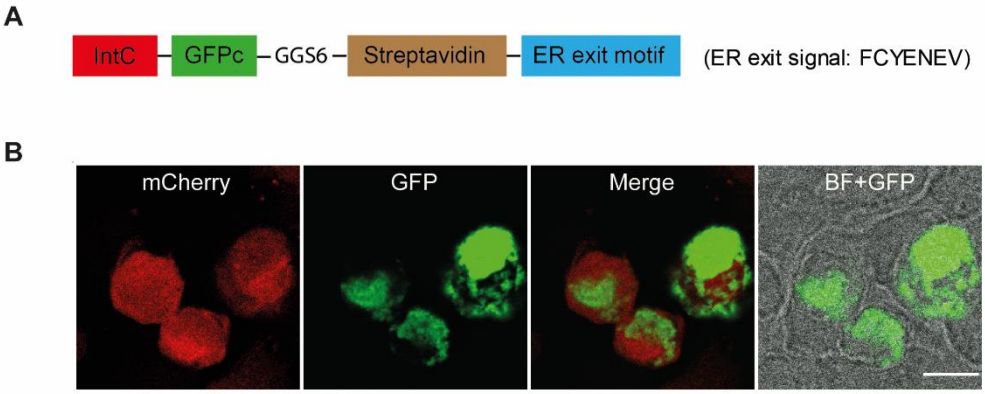

Figure 3.10 Subcellular localization of HCN1 after fusing ER-exit to the C-terminus.

(A) A schematic diagram of the expressed protein is shown. An ER-exit motif is linked to the C-terminus of Int_C::GFP_C::streptavidin. (B) Confocal imaging showed GFP aggregation in the cytoplasm. Scale bar: 10 µm.

3.2. Electrophysiological recording

3.2.1. Electrophysiological recording in a transient system

To compare channel densities of clustered and non-clustered HCN1 channels on the membrane, we co-transfected HEK293 cells with plasmids encoding mCherry::T2A::HCN1::GFP_N::Int_N and mTagBFP2::T2A::Int_C::GFP_C::streptavidin. HEK293 cells transfected with plasmid encoding mCherry::T2A::HCN1::GFP_N::Int_N or full-length HCN1 were recorded as control. **Figure 3.11 A-B** shows examples of typical whole-

cell HCN1 currents recorded with the protocol displayed. For the assessment of the channel density expressed on the membrane, cell capacitance of each cell was recorded, which is directly proportional to its cell membrane surface area (Hille,1984); the amplitude of I_h, on the other hand, relates to the total number of functional HCN1 channels on the membrane. Therefore, functional HCN1 channel density (the number of functional HCN1 channels per unit of cell surface area) can be best estimated by electrophysiological measurements of HCN1 channel current density.

Our results showed HCN1 channel density was considerably higher in HEK293 cells transfected with cluster constructs than non-cluster constructs or full-length HCN1 channel at a voltage from -140 mV to -110 mV (**Figure 3.11 C**, two-way AVONA, $p<0.0001$). All these three groups exhibited hyperpolarization-dependent activation. Besides, there was a depolarizing shift in voltage-dependent activation of the $HCN1_{\triangle C}$ cluster and $HCN1_{\triangle C}$ non-cluster groups compared to full-length HCN control (**Figure 3.11, D-E**, one-way ANOVA, $p=0.0021$ and $p=0.0098$, respectively). For the reversal potential, there was no significant difference (**Figure 3.11 F**).

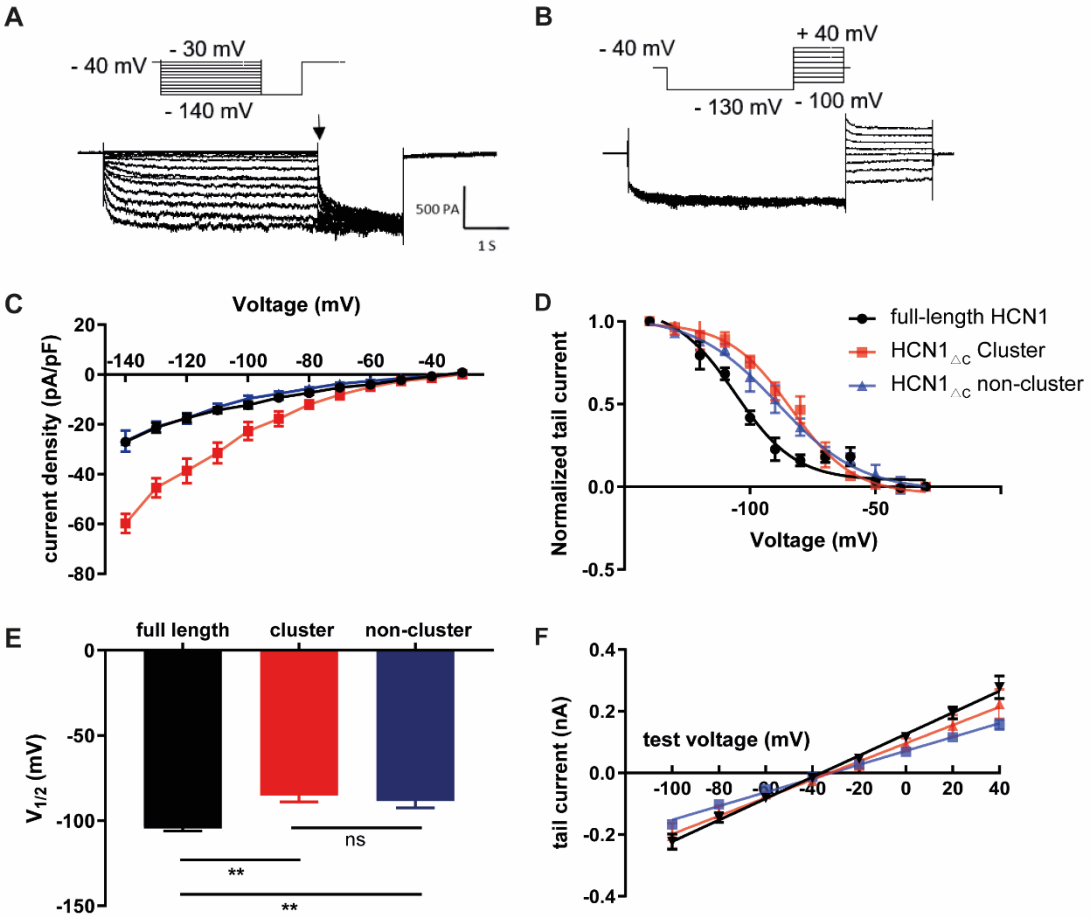

Figure 3.11 Electrophysiological recording of HCN1 expressed in HEK293 cells.

(A) Representative HCN1 current traces elicited by the pulse protocol displayed above. Cells were held at -40 mV, and hyperpolarized at potentials from -140 mV to -30 mV for 5 s, followed by a pulse to -140 mV for 2 s. Currents immediately following the pulse to -140 mV after the initial activations at various potentials (arrow) were defined as tail currents, and were used to determine the voltage-dependent activation kinetics. (B) Upper panel, pulse protocol for the determination of reversal potential E_{rev}. Lower panel, representative recording of HCN1 current traces. The tail current amplitudes immediately after the step to test voltages between -100 mV and +40 mV were used to determine E_{rev}. (C) Current density curves for full-length HCN1, HCN1$_{\triangle C}$ cluster, and HCN1$_{\triangle C}$ non-cluster groups. (D) Normalized voltage-dependent activation curves showed a depolarizing shift in voltage-dependence activation of the HCN1$_{\triangle C}$ cluster and HCN1$_{\triangle C}$ non-cluster groups compared to full-length HCN1 control. (E) Half maximal activation voltage ($V_{1/2}$) of HCN1$_{\triangle C}$ cluster and HCN1$_{\triangle C}$ non-cluster groups, derived from voltage-dependent activation curves were significantly different from full-length HCN1 control (one-way ANOVA, p=0.0021 and p=0.0098, respectively). (F) Tail current/voltage relations revealed E_{rev} at ~36 mV for all three groups (full-length HCN1, HCN1$_{\triangle C}$ cluster, and HCN1$_{\triangle C}$ non-cluster). All values were given as the mean ± SEM; n= 6-8 cells per experiment.

3.2.2. Electrophysiological recording in a stable system

Transient expression of HCN1 channel often leads to variable levels of protein expression in HEK293 cells. Thus, we established the HEK293-A6 cell line that stably expressed HCN1 lattice by undirected integration of the mCherry::T2A::HCN1::GFP_N::Int_N and mTagBFP2::T2A::Int_C::GFP_C::streptavidin constructs into the genome of the host cell. The electrophysiological recording showed stable cell line A6 had a current amplitude of 1.12 nA at -140 mV, which corresponded to a current density of 59.61 pA/pF. $V_{1/2}$ is -109.7 mV, and E_{rev} is -39.48 mV (**Figure 3.12**).

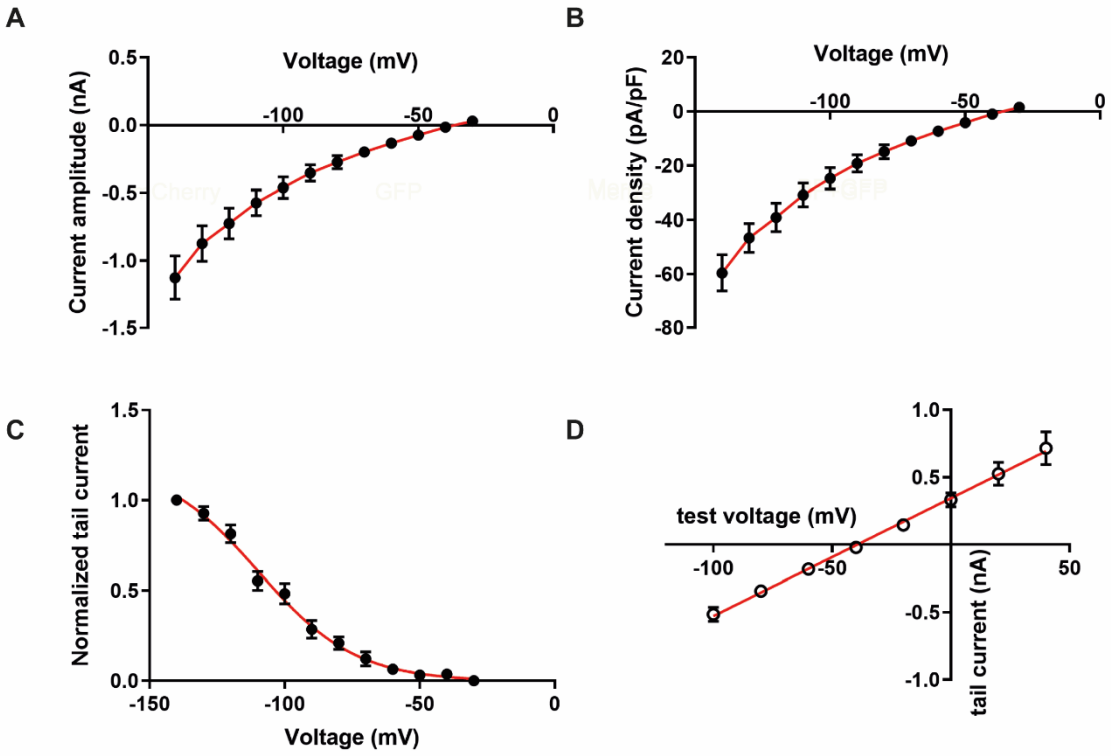

Figure 3.12 Electrophysiological recording of HCN1 expressed in the cell line.

The current-voltage curve (A) and current density-voltage curve (B) of HCN1 stably expressed in HEK293 cells. (C) Voltage-dependent activation curve of HCN1 in the stable cell line; the normalized tail current is plotted against activation voltage and fitted with Boltzmann function to obtain the half-maximal activation voltage ($V_{1/2}$). (D) Tail current is plotted against the holding voltage to show the E_{rev} of HCN1 expressed in the cell line. All values were given as the mean ± SEM; n= 7-8 cells per experiment.

3.3. Generation of the membrane sheet

3.3.1. Membrane sheet preparation

An inherent limitation in TEM techniques is the sample thickness, which needs to be < 300 nm (Adrian et al., 1984). Given this limitation, many eukaryotic cells are too thick to be imagined by EM, there is, therefore, a need to reduce the sample thickness by methods including vitreous sectioning and cryo-FIB milling. In this study, we applied unroofing techniques to derive membrane sheets directly from cells stably express HCN1 lattice. Compared to isolated proteins or protein in reconstituted bilayers, membrane sheets offer the advantages of providing a near-native lipid membrane environment for protein structural studies. In this study, both sonication and paper blotting methods (**Figure 3.13, A-B)** were optimized to achieve efficient unroofing while maximally preserve the completeness of carbon film.

3.3.1.1. **Membrane sheet preparation by sonication**

Sonication intensity from 5% to 25% of maximal output, in combination with sonication duration from 0.1 s to 1 s, were tested for efficient membrane sheet production. We found sonication intensity lower than 15% failed to generate membrane sheets efficiently, while sonication intensity higher than 25% severely damaged EM grid carbon film (**Figure 3.13, C-F**). Besides, sonication duration was an additional key factor: sonication duration of 0.5 s was optimal for membrane sheeting, and sonication for a longer duration did not further increase membrane sheet yield. We also tested membrane sheet production with various tip distances to the cell side of the EM grid ranging from 0.1 cm to 1 cm. Screening results showed that a slight change in tip distance significantly influenced the membrane sheeting success rate. Tip distances lower than 0.5 cm could severely damage the carbon film, while tip distances higher than 1 cm produced too weak sonication power to rip the cells open. Therefore, a tip distance of 0.7-1 cm was applied as an optimal condition for sonication. After systematic screening experiments, we determined that the optimal combination of parameters for membrane sheeting was a sonication intensity of 15-20% of maximal output, with a sonication duration of 0.5 s and a tip distance of 0.7-1 cm. In some cases, a second episode of sonication was necessary to improve membrane sheet production.

3.3.1.2. **Membrane sheet preparation by paper blotting**

The crucial part of paper blotting is the choice of filter papers, which is influenced by several factors, including cell health, confluence, and attachment to the EM grid. Six types of filter papers were screened on HEK293 cells, with physical properties, as provided by the manufacturers, listed as follows (**Table 3.1**). The blotting cycles and blotting time were optimized. Fluorescent labeling and negative-staining EM were used to assess the membrane patch yield and quality (**Figure 3.13, G-K**).

As indicated by systematic screening results, blotting twice from the cell side with Whatman® qualitative filter paper Grade 41 for 2-3 s turned out to be the most efficient condition. A second investigator repeated each blotting protocol using different filter papers. Although there was a minor difference in patch production efficiency, the observations in the first trial could be well reproduced in the second trial by the second investigator. Whatman® qualitative filter paper Grade 41 was producing membrane patches with high reproducibility in the hands of both investigators and was therefore chosen for the routine procedures of paper blotting. Compared to the sonication method, the paper-blotting method produced membrane patches with smaller surface coverage and less consistency in the membrane patch thickness (**Figure 3.13 L**). Therefore, validation of the generated membrane patch is required before EM imaging.

Table 3.1 Filter paper screening for optimal conditions on HEK293 cells

Whatman® Qualitative filter paper	Grammage (g/m^2)	Thickness (µm)	Blotting 1^{st} trial	Blotting 2^{nd} trial
Grade 1	87	180	+	-
Grade 4	92	205	-	++
Grade 41	95	210	++	+
Grade 42	95	220	+	-
Grade 43	100	200	-	--
Grade 50	97	0.12115	--	--

- no membrane patches
-- severely damaged carbon film
+ membrane patches present (<40%)
++ membrane patches present (>40%)
+++ membrane patches (>40%) + very good sample preservation

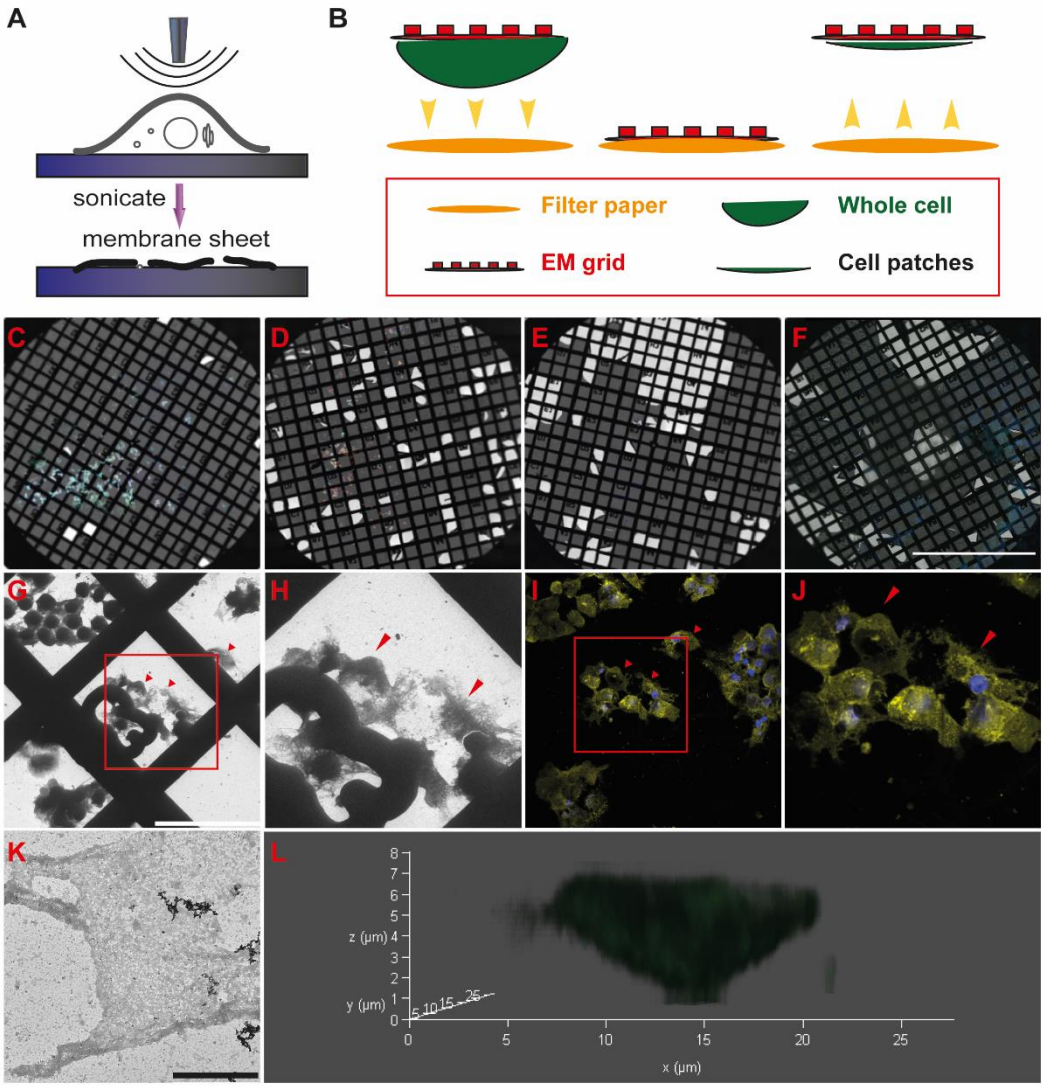

Figure 3.13 Membrane sheet generation in HEK293 cells.

(A-B) Schematic illustration of unroofing by sonication and paper-blotting methods. (C-F) Grid overview after sonication with 15% intensity for 0.1 s (C), 20% intensity for 0.1 s (D), 20% intensity for 0.5 s (E), 25% intensity for 0.1 s (F). Scale bar: 1 mm. (G-J) Isolated membrane patches from HEK293 cells. (G) Overview of HEK293 membrane patches on the grid after negative staining (arrows). Scale bar: 100 µm. (H) Zoom-in image of the marked rectangular area in (G). (I) Isolated membrane patches showed positive membrane stain (yellow) and negative nucleus stain (blue). (J) Zoom-in image of the marked rectangular area in (I). (K) Magnified view showing a single membrane patch from WT HEK293 cells by sonication. Scale bar: 2 µm. (L) 3D reconstruction of a membrane preparation generated by the paper-blotting method showed a thickness of around 7 µm.

3.3.2. Membrane sheet validation

3.3.2.1. **Membrane sheet validation in WT HEK293 cell**

WT HEK293 cells were labeled with CellMask plasma membrane stain, Mitotracker Orange CMTMRos, and DRAQ5 nucleus stain, as described above. After unroofing procedures, membrane preparations with positive DRAQ5 stain were verified as whole cells or unsuccessful membrane sheeting (**Figure 3.14 A**), while samples with positive CellMask plasma membrane stain and negative DRAQ5 labels were validated as qualified membrane patches (**Figure 3.14, B-D**). Typical membrane patches had an area up to a few hundred square micrometers. When the sonication intensity was too strong, membranes could be even fragmented. Z-stack confocal imaging of the membrane patches (**Figure 3.14, E-F**) showed a negative nucleus stain in each confocal plane. X-Z section of 3D reconstruction images showed that the generated membrane sheet was significantly thinner than the whole cell.

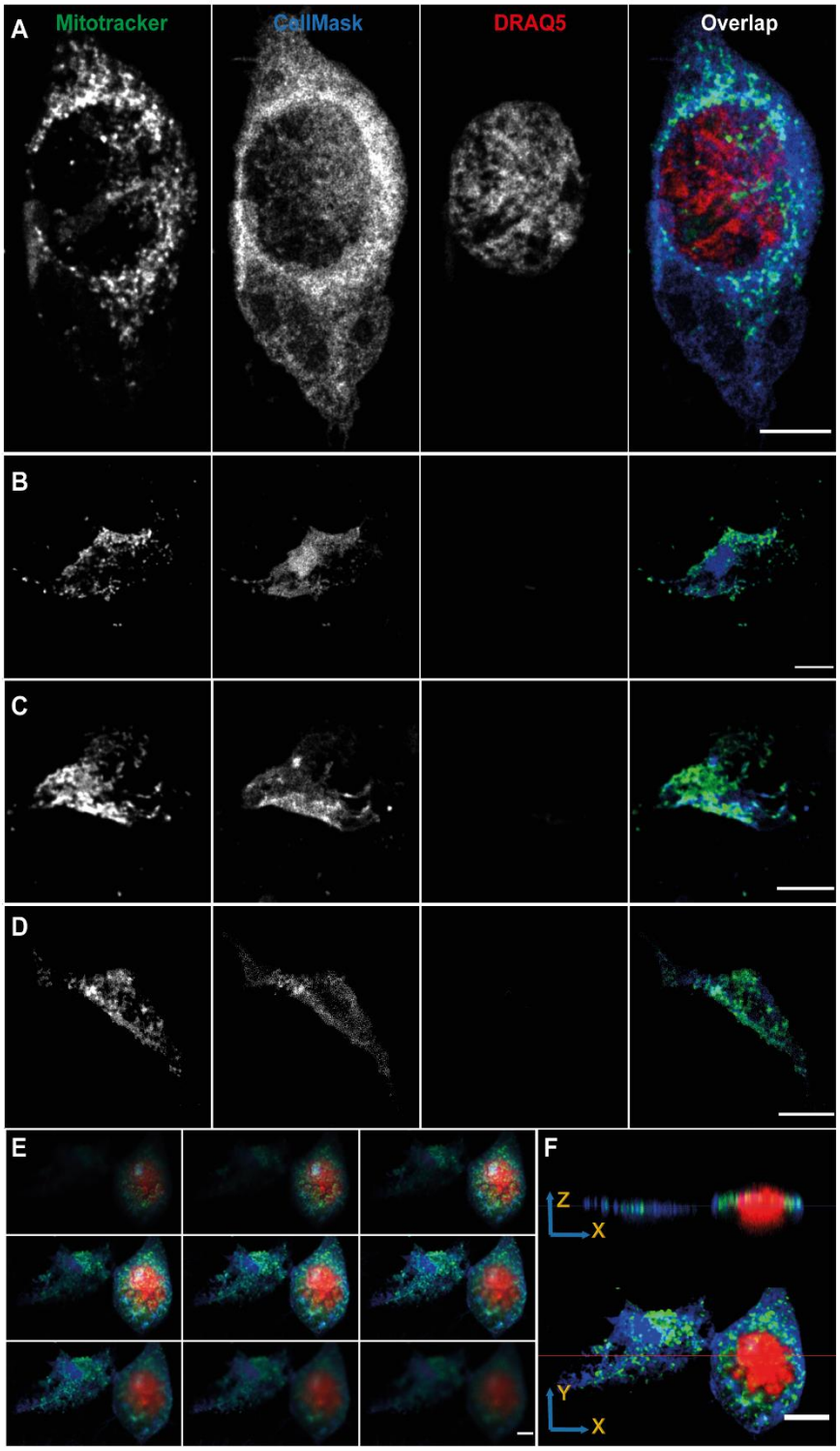

Figure 3.14 Membrane sheet generation in WT HEK293 cells.

(A) Presentative confocal imaging of complete WT HEK293 cells. (B-D) Presentative imaging of cell membrane patches generated from WT HEK293 cells. Cells were labeled with Mitotracker (green), CellMask plasma membrane stain (blue), and DRAQ5 (red). (E) 2D Z-stack confocal images of membrane sheet (left) and whole-cell (right) stained with CellMask plasma membrane dye (blue), Mitotracker (green), and DRAQ5 (red). (F) Cross-sections of 3D reconstruction images of membrane sheet (left) and whole-cell (right) were shown. The X-Z section was made at the red line in the X-Y section image. Scale bars: 10 µm.

3.3.2.2. **Membrane sheet validation in the HCN1 lattice system**

HEK293 HCN1-A6 cells were labeled with CellMask plasma membrane stain and Hoechst 34580 nuclear stain, as described previously. Generated membrane sheets were examined under the fluorescence microscope. Cells with only positive CellMask plasma membrane stain were qualified as membrane sheets, while cells with positive Hoechst 34580 nuclear stain were considered as whole cells (**Figure 3.15**). The results indicate that membrane sheeting procedures optimized in WT HEK293 cells are readily transferrable to the HEK293 HCN1-A6 cell line.

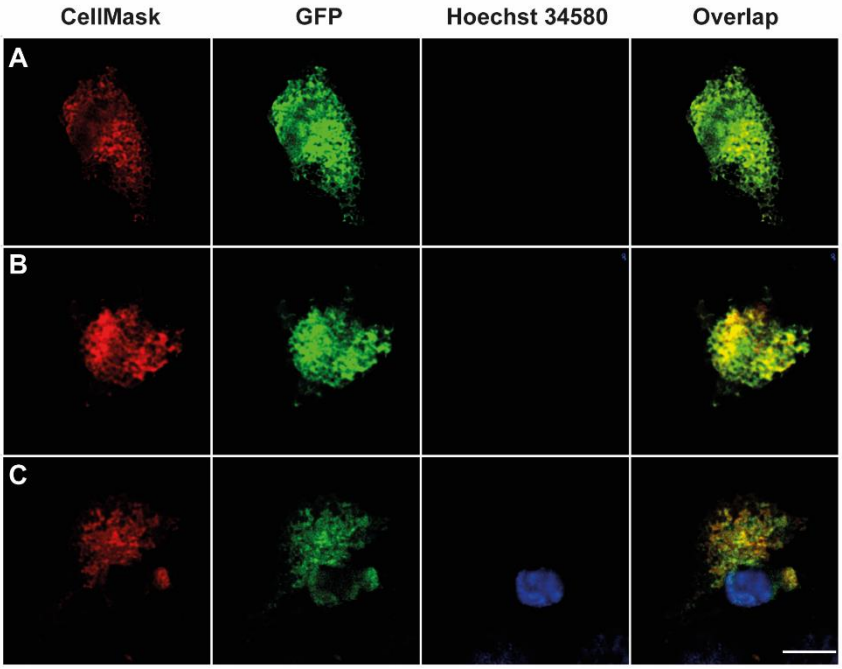

Figure 3.15 Confocal images of membrane sheet expressing HCN1 lattice.

(A-C) Representative confocal imaging of membrane patches expressing HCN1 lattice (green) validated as positive CellMask plasma membrane stain (red) and negative Hoechst 34580 stain (blue). Scale bar: 10 µm.

3.4. Correlative light and electron microscopy

3.4.1. Immunofluorescent labeling of HCN1 lattice with QDs

For the detection of protein lattice on the membrane, a high degree of specific labeling is required. The unique optical features and electron density of QDs make them desirable probes for correlative microscopic analysis. To achieve high labeling specificity without compromising biomolecular function, we synthesized specific immunofluorescent probes by conjugating QDs to GFP nanobodies (**Figure 3.16 A**). This resulting QD-GFP nanobody complex (QD-GFPnb) would then be able to bind GFP in the HCN1 lattice with high specificity. We investigated the labeling efficiency of QD-GFPnb probes at the subcellular level using the membrane sheets generated from HEK293 cells stably expressing HCN1 lattice. These membrane sheets were then labeled with QD-GFPnb probes, as well as nuclear and plasma membrane stain, and examined under the confocal microscopy (detailed in **Figure 3.16 B**). Three different blocking conditions (1% BSA, 6%

BSA/10% horse serum, and 10% horse serum) were tested to optimize QD labeling, Confocal images showed good colocalization of GFP and conjugated QDs in all three blocking conditions (**Figure 3.16, C-E**). When WT HKE293 cells were incubated with QD-GFPnb conjugates, no signal was detected (**Figure 3.16 F**). These results indicate the high specificity of QD-GFPnb conjugate labeling.

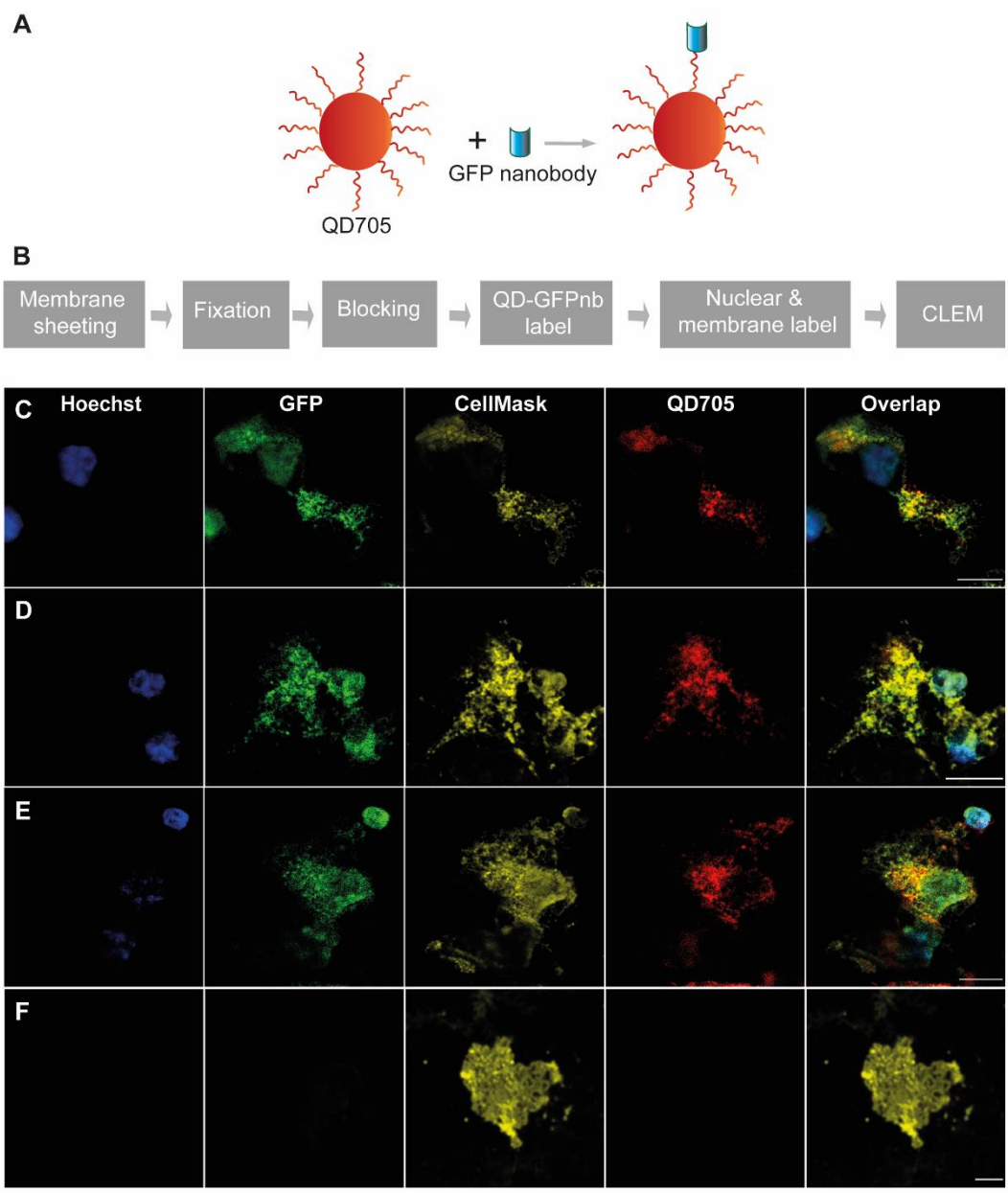

Figure 3.16 QD label of membrane sheet expressing HCN1 lattice.

(A) A schematic diagram showing GFPnb conjugated to QDs. (B) The general process of QD labeling of membrane sheets. (C-E) Membrane sheets generated from HEK293 cells expressing HCN1 lattice were fixed, blocked, and incubated with QD-GFPnb conjugates. Cells were blocked with (C) 1% BSA, (D) 6% BSA/10% horse serum, and (E) 10% horse serum. In all three blocking conditions, QD-GFPnb showed strong colocalization with GFP. (F) When WT HEK293 cells were incubated with QD-GFPnb conjugates, no detectable signals on the cell were identified. The nuclei were counterstained with Hoechst 34580 (blue), and the membrane was stained with CellMask plasma membrane stain (orange). Filter set cy5.5 (ex 654±20 nm/em 716±20 nm) was used for QD705 imaging. Scale bars: 10 µm.

3.4.2. CLEM

CLEM is a powerful method that allows the identification of targeted macromolecules within a high-resolution cellular map. It is covered by a wide range of techniques including protein fluorescent and QD labeling, fLM imaging, as well as TEM data collection and analysis for subsequent cryo-ET studies. For the CLEM of HCN1 lattice on the membrane, membrane patches with HCN1 lattice were identified and located in fLM (**Figure 3.17, A-C**), with their coordinates transferred to EM for the acquisition of high-resolution structural data. At the EM stage, a low-magnification (100-150×) map of the entire grid was acquired using SerialEM software (**Figure 3.17 D**). Subsequently, an intermediate-magnification montaging of ROIs identified in fLM was acquired (**Figure 3.17 E**). High-resolution TEM images revealed clusters of QDs, which correlated nicely with the GFP fluorescence on the membrane patch. These results strongly indicate the successful formation of protein lattice on the membrane (**Figure 3.17 F**).

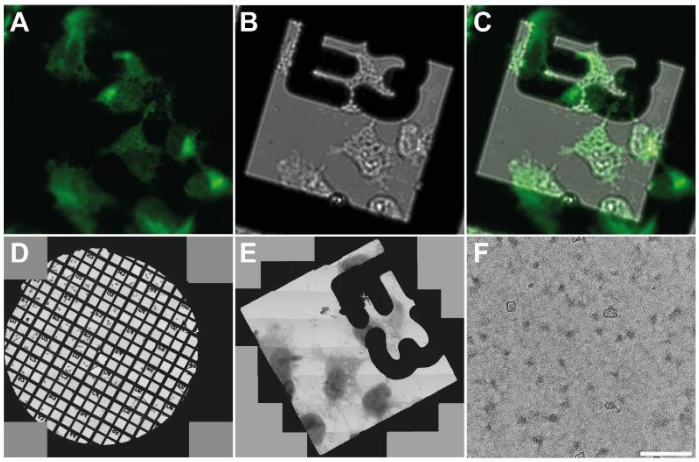

Figure 3.17 CLEM of HCN1 lattice on the membrane.

(A-C) Fluorescence microscopy image of HEK293 cells expressing HCN1 lattice on the grid using the Leica LASX software: (A) GFP, (B) bright-field, (C) merged images. (D) Grid map by negative-staining TEM. (E) TEM montage by SerialEM software. (F) 60,000× magnification TEM images showed clusters of QDs. Scale bar: 200 nm.

4. Discussion

4.1. Studying membrane protein in near-native environments

Membrane proteins perform vital roles in many biological processes and account for approximately 60% of the drug targets (Terstappen and Reggiani, 2001; Yildirim et al., 2007). Therefore, studying membrane proteins at atomic resolution is critical for extending our understanding of their structure-functional relationships and rational drug design with improved pharmaceutical properties (Blundell et al., 2002; Murray and Blundell, 2010; Stansfeld and Sansom, 2011). The past few years have seen explosive growth in SBDD due to technical development in structural biology. Nevertheless, structural determination of membrane protein has lagged behind compared to cytosolic ones, mainly due to the challenge in membrane protein expression and purification. As membrane proteins are inserted into the lipid bilayer with large gradients in fluidity, water concentration, and dielectric constants across the membrane (De Planque et al., 2001; Engelman, 1996), both the lipid composition and biophysical properties of the cell membrane are known to influence membrane protein structure, dynamics, and function. Although considerable technical advances have been made over the past years, the solubilization, purification, and reconstitution of membrane protein in mimetics of native membranes in a functional state remain the main ‘bottleneck’ for structural studies.

Detergents, with different hydrophobicity properties, have been the most commonly employed route to solubilize membrane proteins in expression systems. However, not all proteins are amenable to detergent isolation. Besides, the presence of detergents used in crystallography gives rise to structural distortions in membrane proteins because of the non-native environment. Therefore, a thorough detergent screen is often required to identify the detergent that can best stabilize the targeted membrane protein in a functional state. Recently amphipols and nanodiscs have become increasingly popular, as well as new technologies such as styrene-maleic acid copolymer lipid particles and saposin-lipoprotein nanoparticle systems (Bayburt and Sligar, 2010; Breyton et al., 2010; Frauenfeld et al., 2016; Postis et al., 2015; Tate, 2010). However, these micelle-like structure formations are significantly different from those of the lipid bilayer environment, leading to possible perturbance of the native structure, disruption of specific

conformational states, and elimination of critical native cofactors. Recent studies showed notable structural distortions for membrane proteins determined in detergents and detergent micelles (Cross et al., 2011; Zhou and Cross, 2013).

In membrane protein crystallography, protein engineerings, such as mutagenesis (Abdul-Hussein et al., 2013; Serrano-Vega and Tate, 2009), truncation (Lee and MacKinnon, 2017) and the creation of chimeras (Long et al., 2007; Nishida et al., 2007), are often carried out for facilitating crystallization. However, these modifications might cause the structure solved to differ from the fully functional native structure (Lu et al., 2013). For instance, while most point mutations resulted in subtle structural differences, some led to structural changes crucial for the mechanistic understanding of the protein function and rational drug design. The truncations of membrane protein, most often the N- and C-terminal segments, are considered as relatively benign alterations that leave the core structure and function of proteins intact. However, dramatic conformational rearrangements were observed in membrane protein after N-terminus truncation (Lu et al., 2013). Lastly, the inserted tag in crystallography could interfere with the ligand-binding or the protein-protein interaction sites. Similarly, the adding of an antibody or nanobody to facilitate the crystallization process might lock the structure in a conformational intermediate (Pardon et al., 2014; Steyaert and Kobilka, 2011).

Membrane patches obtained directly from biological cells offer substantial advantages over reconstituted lipid membranes and have been used to investigate the structure of membrane protein by EM and atomic force microscopy (Avery et al., 2000; Marasini et al., 2013; Prior et al., 2003; Scheuring et al., 2004). Membrane sheeting techniques, combined with electron tomography, provide unique opportunities for in-situ determination of membrane protein structures in the native environment and thus avoiding the application of biochemical purification procedures and distorting effects of non-native environments.

4.2. In-situ isolation of plasma membrane for cryo-ET

Cryo-ET is so far the only method that allows the visualization of the macromolecular architecture of cells in a near-native state (Baumeister, 2005; Leis et al., 2009). However, the accessible sample thickness has been a fundamental obstacle to

the applicability and the achievable resolution of this method. For the optimal resolution of TEM, the specimen thickness is limited to under 300 nm (Adrian et al., 1984). As a result, cryo-ET structural analysis has been confined to thin cellular specimens as viruses (Bárcena et al., 2009; de Marco et al., 2010; Grünewald et al., 2003), small bacterial cells (Kürner et al., 2005; Khursigara et al., 2008; Zhang et al., 2007), and thin peripheral regions of eukaryotic cells (Han et al., 2008; Koning et al., 2008). For the majority of eukaryotic cells (> 5 µm), preparative techniques such as cryo-sectioning (Al-Amoudi et al., 2004) or FIB milling (Rigort et al., 2010) are required to access structural features hidden deep inside cellular volumes.

Cryo-sectioning technique has been established as a preparation method of producing thin vitrified specimens for visualization by cryo-EM (Al-Amoudi et al., 2005, 2007; Pierson et al., 2010) and cryo-ET (Bouchet-Marquis et al., 2006; Gruska et al., 2008; Hsieh et al., 2006; Masich et al., 2006). Nevertheless, this method is technically challenging, and the samples suffer from disturbing mechanical cutting artifacts primarily from curved sections, crevasses, and substantial compression in the cutting direction (Al-Amoudi et al., 2005; Han et al., 2008; Zhang et al., 2004). These artifacts, especially the potentially inconsistent compression that cannot be quantitatively corrected, result in low yields of quality sections suitable for high-resolution tomography. Cryo-FIB, on the other hand, promises a significant improvement over conventional cryo-sectioning method for cryo-EM studies due to the absence of mechanical deformation (Hayles et al., 2010; Marko et al., 2007; Rigort et al., 2012), but it is typically low throughput and extremely time-consuming (Villa et al., 2013). For large mammalian cells, it can take as much as 4-8 h for thinning a window of approximately the surface of mammalian cells. Moreover, ion-induced structural alterations of ice-embedded biological samples are still poorly understood (Rigort et al., 2010; Rigort and Plitzko, 2015; Schertel et al., 2013; Schaffer et al., 2017).

Another innovative approach to access the inside of the cell is to produce thin membrane sheets by unroofing technique (Avery et al., 2000; Clarke et al., 1975; Heuser, 2000; Mazia et al., 1975; Vacquier, 1975). Several procedures have been reported to obtain membrane sheets, including (i) mechanical stripping procedure by deposing and then removing a glass slide over the cell monolayer (Marasini et al., 2013; Prior et al.,

2003), (ii) shearing-off of the plasma membrane by sonication (Avery et al., 2000; Heuser, 2000), and (iii) lysis of cells by osmotic shock (Hirai et al., 1998). It is a robust and straightforward technique with higher throughput than cryo-sectioning and FIB milling and has produced strikingly high-resolution beautiful images of macromolecules on the plasma membrane (Heuser, 2000). Additionally, compared to isolated proteins or protein in reconstituted bilayers, membrane patches generated directly from cells offer the advantages of studying membrane protein in a detergent-free, near-native environment (Izuta et al., 2017; Perez et al., 2006; Peitsch et al., 2016; Wu and De Camilli, 2012). Furthermore, membrane sheets allow the adding of fiducial markers for the alignment of tomographic tilt series, while in vitreous samples, the alignment is largely through the challenging ‘patch-tracking’ algorithms (Castaño-Díez et al., 2010). Lastly, it enables the study of membrane protein under physiological conditions and the visualization of conformational changes upon ligand binding.

4.3. Challenges in membrane patch preparation

In our studies, cells attached to the EM grids were opened with a shearing force either by sonication or the paper-blotting method. These procedures removed the top of cells, after which most organelles in the cytoplasm, including the nucleus, Golgi, and ER were mostly washed away. What remained were the exposed inner adherent plasma membrane and associated proteins. Nevertheless, in the confocal 3D reconstruction images of the cell membrane sheets, occasionally we observed the nucleus and ER remaining attached to the inner plasma membrane after unroofing procedures. These remaining organelles could hinder the following EM experiments; therefore, after unroofing procedures, cell membrane sheets were fluorescently labeled with membrane stain, ER stain, and nuclear stain and validated under the confocal microscope before EM preparation.

Critical factors to consider before unroofing procedures include cell adhesion and confluency. As HEK293 cells are weakly adherent to the carbon-coated EM girds, which can lead to abnormal cell morphology (Mazia et al., 1975), all the EM grids were coated with poly-D-lysine to increase cell adhesion before unroofing procedures. Besides, at the time of membrane sheeting, cell confluency around 80% yields the best monolayer membrane patch production.

The successful sonication of membrane sheets involves fine-tuning of several factors include sonication intensity, sonication duration, and tip distance to the cells. Among these factors, tip distance to the grid is the most challenging to adjust, as even slight variation in each trial can tremendously alter membrane patch yield. On the other hand, the effect of sonication duration is less obvious. In most cases, a pulse duration of 0.5 s is sufficient, while sonication for the second time is occasionally required to increase the membrane patch yield. We also tested the sonication intensity (% of the maximal output power) ranging from 5% to 40% and determined that sonication intensity around 15~20% was the most efficient for generating membrane sheeting without severe damage to the carbon film. The final delivered sonication power is a combination of multiple factors, including tip distance, sonication duration, and intensity. While weak power cannot rupture the plasma membrane, too strong power often leads to fragmentation of the basal membrane, detachment of the adherent cells, and severe damage to the EM grid carbon film. To fine-tuning all the possible sonication settings for each parameter and determine their optimal combination is a time-consuming and tedious process that requires multiple testing and meticulous planning.

In comparison, factors accounting for the membrane patch yield and quality by the paper-blotting method are less complicated, yet still, we needed to test filter-papers with different properties on HEK293 cells, in combination with various blotting times. We found that filter paper isolating good membrane patches shared similar thickness and grammage. While filter papers with a higher grammage tend to dry out, destroy the sample, or even rip off the carbon film, filter papers with a lighter grammage present a much lower rate of successful unroofing. Besides, blotting duration also plays a significant role. Generally, blotting twice yields the best results in terms of membrane patch production. However, the reproducibility of the paper-blotting results is heavily influenced by the investigators' practise; therefore, a less consistent success rate of membrane sheet production by the paper-blotting method was observed than the sonication method.

In conclusion, we have shown that with the sonication and paper-blotting methods, cells directly cultured on EM grids can be unroofed to generate thin membrane patches suitable for structural studies. However, to achieve efficient cell unroofing with good preservation of EM grid carbon film is challenging. As samples varied in cell confluency

and adhesion from batch to batch, experimental settings needed to be optimized for each individual experiment to gain the maximal membrane sheet production. Besides, the practice and experience of the investigators are equally crucial for efficient unroofing.

4.4. QDs as CLEM probes for protein lattice detection

The identification and determination of regions of interest pose an essential challenge to cellular electron tomography. At higher magnification of EM, it becomes increasingly difficult to target specific subcellular features within the crowded cellular landscape. fLM enables fast determination of tagged macromolecules and analysis of their biological roles within living cells, but the resolution is limited to 200 nm on the X-Y plane and 500 nm in the X-Z direction due to the diffraction limit (Heilemann, 2010; Heintzmann and Ficz, 2013; Schermelleh et al., 2010; Wilt et al., 2009). CLEM is an emerging technique that helps bridge the resolution gap between fLM and EM (De Boer et al., 2015; Wolff et al., 2016; Zhang, 2013). Specific labeling with probes that both emit fluorescence and are electron-dense is required for CLME experiments, in which targeted structures identified at the fLM level can be subsequently characterized at high-resolution EM level (Giepmans et al., 2006; Sjollema et al., 2012).

Fluorescent semiconductor nanocrystals, known as QDs, are a class of non-genetically encoded probes commonly used for single-molecular imaging. Compared to other organic dyes, QDs possess intriguing optical properties, including superior brightness, minimal photobleaching, and simultaneous excitation of multiple fluorescence colors. Besides, QDs are electron-dense and directly visible by EM. Due to these unique optical and chemical features, QDs have been developed as a captivating labeling approach for correlative microscopy. The bioconjugation of QDs allows specific labeling of biomolecular in fixed and live cells without compromising biomolecular function (Jaiswal et al., 2003; Lidke et al., 2004; Wu et al., 2003). There are generally two main strategies for bioconjugations of QDs: covalent chemistries and non-covalent binding. The biotin-streptavidin conjugation, based on high-affinity biotin/streptavidin interactions, is likely the most widely used for cellular QD applications, which offers high affinity, stability, and quantitative control of biomolecular valency at the QD surface. On the other hand, covalent chemistries involve a more stable form of reactions, yet one limitation is the lack

of precise control over orientation and stoichiometry of cross-linked biomolecules. The aggregation of QDs is also a concern (Mattoussi et al., 2000; Noh et al., 2010).

In this study, in order to identify and locate protein lattice from the crowded cellular landscapes on the membrane before cryo-ET structural analysis, we utilized the GFP nanobody conjugated QDs for the specific labeling of GFP on the membrane. As the biotin-streptavidin conjugation is inappropriate due to the presence of streptavidin in the protein lattice, we applied the covalent conjugated QD as CLEM probes. After membrane sheeting, the cytosolic leaflet was exposed, which allowed the cytosolic molecules, such as GFP, to be efficiently labeled with GFP nanobody conjugated QDs. We optimized various QD labeling parameters, including the optimal fixation and blocking conditions by fLM, before proceeding with the more time-consuming and laborious EM sample preparation. Our results demonstrated the specific labeling of bioconjugated QD by showing the colocalization of GFP and QDs and obtaining correlative fluorescence and TEM data.

4.5. Design and forming of protein lattice on the membrane

For membrane proteins that present in the context of the heterogeneous plasma membrane with a plethora of membrane proteins, it would be difficult, if not impossible, to locate the target proteins. Additionally, the resolution that can be achieved in a single tomogram of a biological specimen is extremely low. Therefore, the strategy of generating a structured protein lattice on the membrane will not only aid in the detection of the targeted proteins but also obtaining density maps of targeted macromolecule at significantly higher SNR by 3D averaging algorithms.

4.5.1. Intein-based protein trans-splicing

Protein trans-splicing by split intein has become a routine protein engineering strategy. During trans-splicing reactions, the intein domain excises itself from the precursor protein and ligates its N- and C-terminal flanking sequences (termed extein) without any exogenous cofactor or energy sources such as ATP. When the two split intein precursors are co-expressed, trans-splicing can occur upon the association of the two domains, thus opening an avenue for performing protein engineering in vivo (Paulus, 2000;

Topilina and Mills, 2014). Naturally split DnaE inteins from *Nostoc punctiforme*, including *Ssp* DnaE intein and *Npu* DnaE intein, are commonly used and exhibit efficient ligation kinetics (Ellilä et al., 2011; Iwai et al., 2006).

In our experiments, we utilized an optimized intein system to cross-link channels into a structured lattice on the membrane. In this system, the intein is to link a tetrameric channel via their carboxy-terminus to a tetrameric modified streptavidin. To optimize trans-splicing efficiency, we tested the trans-splicing reaction of both *Npu* DnaE and *Ssp* DnaE in HEK293 cells and found *Npu* DnaE intein exhibited more robust trans-splicing efficiency than *Ssp* DnaE intein. Besides their intrinsic splicing kinetics, extein residues near the junction site also play a unique role in the protein trans-splicing efficiency. One possible assumption is that N- and C-extein sequences near the splicing junction site are likely to be involved in the active structural rearrangement during protein trans-splicing. Sequence alignment of both inteins showed N-terminal fragment (Int_N) of *Npu* DnaE intein is 21 amino acids shorter than that of *Ssp* DnaE intein. This flexibility of shorter N-terminal fragment might contribute to the higher tolerance of varying DnaE C-terminal fragment (Int_C) in *Npu* DnaE intein mediated trans-splicing reaction, as evidenced by random substitution studies (Cheriyan et al., 2013).

4.5.2. Optimized split GFP reporter for protein lattice labeling

To facilitate the detection of trans-splicing reactions, therefore, the successful formation of protein lattice on the membrane, we have generated two variants of split GFP reporters, namely the split sfGFP and split EGFP complementation system. Reconstitution assay in HEK293 cells showed split sfGFP possessed more enhanced reconstitution efficiency compared to split EGFP. Multiple factors influence split protein reconstitution efficiency, including split protein structure, chromophore maturation, and photophysical properties. Sequence alignment showed that sfGFP incorporated the ‘cycle-3’ mutations (F99S, M153T, V163A) (Crameri et al., 1995) and six other critical mutations (S30R, Y39I, N105K, Y145F, I171V, and A206V) compared to folding reporter GFP that led to enhanced fluorescent signals and robust protein folding (Cabantous et al., 2005; Chudakov et al., 2010; Pédelacq et al., 2006; Romei and Boxer, 2019). X-ray crystallographic studies revealed S30R contributed significantly to sfGFP folding fluorescence by mediating the five-membered intramolecular ion-pair network formation (E32–R30-E17–R122–E115)

that increased global structural stability (Pédelacq et al., 2006). Moreover, the split scheme also played an essential role in folding efficiency. While EGFP was split between the 7th and 8th β-strand, sfGFP was split at the 11th β-strand, yielding a 214-residue N-terminal fragment (GFP1-10) and a 17-residue C-terminal fragment (GFP11). The small size of the GFP11 tag minimizes perturbation to the tagged proteins and thus improves the solubility and folding significantly, making it a more reliable tool for cell labeling and trafficking experiments (Baird et al., 1999).

4.5.3. Design and functionality of fusion protein linkers

For the construction of stable, bioactive protein lattice, fusion protein linkers are indispensable components to consider. The inserted linkers can reduce the interference between functional domains and improve protein folding, whereas direct fusion of proteins without a linker may lead to protein misfolding (Zhao et al., 2008) or impaired bioactivity (Bai et al., 2005; Bai and Shen, 2006). The design of a linker often requires thorough consideration in order to maximize the flexibility and folding stability of fusion proteins. Both the linker length and sequence composition have a significant effect on the folding stability and bioactivity of fusion proteins (Robinson and Sauer, 1998). Depending on the biological applications, linkers can be classified into three main categories: flexible linkers, rigid linkers, and in vivo cleavable linkers. The flexible linkers generally consist of small or polar amino acids, such as Gly and Ser, to provide excellent flexibility and solubility. Rigid linkers generally adopt α-helical structure with pro-rich sequences and are applied when sufficient separation of protein domains is required. Cleavable linker, on the other hand, allows the cleavage of the function domain via the reduction of the disulfide bond, or by proteases.

In our study, we utilized a flexible GS linker to bridge the HCN1 and GFP_N and adjusted the linker length according to the distance between the C-terminus of HCN1 to N-terminus of GFP_N under its natural orientation (1.2 nm). Assuming the length of GGS is 0.5 nm, the length of $(GGS)_6$ would allow for proper protein folding and optimal biological activity of the functional domains. Similarly, a $(GGS)_6$ linker was also applied to bridge GFPc and streptavidin subunit.

4.6. Outlook

The need to map biological systems at scales extending from organisms to atoms makes integrative methods indispensable. A unified method is required that is capable of navigating cellular landscapes (e.g., correlative microscopy), preparing thin cellular specimens (e.g., micromachining by FIB milling or unroofing techniques), acquiring structural information (e.g., electron tomography), and analyzing complex cellular volumes (computational methods). This study successfully combines various techniques into a robust and reliable workflow for in situ structural studies of membrane proteins.

In CLEM experiments, we have achieved reasonably accurate subcellular spatial correlations between LM/EM modalities. However, the lower spatial resolution of fLM (<200 nm) limits the degree to which we can specify that a fluorescent signal corresponds to a specific structure within an overlayed LM/EM image. To this end, super-resolution CLEM, which combines CLEM with super-resolution microscopy techniques, is currently under development to overcome this diffraction limit and achieve correlation at 20-nm resolution (Sochacki et al., 2014). This super-resolution CLEM technique will provide a promising new avenue to identify fluorescently labeled molecules within the cellular structural context with high precision (Arnold et al., 2016; Chang et al., 2014; Liu et al., 2015; van Elsland et al., 2018; Wolff et al., 2016).

Another limitation of this study is sample preparation at RT, which can result in structural deformation between LM/EM imaging modes that renders the precise image correlation more difficult. In order to reduce the artifacts associated with conventional EM preparation (Murk et al., 2003), structural biologists combine CLEM with fast freezing techniques to keep the vitrified samples remaining consistent during images at LM and EM stages, which ensures that no artifacts are introduced during the sample processing. Besides, cryo-immobilization also helps the preservation of ultrastructure in a close-to-native state for subsequent cryo-ET studies (Plitzko et al., 2009).

Correlative cryo-ET is another breakthrough innovation in electron microscopy. Although the combination of CLEM with electron tomography is challenging, it enables in situ high-resolution structural determination (Lucic et al., 2007; Plitzko et al., 2009; Sartori et al., 2007; Schwartz et al., 2007). In this study, correlative cryo-ET can be employed to map the high-resolution structure of the HCN1 lattice on the membrane. Moreover,

tomographic studies of membrane sheets enable the visualization of the HCN1 structural response induced by pharmacological manipulations (Fernández-Busnadiego et al., 2010). It is expected that with computational and technical developments, such as automatic correlation system and rapid transfer system for high-pressure freezing, correlative cryo-ET will find widespread use in studying protein structure-function relationships in the native cellular environment and bridge the resolution gap between light microscopy and atomic-resolution methods such as X-ray crystallography and single-particle EM.

5. Abstract

Hyperpolarized-activated cyclic nucleotide-gated (HCN) channels play complex and diverse roles in the regulation of neuronal and network excitability. Aberrant expression, trafficking, and post-translational modifications of HCN1 channels contribute to the experimental and human epilepsy, yet the structural basis underpinning the altered function is still unknown. To unravel the structure-function relationship of HCN1 channels in the native cellular environment, we utilized an optimized intein system to cross-link channels into a structured lattice on the membrane. The successful forming of HCN1 lattice on the membrane was evidenced by split GFP reconstitution and functionally characterized by electrophysiological recording. We subsequently generated membrane sheets suitable for structural EM analysis directly from cells expressing protein lattices by unroofing techniques. The membrane sheets were then fluorescent- and immunolabeled with GFP nanobody conjugated quantum dot, which allowed the detection of protein lattice for correlative light and electron microscopy experiments. Compared to structural studies in membrane mimetic environments, this study provides invaluable opportunities for in situ structural determination of membrane protein in the native membrane environment.

6. List of Figures

7. List of Tables

8. Bibliography

Abdul-Hussein S, Andréll J, Tate CG. Thermostabilisation of the serotonin transporter in a cocaine-bound conformation. J Mol Biol 2013; 425:2198–2207

Adrian M, Dubochet J, Lepault J, McDowall AW. Cryo-electron microscopy of viruses. Nature 1984; 308:32–36

Afonine P V., Grosse-Kunstleve RW, Echols N, Headd JJ, Moriarty NW, Mustyakimov M, Terwilliger TC, Urzhumtsev A, Zwart PH, Adams PD. Towards automated crystallographic structure refinement with phenix.refine. Acta Crystallogr Sect D Biol Crystallogr 2012; 68:352–367

Al-Amoudi A, Chang JJ, Leforestier A, McDowall A, Salamin LM, Norlén LPO, Richter K, Blanc NS, Studer D, Dubochet J. Cryo-electron microscopy of vitreous sections. EMBO J 2004; 23:3583–3588

Al-Amoudi A, Díez DC, Betts MJ, Frangakis AS. The molecular architecture of cadherins in native epidermal desmosomes. Nature 2007; 450:832–837

Al-Amoudi A, Studer D, Dubochet J. Cutting artefacts and cutting process in vitreous sections for cryo-electron microscopy. J Struct Biol 2005; 150:109–121

Alonso A, Llinás RR. Subthreshold Na+-dependent theta-like rhythmicity in stellate cells of entorhinal cortex layer II. Nature 1989; 342:175–177

Amunts A, Brown A, Bai XC, Llácer JL, Hussain T, Emsley P, Long F, Murshudov G, Scheres SHW, Ramakrishnan V. Structure of the yeast mitochondrial ribosome. Science 2017; 355:528–531

Andersen AH, Kak AC. Simultaneous algebraic reconstruction technique (SART): A superior implementation of the art algorithm. Ultrason Imaging 1984; 6:81–94

Arnold J, Mahamid J, Lucic V, De Marco A, Fernandez JJ, Laugks T, Mayer T, Hyman AA, Baumeister W, Plitzko JM. Site-Specific Cryo-focused Ion Beam Sample Preparation Guided by 3D Correlative Microscopy. Biophys J 2016; 110:860–869

Assenberg R, Wan PT, Geisse S, Mayr LM. Advances in recombinant protein expression for use in pharmaceutical research. Curr Opin Struct Biol 2013; 23:393–402

Atherton JF, Kitano K, Baufreton J, Fan K, Wokosin D, Tkatch T, Shigemoto R, Surmeier DJ, Bevan MD. Selective participation of somatodendritic HCN channels in inhibitory but not excitatory synaptic integration in neurons of the subthalamic nucleus. J Neurosci 2010; 30:16025–16040

Avery J, Ellis DJ, Lang T, Holroyd P, Riedel D, Henderson RM, Edwardson JM, Jahn R. A cell-free system for regulated exocytosis in PC12 cells. J Cell Biol 2000; 148:317–324

Bai X chen, McMullan G, Scheres SHW. How cryo-EM is revolutionizing structural biology. Trends Biochem Sci 2015; 40:49–57

Bai Y, Ann DK, Shen WC. Recombinant granulocyte colony-stimulating factor-transferrin fusion protein as an oral myelopoietic agent. Proc Natl Acad Sci U S A 2005; 102:7292–7296

Bai Y, Shen WC. Improving the oral efficacy of recombinant granulocyte colony-stimulating factor and transferrin fusion protein by spacer optimization. Pharm Res 2006; 23:2116–2121

Baird GS, Zacharias DA, Tsien RY. Circular permutation and receptor insertion within green fluorescent proteins. Proc Natl Acad Sci U S A 1999; 96:11241–11246

Balch WE, McCaffery JM, Plutner H, Farquhar MG. Vesicular stomatitis virus glycoprotein is sorted and concentrated during export from the endoplasmic reticulum. Cell 1994; 76:841–852

Bárcena M, Oostergetel GT, Bartelink W, Faas FGA, Verkleij A, Rottier PJM, Koster AJ, Bosch BJ. Cryo-electron tomography of mouse hepatitis virus: Insights into the structure of the coronavirion. Proc Natl Acad Sci U S A 2009; 106:582–587

Baumeister W. From proteomic inventory to architecture. FEBS Lett 2005; 579:933–937

Beck M, Malmström JA, Lange V, Schmidt A, Deutsch EW, Aebersold R. Visual proteomics of the human pathogen Leptospira interrogans. Nat Methods 2009; 6:817–823

Bender RA, Soleymani S V., Brewster AL, Nguyen ST, Beck H, Mathern GW, Baram TZ. Enhanced expression of a specific hyperpolarization-activated cyclic nucleotide-

gated cation channel (HCN) in surviving dentate gyrus granule cells of human and experimental epileptic hippocampus. J Neurosci 2003; 23:6826–6836

Berger T, Larkum ME, Lüscher HR. High Ih channel density in the distal apical dendrite of layer V pyramidal cells increases bidirectional attenuation of EPSPs. J Neurophysiol 2001; 85:855–868

Betzig E, Patterson GH, Sougrat R, Lindwasser OW, Olenych S, Bonifacino JS, Davidson MW, Lippincott-Schwartz J, Hess HF. Imaging intracellular fluorescent proteins at nanometer resolution. Science 2006; 313:1642–1645

Bezanilla F. The voltage sensor in voltage-dependent ion channels. Physiol Rev 2000; 80:555–592

Biel M, Wahl-Schott C, Michalakis S, Zong X. Hyperpolarization-Activated Cation Channels: From Genes to Function. Physiol Rev 2009; 89:847–885

Blundell TL, Jhoti H, Abell C. High-throughput crystallography for lead discovery in drug design. Nat Rev Drug Discov 2002; 1:45–54

Bolia A, Gerek ZN, Ozkan SB. BP-dock: A flexible docking scheme for exploring protein-ligand interactions based on unbound structures. J Chem Inf Model 2014; 54:913–925

Bouchet-Marquis C, Dubochet J, Fakan S. Cryoelectron microscopy of vitrified sections: A new challenge for the analysis of functional nuclear architecture. Histochem Cell Biol 2006; 125:43–51

Brewster A, Bender RA, Chen Y, Dube C, Eghbal-Ahmadi M, Baram TZ. Developmental Febrile Seizures Modulate Hippocampal Gene Expression of Hyperpolarization-Activated Channels in an Isoform- and Cell-Specific Manner. J Neurosci 2002; 22:4591–4599

Brewster AL, Bernard JA, Gall CM, Baram TZ. Formation of heteromeric hyperpolarization-activated cyclic nucleotide-gated (HCN) channels in the hippocampus is regulated by developmental seizures. Neurobiol Dis 2005; 19:200–207

Cabantous S, Terwilliger TC, Waldo GS. Protein tagging and detection with engineered

self-assembling fragments of green fluorescent protein. Nat Biotechnol 2005; 23:102–107

Caffrey M. Crystallizing Membrane Proteins for Structure Determination: Use of Lipidic Mesophases. Annu Rev Biophys 2009; 38:29–51

Carlson L-AA, de Marco A, Oberwinkler H, Habermann A, Briggs JAGG, Kräusslich H-GG, Grünewald K. Hope TJ, ed Cryo electron tomography of native HIV-1 budding sites. PLoS Pathog 2010; 6:e1001173

Carroni M, Saibil HR. Cryo electron microscopy to determine the structure of macromolecular complexes. Methods 2016; 95:78–85

Castaño-Díez D, Scheffer M, Al-Amoudi A, Frangakis AS. Alignator: A GPU powered software package for robust fiducial-less alignment of cryo tilt-series. J Struct Biol 2010; 170:117–126

Celler K, Koning RI, Willemse J, Koster AJ, Van Wezel GP. Cross-membranes orchestrate compartmentalization and morphogenesis in Streptomyces. Nat Commun 2016; 7:ncomms11836

Chen J, Mitcheson JS, Lin M, Sanguinetti MC. Functional roles of charged residues in the putative voltage sensor of the HCN2 pacemaker channel. J Biol Chem 2000; 275:36465–36471

Chen K, Aradi I, Thon N, Eghbal-Ahmadi M, Baram TZ, Soltesz I. Persistently modified h-channels after complex febrile seizures convert the seizure-induced enhancement of inhibition to hyperexcitability. Nat Med 2001; 7:331–337

Chen M, Dai W, Sun SY, Jonasch D, He CY, Schmid MF, Chiu W, Ludtke SJ. Convolutional neural networks for automated annotation of cellular cryo-electron tomograms. Nat Methods 2017; 14:983–985

Cheng Y, Grigorieff N, Penczek PA, Walz T. A primer to single-particle cryo-electron microscopy. Cell 2015; 161:438–449

Cherezov V. Crystallizing membrane proteins using lipidic mesophases. Nat Protoc 2009; 4:706–731

Cheriyan M, Pedamallu CS, Tori K, Perler F. Faster protein splicing with the nostoc

punctiforme DnaE intein using non-native extein residues. J Biol Chem 2013; 288:6202–6211

Chudakov DM, Matz M V., Lukyanov S, Lukyanov KA. Fluorescent proteins and their applications in imaging living cells and tissues. Physiol Rev 2010; 90:1103–1163

Chun E, Thompson AA, Liu W, Roth CB, Griffith MT, Katritch V, Kunken J, Xu F, Cherezov V, Hanson MA, Stevens RC. Fusion partner toolchest for the stabilization and crystallization of G protein-coupled receptors. Structure 2012; 20:967–976

Clarke M, Schatten G, Mazia D, Spudich JA. Visualization of actin fibers associated with the cell membrane in amoebae of Dictyostelium discoideum. Proc Natl Acad Sci U S A 1975; 72:1758–1762

Conway JF, Trus BL, Booy FP, Newcomb WW, Brown JC, Steven AC. The effects of radiation damage on the structure of frozen hydrated HSV-1 capsids. J Struct Biol 1993; 111:222–233

Crameri A, Whitehorn EA, Tate E, Stemmer WPC. lmproved Green Fluorescent Protein DNA Shuffling. 1995:315–319

Craven KB, Zagotta WN. CNG AND HCN CHANNELS: Two Peas, One Pod. Annu Rev Physiol 2006; 68:375–401

Cross TA, Sharma M, Yi M, Zhou HX. Influence of solubilizing environments on membrane protein structures. Trends Biochem Sci 2011; 36:117–125

D'Arcangelo JG, Stahmer KR, Miller EA. Vesicle-mediated export from the ER: COPII coat function and regulation. Biochim Biophys Acta - Mol Cell Res 2013; 1833:2464–2472

Dabov K, Foi A, Katkovnik V, Egiazarian K. Image denoising by sparse 3-D transform-domain collaborative filtering. IEEE Trans Image Process 2007; 16:2080–2095

De Boer P, Hoogenboom JP, Giepmans BNG. Correlated light and electron microscopy: Ultrastructure lights up! Nat Methods 2015; 12:503–513

de Marco A, Müller B, Glass B, Riches JD, Kräusslich HG, Briggs JAG. Structural analysis of HIV-1 maturation using cryo- electron tomography. PLoS Pathog 2010; 6:e1001215

De Planque MRR, Goormaghtigh E, Greathouse D V., Koeppe RE, Kruijtzer JAW,

Liskamp RMJ, De Kruijff B, Killian JA. Sensitivity of single membrane-spanning α-helical peptides to hydrophobic mismatch with a lipid bilayer: Effects on backbone structure, orientation, and extent of membrane incorporation. Biochemistry 2001; 40:5000–5010

De Rosier DJ, Klug A. Reconstruction of three dimensional structures from electron micrographs. Nature 1968; 217:130–134

Deschamps JR. The role of crystallography in drug design. AAPS J 2005; 7:813–819

Dibbens LM, Reid CA, Hodgson B, Thomas EA, Phillips AM, Gazina E, Cromer BA, Clarke AL, Baram TZ, Scheffer IE, Berkovic SF, Petrou S. Augmented currents of an HCN2 variant in patients with febrile seizure syndromes. Ann Neurol 2010; 67:542–546

DiFrancesco D, Tortora P. Direct activation of cardiac pacemaker channels by intracellular cyclic AMP. Nature 1991; 351:145–147

DiFrancesco JC, Barbuti A, Milanesi R, Coco S, Bucchi A, Bottelli G, Ferrarese C, Franceschetti S, Terragni B, Baruscotti M, DiFrancesco D. Recessive loss-of-function mutation in the pacemaker HCN2 Channel causing increased neuronal excitability in a patient with idiopathic generalized epilepsy. J Neurosci 2011; 31:17327–17337

Ding W, You Z, Shen S, Chen L, Zhu S, Mao J. Inhibition of HCN channel activity in the thalamus attenuates chronic pain in rats. Neurosci Lett 2016; 631:97–103

Du L, Wang SJ, Cui J, He WJ, Ruan HZ. The role of HCN channels within the periaqueductal gray in neuropathic pain. Brain Res 2013; 1500:36–44

Dubé C, Richichi C, Bender RA, Chung G, Litt B, Baram TZ. Temporal lobe epilepsy after experimental prolonged febrile seizures: Prospective analysis. Brain 2006; 129:911–922

Egerton RF, McLeod R, Wang F, Malac M. Basic questions related to electron-induced sputtering in the TEM. Ultramicroscopy 2010; 110:991–997

Elokely KM, Doerksen RJ. Docking challenge: Protein sampling and molecular docking performance. J Chem Inf Model 2013; 53:1934–1945

Emsley P, Lohkamp B, Scott WG, Cowtan K. Features and development of Coot. Acta Crystallogr Sect D Biol Crystallogr 2010; 66:486–501

Endo Y, Sawasaki T. Cell-free expression systems for eukaryotic protein production. Curr Opin Biotechnol 2006; 17:373–380

Engelman DM. Crossing the hydrophobic barrier: Insertion of membrane proteins. Science 1996; 274:1850–1851

Evans TC, Martin D, Kolly R, Panne D, Sun L, Ghosh I, Chen L, Benner J, Liu XQ, Xu MQ. Protein trans-splicing and cyclization by a naturally split intein from the dnaE gene of Synechocystis species PCC6803. J Biol Chem 2000; 275:9091–9094

Faas FGA, Bárcena M, Agronskaia A V., Gerritsen HC, Moscicka KB, Diebolder CA, van Driel LF, Limpens RWAL, Bos E, Ravelli RBG, Koning RI, Koster AJ. Localization of fluorescently labeled structures in frozen-hydrated samples using integrated light electron microscopy. J Struct Biol 2013; 181:283–290

Fernández-Busnadiego R, Zuber B, Maurer UE, Cyrklaff M, Baumeister W, Lučić V. Quantitative analysis of the native presynaptic cytomatrix by cryoelectron tomography. J Cell Biol 2010; 188:145–156

Fernandez-Leiro R, Scheres SHW. Unravelling biological macromolecules with cryo-electron microscopy. Nature 2016; 537:339–346

Fernandez JJ, Li S, Bharat TAM, Agard DA. Cryo-tomography tilt-series alignment with consideration of the beam-induced sample motion. J Struct Biol 2018; 202:200–209

Ferreira LG, Dos Santos RN, Oliva G, Andricopulo AD. Molecular docking and structure-based drug design strategies. Molecules 2015; 20:13384–13421

Frank J, Goldfarb W, Eisenberg D, Baker TS. Reconstruction of glutamine synthetase using computer averaging. Ultramicroscopy 1978; 3:283–290

Frauenfeld J, Gumbart J, Sluis EOV Der, Funes S, Gartmann M, Beatrix B, Mielke T, Berninghausen O, Becker T, Schulten K, Beckmann R. Cryo-EM structure of the ribosome-SecYE complex in the membrane environment. Nat Struct Mol Biol 2011; 18:614–621

Frauenfeld J, Löving R, Armache JP, Sonnen AFP, Guettou F, Moberg P, Zhu L, Jegerschöld C, Flayhan A, Briggs JAG, Garoff H, Löw C, Cheng Y, Nordlund P. A saposin-lipoprotein nanoparticle system for membrane proteins. Nat Methods 2016;

13:345–351

Gauss R, Seifert R, Kaupp UB. Molecular identification of a hyperpolarization-activated channel in sea urchin sperm. Nature 1998; 393:583–587

Giepmans BNG, Adams SR, Ellisman MH, Tsien RY. The fluorescent toolbox for assessing protein location and function. Science 2006; 312:217–224

Glaeser RM. Limitations to significant information in biological electron microscopy as a result of radiation damage. J Ultrasructure Res 1971; 36:466–482

Gordon R, Bender R, Herman GT. Algebraic Reconstruction Techniques (ART) for three-dimensional electron microscopy and X-ray photography. J Theor Biol 1970; 29:471–476

Gregor J, Benson T. Computational analysis and improvement of SIRT. IEEE Trans Med Imaging 2008; 27:918–924

Grünewald K, Desai P, Winkler DC, Heymann JB, Belnap DM, Baumeister W, Steven AC. Three-Dimensional Structure of Herpes Simplex Virus from Cryo-Electron Tomography. Science 2003; 302:1396–1398

Gruska M, Medalia O, Baumeister W, Leis A. Electron tomography of vitreous sections from cultured mammalian cells. J Struct Biol 2008; 161:384–392

Gullingsrud J, Schulten K. Lipid Bilayer pressure profiles and mechanosensitive channel gating. Biophys J 2004; 86:3496–3509

Hagen WJH, Wan W, Briggs JAG. Implementation of a cryo-electron tomography tilt-scheme optimized for high resolution subtomogram averaging. J Struct Biol 2017; 197:191–198

Hampton CM, Strauss JD, Ke Z, Dillard RS, Hammonds JE, Alonas E, Desai TM, Marin M, Storms RE, Leon F, Melikyan GB, Santangelo PJ, Spearman PW, Wright ER. Correlated fluorescence microscopy and cryo-electron tomography of virus-infected or transfected mammalian cells. Nat Protoc 2017; 12:150–167

Han HM, Zuber B, Dubochet J. Compression and crevasses in vitreous sections under different cutting conditions. J Microsc 2008; 230:167–171

Han R, Wang L, Liu Z, Sun F, Zhang F. A novel fully automatic scheme for fiducial marker-

based alignment in electron tomography. J Struct Biol 2015; 192:403–417

Hansen SB, Tao X, MacKinnon R. Structural basis of PIP2 activation of the classical inward rectifier K+ channel Kir2.2. Nature 2011; 477:495–498

Hanton SL, Renna L, Bortolotti LE, Chatre L, Stefano G, Brandizzi F. Diacidic motifs influence the export of transmembrane proteins from the endoplasmic reticulum in plant cells. Plant Cell 2005; 17:3081–3093

Hayles MF, Matthijs de Winter DA, Schneijdenberg CTWM, Meeldijk JD, Luecken U, Persoon H, de Water J, de Jong F, Humbel BM, Verkleij AJ. The making of frozen-hydrated, vitreous lamellas from cells for cryo-electron microscopy. J Struct Biol 2010; 172:180–190

He C, Chen F, Li B, Hu Z. Neurophysiology of HCN channels: From cellular functions to multiple regulations. Prog Neurobiol 2014; 112:1–23

Heilemann M. Fluorescence microscopy beyond the diffraction limit. J Biotechnol 2010; 149:243–251

Heintzmann R, Ficz G. Breaking the resolution limit in light microscopy. In: Prescott DM, ed. Methods in Cell Biology, 1st ed. Academic press, 2013: 525–544

Hell SW, Wichmann J. Breaking the diffraction resolution limit by stimulated emission: stimulated-emission-depletion fluorescence microscopy. Opt Lett 1994; 19:780–782

Henderson R. The Potential and Limitations of Neutrons, Electrons and X-Rays for Atomic Resolution Microscopy of Unstained Biological Molecules. Q Rev Biophys 1995; 28:171–193

Heuser J. The production of “cell cortices” for light and electron microscopy. Traffic 2000; 1:545–552

Hille B. Ionic Channels of Excitable Membranes. Oxford University Press, 1992

Hirai N, Sonobe S, Hayashi T. In situ synthesis of β-glucan microfibrils on tobacco plasma membrane sheets. Proc Natl Acad Sci U S A 1998; 95:15102–15106

Hsieh CE, Leith AD, Mannella CA, Frank J, Marko M. Towards high-resolution three-dimensional imaging of native mammalian tissue: Electron tomography of frozen-hydrated rat liver sections. J Struct Biol 2006; 153:1–13

Hu H, Vervaeke K, Graham LJ, Storm JF. Complementary theta resonance filtering by two spatially segregated mechanisms in CA1 hippocampal pyramidal neurons. J Neurosci 2009; 29:14472–14483

Huang Z, Walker MC, Shah MM. Loss of dendritic HCN1 subunits enhances cortical excitability and epileptogenesis. J Neurosci 2009; 29:10979–10988

Hunte C. Specific protein-lipid interactions in membrane proteins. Biochem Soc Trans 2005; 33:938–942

Ishii TM, Takano M, Ohmori H. Determinants of activation kinetics in mammalian hyperpolarization-activated cation channels. J Physiol 2001; 537:93–100

Iwai H, Züger S, Jin J, Tam PH. Highly efficient protein trans-splicing by a naturally split DnaE intein from Nostoc punctiforme. FEBS Lett 2006; 580:1853–1858

Izuta S, Yamaguchi S, Misawa R, Yamahira S, Tan M, Kawahara M, Suzuki T, Takagi T, Sato K, Nakamura M, Nagamune T, Okamoto A. Microfluidic preparation of anchored cell membrane sheets for in vitro analyses and manipulation of the cytoplasmic face. Sci Rep 2017; 7:14962

Jaiswal JK, Mattoussi H, Mauro JM, Simon SM. Long-term multiple color imaging of live cells using quantum dot bioconjugates. Nat Biotechnol 2003; 21:47–51

Jiang Y, Ruta V, Chen J, Lee A, MacKinnon R. The principle of gating charge movement in a voltage-dependent K+ channel. Nature 2003; 423:42–48

Jorgensen WL. The Many Roles of Computation in Drug Discovery. Science 2004; 303:1813–1818

Jung S, Bullis JB, Lau IH, Jones TD, Warner LN, Poolos NP. Downregulation of dendritic HCN channel gating in epilepsy is mediated by altered phosphorylation signaling. J Neurosci 2010; 30:6678–6688

Jung S, Jones TD, Lugo JN, Sheerin AH, Miller JW, D'Ambrosio R, Anderson AE, Poolos NP, Ambrosio RD', Anderson AE, Poolos NP. Progressive dendritic HCN channelopathy during epileptogenesis in the rat pilocarpine model of epilepsy. J Neurosci 2007; 27:13012–13021

Jung S, Warner LN, Pitsch J, Becker AJ, Poolos NP. Rapid loss of dendritic HCN channel

expression in hippocampal pyramidal neurons following status epilepticus. J Neurosci 2011; 31:14291–14295

Kendrew JC, Bodo G, Dintzis HM, Parrish RG, Wyckoff H, Phillips DC. A three-dimensional model of the myoglobin molecule obtained by x-ray analysis. Nature 1958; 181:662–666

Kepp O, Galluzzi L, Lipinski M, Yuan J, Kroemer G. Cell death assays for drug discovery. Nat Rev Drug Discov 2019; 14:901–913

Khursigara CM, Wu X, Zhang P, Lefman J, Subramaniam S. Role of HAMP domains in chemotaxis signaling by bacterial chemoreceptors. Proc Natl Acad Sci U S A 2008; 105:16555–16560

Kim CS, Chang PY, Johnston D. Enhancement of dorsal hippocampal activity by knockdown of hcn1 channels leads to anxiolytic- and antidepressant-like behaviors. Neuron 2012a; 75:503–516

Kim J, Zhao T, Petralia RS, Yu Y, Peng H, Myers E, Magee JC. MGRASP enables mapping mammalian synaptic connectivity with light microscopy. Nat Methods 2012b; 9:96–102

Kitayama M, Miyata H, Yano M, Saito N, Matsuda Y, Yamauchi T, Kogure S. Ih blockers have a potential of antiepileptic effects. Epilepsia 2003; 44:20–24

Koga K, Descalzi G, Chen T, Ko HG, Lu J, Li S, Son J, Kim TH, Kwak C, Huganir RL, Zhao M gao, Kaang BK, Collingridge GL, Zhuo M. Coexistence of two forms of LTP in ACC provides a synaptic mechanism for the interactions between anxiety and chronic pain. Neuron 2015; 85:377–389

Koning RI, Zovko S, Bárcena M, Oostergetel GT, Koerten HK, Galjart N, Koster AJ, Mieke Mommaas A. Cryo electron tomography of vitrified fibroblasts: Microtubule plus ends in situ. J Struct Biol 2008; 161:459–468

Kopek BG, Shtengel G, Xu CS, Clayton DA, Hess HF. Correlative 3D superresolution fluorescence and electron microscopy reveal the relationship of mitochondrial nucleoids to membranes. Proc Natl Acad Sci U S A 2012; 109:6136–6141

Krivák R, Hoksza D. Improving protein-ligand binding site prediction accuracy by

classification of inner pocket points using local features. J Cheminform 2015; 7:12

Kühlbrandt W. The resolution revolution. Science 2014; 343:1443–1444

Kukulski W, Schorb M, Welsch S, Picco A, Kaksonen M, Briggs JAG. Precise, Correlated Fluorescence Microscopy and Electron Tomography of Lowicryl Sections Using Fluorescent Fiducial Markers. In: Thomas M-R, Paul V, eds. Methods in Cell Biology. Academic press, 2012: 235–257

Kupsch A, LANGE A, Hentschel MP, LÜCK S, Schmidt V, GROTHAUSMANN R, Hilger A, Manke I. Missing wedge computed tomography by iterative algorithm DIRECTT. J Microsc 2016; 261:36–45

Kürner J, Frangakis AS, Baumeister W. Cryo-electron tomography reveals the cytoskeletal structure of Spiroplasma melliferum. Science 2005; 307:436–438

Lacapère JJ, Pebay-Peyroula E, Neumann JM, Etchebest C. Determining membrane protein structures: still a challenge! Trends Biochem Sci 2007; 32:259–270

Lee C-H, Mackinnon R. Structures of the human HCN1 hyperpolarization-activated channel HHS Public Access. Cell 2017; 168:111–120

Lee CH, MacKinnon R. Structures of the Human HCN1 Hyperpolarization-Activated Channel. Cell 2017; 168:111-120.e11

Leis A, Rockel B, Andrees L, Baumeister W. Visualizing cells at the nanoscale. Trends Biochem Sci 2009; 34:60–70

Leone V, Marinelli F, Carloni P, Parrinello M. Targeting biomolecular flexibility with metadynamics. Curr Opin Struct Biol 2010; 20:148–154

Li X, Dang S, Yan C, Gong X, Wang J, Shi Y. Structure of a presenilin family intramembrane aspartate protease. Nature 2013; 493:56–61

Lidke DS, Nagy P, Heintzmann R, Arndt-Jovin DJ, Post JN, Grecco HE, Jares-Erijman EA, Jovin TM. Quantum dot ligands provide new insights into erbB/HER receptor-mediated signal transduction. Nat Biotechnol 2004; 22:198–203

Lingwood D, Simons K. Lipid rafts as a membrane-organizing principle. Science 2010; 327:46–50

Liu Q, Dahmane T, Zhang Z, Assur Z, Brasch J, Shapiro L, Mancia F, Hendrickson WA. Structures from anomalous diffraction of native biological macromolecules. Science 2012; 336:1033–1037

Loerke J, Giesebrecht J, Spahn CMT. Multiparticle Cryo-EM of Ribosomes. In: Abeison J, Simon M, Verdine G, Pyle A, eds. Methods in Enzymology. Academic press, 2010: 161–177

Long SB, Tao X, Campbell EB, MacKinnon R. Atomic structure of a voltage-dependent K+ channel in a lipid membrane-like environment. Nature 2007; 450:376–382

Lu GJ, Tian Y, Vora N, Marassi FM, Opella SJ. The structure of the mercury transporter MerF in phospholipid bilayers: A large conformational rearrangement results from N-terminal truncation. J Am Chem Soc 2013; 135:9299–9302

Ludwig A, Budde T, Stieber J, Moosmang S, Wahl C, Holthoff K, Langebartels A, Wotjak C, Munsch T, Zong X, Feil S, Feil R, Lancel M, Chien KR, Konnerth A, Pape HC, Biel M, Hofmann F. Absence epilepsy and sinus dysrhythmia in mice lacking the pacemaker channel HCN2. EMBO J 2003; 22:216–224

Ludwig A, Zong X, Jeglitsch M, Hofmann F, Biel M. A family of hyperpolarization-activated mammalian cation channels. Nature 1998; 393:587–591

Lupica CR, Bell JA, Hoffman AF, Watson PL. Contribution of the hyperpolarization-activated current (Ih) to membrane potential and GABA release in hippocampal interneurons. J Neurophysiol 2001; 86:261–268

Macalino SJY, Gosu V, Hong S, Choi S. Role of computer-aided drug design in modern drug discovery. Arch Pharm Res 2015; 38:1686–1701

MacRi V, Angoli D, Accili EA. Architecture of the HCN selectivity filter and control of cation permeation. Sci Rep 2012; 2:894

Mahamid J, Pfeffer S, Schaffer M, Villa E, Danev R, Cuellar LK, Förster F, Hyman AA, Plitzko JM, Baumeister W. Visualizing the molecular sociology at the HeLa cell nuclear periphery. Science 2016; 351:969–972

Marcelin B, Chauvière L, Becker A, Migliore M, Esclapez M, Bernard C. h channel-dependent deficit of theta oscillation resonance and phase shift in temporal lobe

epilepsy. Neurobiol Dis 2009; 33:436–447

Marcin B, John J. C, Alexander S, Ulrike W, Rainer H, Felipe EZ, Dirk F, Thorsten L, Reinhard J. A Novel Site of Action for α-SNAP in the SNARE Conformational Cycle Controlling Membrane Fusion. Mol Biol Cell 2007; 18:3250–3263

Marko M, Hsieh C, Schalek R, Frank J, Mannella C. Focused-ion-beam thinning of frozen-hydrated biological specimens for cryo-electron microscopy. Nat Methods 2007; 4:215–217

Masich S, Östberg T, Norlén L, Shupliakov O, Daneholt B. A procedure to deposit fiducial markers on vitreous cryo-sections for cellular tomography. J Struct Biol 2006; 156:461–468

Mathai JC, Sprott GD, Zeidel ML. Molecular Mechanisms of Water and Solute Transport across Archaebacterial Lipid Membranes. J Biol Chem 2001; 276:27266–27271

Mattoussi H, Matthew Mauro J, Goldman ER, Anderson GP, Sundar VC, Mikulec F V., Bawendi MG. Self-assembly of CdSe-ZnS quantum dot bioconjugates using an engineered recombinant protein. J Am Chem Soc 2000; 122:12142–12150

Mazia D, Schatten G, Sale W. Adhesion of cells to surfaces coated with polylysine: Applications to electron microscopy. J Cell Biol 1975; 66:198–200

McPherson A, Gavira JA. Introduction to protein crystallization. Acta Crystallogr Sect FStructural Biol Commun 2014; 70:2–20

Mesirca P et al. Cardiac arrhythmia induced by genetic silencing of “funny” (f) channels is rescued by GIRK4 inactivation. Nat Commun 2014; 5:4664

Miao J, Ercius P, Billinge SJL. Atomic electron tomography: 3D structures without crystals. Science 2016; 353:aaf2157

Moosmang S, Biel M, Hofmann F, Ludwig A. Differential distribution of four hyperpolarization-activated cation channels in mouse brain. Biol Chem 1999; 380:975–980

Moosmang S, Stieber J, Zong X, Biel M, Hofmann F, Ludwig A. Cellular expression and functional characterization of four hyperpolarization-activated pacemaker channels in cardiac and neuronal tissues. Eur J Biochem 2001; 268:1646–1652

Moraes I, Evans G, Sanchez-Weatherby J, Newstead S, Stewart PDS. Membrane protein structure determination - The next generation. Biochim Biophys Acta - Biomembr 2014; 1838:78–87

Moser MB, Rowland DC, Moser EI. Place cells, grid cells, and memory. Cold Spring Harb Perspect Biol 2015; 7:a021808

Murk JLAN, Posthuma G, Koster AJ, Geuze HJ, Verkleij AJ, Kleijmeer MJ, Humbel BM. Influence of aldehyde fixation on the morphology of endosomes and lysosomes: Quantitative analysis and electron tomography. J Microsc 2003; 212:81–90

Murray CW, Blundell TL. Structural biology in fragment-based drug design. Curr Opin Struct Biol 2010; 20:497–507

Nakane T, Kimanius D, Lindahl E, Scheres SHW. Characterisation of molecular motions in cryo-EM single-particle data by multi-body refinement in RELION. Elife 2018

Natesh R. Crystallography beyond Crystals: PX and SPCryoEM. Resonance 2014; 19:1177–1196

Negami T, Shimizu K, Terada T. Coarse-grained molecular dynamics simulations of protein-ligand binding. J Comput Chem 2014; 35:1835–1845

Nichols NM, Evans TC. Mutational Analysis of Protein Splicing, Cleavage, and Self-Association Reactions Mediated by the Naturally Split *Ssp* DnaE Intein. Biochemistry 2004; 43:10265–10276

Noam Y, Bernard C, Baram TZ. Towards an integrated view of HCN channel role in epilepsy. Curr Opin Neurobiol 2011; 21:873–879

Noh M, Kim T, Lee H, Kim CK, Joo SW, Lee K. Fluorescence quenching caused by aggregation of water-soluble CdSe quantum dots. Colloids Surfaces A Physicochem Eng Asp 2010; 359:39–44

Nolan M, Malleret G, Dudman J, Buhi D, Santoro B, Gibbs E, S V, Buzsáki G, Sigegelbaum S, Kandel E, Morozov A. A Behavioral Role for Dendritic IntegrationHCN1 Channels Constrain Spatial Memory and Plasticity at Inputs to Dendrites of CA1 Pyramidal Neurons. Cell 2005; 119:719–732

Nolan M, Malleret G, Dudman J, Buhl D, Santoro B, Gibbs E, Vronskaya S, Buzsaki G,

Siegelbaum S, Kandel E. Constraining the function of CA1 in associative memory models of the hippocampus. Cell 2004; 119:719–732

Notomi T, Shigemoto R. Immunohistochemical Localization of Ih Channel Subunits, HCN1-4, in the Rat Brain. J Comp Neurol 2004; 471:241–276

Nymeyer H, Zhou HX. A method to determine dielectric constants in nonhomogeneous systems: Application to biological membranes. Biophys J 2008; 94:1185–1193

Okamoto T, Harnett MT, Morikawa H. Hyperpolarization-activated cation current (Ih) is an ethanol target in midbrain dopamine neurons of mice. J Neurophysiol 2006; 95:619–626

Pan Y, Laird JG, Yamaguchi DM, Baker SA. An N-terminal ER export signal facilitates the plasma membrane targeting of HCN1 channels in photoreceptors. Investig Ophthalmol Vis Sci 2015; 56:3514–3521

Paulus H. Protein Splicing and Related Forms of Protein Autoprocessing. Annu Rev Biochem 2000; 69:447–496

Pédelacq JD, Cabantous S, Tran T, Terwilliger TC, Waldo GS. Engineering and characterization of a superfolder green fluorescent protein. Nat Biotechnol 2006; 24:79–88

Peitsch CF, Beckmann S, Zuber B. iMEM: Isolation of Plasma Membrane for Cryoelectron Microscopy. Structure 2016; 24:2198–2206

Perez JB, Martinez KL, Segura JM, Vogel H. Supported cell-membrane sheets for functional fluorescence imaginig of membrane proteins. Adv Funct Mater 2006; 16:306–312

Perilla JR, Beckstein O, Denning EJ, Woolf TB. Computing ensembles of transitions from stable states: Dynamic importance sampling. J Comput Chem 2011; 32:196–209

Perlmutter JD, Drasler WJ, Xie W, Gao J, Popot JL, Sachs JN. All-atom and coarse-grained molecular dynamics simulations of a membrane protein stabilizing polymer. Langmuir 2011; 27:10523–10537

Pierson J, Fernández JJ, Bos E, Amini S, Gnaegi H, Vos M, Bel B, Adolfsen F, Carrascosa JL, Peters PJ. Improving the technique of vitreous cryo-sectioning for cryo-electron

tomography: Electrostatic charging for section attachment and implementation of an anti-contamination glove box. J Struct Biol 2010; 169:219–225

Plitzko JM, Rigort A, Leis A. Correlative cryo-light microscopy and cryo-electron tomography: from cellular territories to molecular landscapes. Curr Opin Biotechnol 2009; 20:83–89

Poolos NP, Migliore M, Johnston D. Pharmacological upregulation of h-channels reduces the excitability of pyramidal neuron dendrites. Nat Neurosci 2002; 5:767–774

Postea O, Biel M. Exploring HCN channels as novel drug targets. Nat Rev Drug Discov 2011; 10:903–914

Postis V, Rawson S, Mitchell JK, Lee SC, Parslow RA, Dafforn TR, Baldwin SA, Muench SP. The use of SMALPs as a novel membrane protein scaffold for structure study by negative stain electron microscopy. Biochim Biophys Acta - Biomembr 2015; 1848:496–501

Powell KL, Ng C, O'Brien TJ, Xu SH, Williams DA, Foote SJ, Reid CA. Decreases in HCN mRNA expression in the hippocampus after kindling and status epilepticus in adult rats. Epilepsia 2008; 49:1686–1695

Prior IA, Muncke C, Parton RG, Hancock JF. Direct visualization of ras proteins in spatially distinct cell surface microdomains. J Cell Biol 2003; 160:165–170

Prole DL, Yellen G. Reversal of HCN channel voltage dependence via bridging of the S4-S5 linker and post-S6. J Gen Physiol 2006; 128:273–282

Radermacher M. Three-Dimensional reconstruction of single particles from random and nonrandom tilt series. J Electron Microsc Tech 1988; 9:359–394

Rhee JM, Pirity MK, Lackan CS, Long JZ, Kondoh G, Takeda J, Hadjantonakis AK. In vivo imaging and differential localization of lipid-modified GFP-variant fusions in embryonic stem cells and mice. Genesis 2006; 44:202–218

Rigort A, Bäuerlein FJB, Leis A, Gruska M, Hoffmann C, Laugks T, Böhm U, Eibauer M, Gnaegi H, Baumeister W, Plitzko JM. Micromachining tools and correlative approaches for cellular cryo-electron tomography. J Struct Biol 2010; 172:169–179

Rigort A, Bäuerlein FJB, Villa E, Eibauer M, Laugks T, Baumeister W, Plitzko JM. Focused

ion beam micromachining of eukaryotic cells for cryoelectron tomography. Proc Natl Acad Sci U S A 2012; 109:4449–4454

Rigort A, Plitzko JM. Cryo-focused-ion-beam applications in structural biology. Arch Biochem Biophys 2015; 581:122–130

Robinson CR, Sauer RT. Optimizing the stability of single-chain proteins by linker length and composition mutagenesis. Proc Natl Acad Sci U S A 1998; 95:5929–5934

Robinson RB, Siegelbaum SA. Hyperpolarization-Activated Cation Currents: From Molecules to Physiological Function. Annu Rev Physiol 2003; 65:453–480

Romei MG, Boxer SG. Split Green Fluorescent Proteins: Scope, Limitations, and Outlook. Annu Rev Biophys 2019; 48:19–44

Rust MJ, Bates M, Zhuang X. Sub-diffraction-limit imaging by stochastic optical reconstruction microscopy (STORM). Nat Methods 2006; 3:793–796

Santoro B, Lee JY, Englot DJ, Gildersleeve S, Piskorowski RA, Siegelbaum SA, Winawer MR, Blumenfeld H. Increased seizure severity and seizure-related death in mice lacking HCN1 channels. Epilepsia 2010; 51:1624–1627

Santoro B, Liu DT, Yao H, Bartsch D, Kandel ER, Siegelbaum SA, Tibbs GR. Identification of a gene encoding a hyperpolarization-activated pacemaker channel of brain. Cell 1998; 93:717–729

Sartori A, Gatz R, Beck F, Rigort A, Baumeister W, Plitzko JM. Correlative microscopy: Bridging the gap between fluorescence light microscopy and cryo-electron tomography. J Struct Biol 2007; 160:135–145

Sawasaki T, Ogasawara T, Morishita R, Endo Y. A cell-free protein synthesis system for high-throughput proteomics. Proc Natl Acad Sci U S A 2002; 99:14652–14657

Schaffer M, Mahamid J, Engel BD, Laugks T, Baumeister W, Plitzko JM. Optimized cryo-focused ion beam sample preparation aimed at in situ structural studies of membrane proteins. J Struct Biol 2017; 197:73–82

Scheres SHW, Gao H, Valle M, Herman GT, Eggermont PPB, Frank J, Carazo JM. Disentangling conformational states of macromolecules in 3D-EM through likelihood optimization. Nat Methods 2007; 4:27–29

Schermelleh L, Heintzmann R, Leonhardt H. A guide to super-resolution fluorescence microscopy. J Cell Biol 2010; 190:165–175

Schertel A, Snaidero N, Han HM, Ruhwedel T, Laue M, Grabenbauer M, Möbius W. Cryo FIB-SEM: Volume imaging of cellular ultrastructure in native frozen specimens. J Struct Biol 2013; 184:355–360

Scheuring S, Rigaud JL, Sturgis JN. Variable LH2 stoichiometry and core clustering in native membranes of Rhodospirillum photometricum. EMBO J 2004; 23:4127–4133

Schmid MF, Booth CR. Methods for aligning and for averaging 3D volumes with missing data. J Struct Biol 2008; 161:243–248

Schorb M, Briggs JAG. Correlated cryo-fluorescence and cryo-electron microscopy with high spatial precision and improved sensitivity. Ultramicroscopy 2014; 143:24–32

Schuler MA, Denisov IG, Sligar SG. Nanodiscs as a new tool to examine lipid-protein interactions. In: Kleinschmidt J, ed. Methods in Molecular Biology. Humana, New York, NY, 2019: 645–671

Schur FKM, Obr M, Hagen WJH, Wan W, Jakobi AJ, Kirkpatrick JM, Sachse C, Kräusslich HG, Briggs JAG. An atomic model of HIV-1 capsid-SP1 reveals structures regulating assembly and maturation. Science 2016; 353:506–508

Scott MC, Chen CC, Mecklenburg M, Zhu C, Xu R, Ercius P, Dahmen U, Regan BC, Miao J. Electron tomography at 2.4-ångström resolution. Nature 2012; 483:444–447

Serrano-Vega MJ, Tate CG. Transferability of thermostabilizing mutations between β-adrenergic receptors. Mol Membr Biol 2009; 26:385–396

Shah MM. Cortical HCN channels: Function, trafficking and plasticity. J Physiol 2014; 592:2711–2719

Shah MM, Anderson AE, Leung V, Lin X, Johnston D. Seizure-induced plasticity of h channels in entorhinal cortical layer III pyramidal neurons. Neuron 2004; 44:495–508

Sheldrick GM. A short history of SHELX. Acta Crystallogr Sect A Found Crystallogr 2008; 64:112–122

Shin M, Simkin D, Suyeoka GM, Chetkovich DM. Evaluation of HCN2 abnormalities as a cause of juvenile audiogenic seizures in Black Swiss mice. Brain Res 2006; 1083:14–

20

Simons K, Sampaio JL. Membrane organization and lipid rafts. Cold Spring Harb Perspect Biol 2011; 3:a004697

Sliwoski G, Kothiwale S, Meiler J, Lowe EW. Computational methods in drug discovery. Pharmacol Rev 2014; 66:334–395

Smith JL, Fischetti RF, Yamamoto M. Micro-crystallography comes of age. Curr Opin Struct Biol 2012; 22:602–612

Sochacki KA, Shtengel G, Van Engelenburg SB, Hess HF, Taraska JW. Correlative super-resolution fluorescence and metal-replica transmission electron microscopy. Nat Methods 2014; 11:305–308

Song Y, Nikoloff JM, Zhang D. Improving protein production on the level of regulation of both expression and secretion pathways in Bacillus subtilis. J Microbiol Biotechnol 2015; 25:963–977

Sorzano COS, Messaoudi C, Eibauer M, Bilbao-Castro JR, Hegerl R, Nickell S, Marco S, Carazo JM. Marker-free image registration of electron tomography tilt-series. BMC Bioinformatics 2009; 10:124

Stansfeld PJ, Sansom MSP. Molecular simulation approaches to membrane proteins. Structure 2011; 19:1562–1572

Stark H, Zemlin F, Boettcher C. Electron radiation damage to protein crystals of bacteriorhodopsin at different temperatures. Ultramicroscopy 1996; 63:75–79

Steyaert J, Kobilka BK. Nanobody stabilization of G protein-coupled receptor conformational states. Curr Opin Struct Biol 2011; 21:567–572

Stieber J, Stöckl G, Herrmann S, Hassfurth B, Hofmann F. Functional expression of the human HCN3 channel. J Biol Chem 2005; 280:34635–34643

Surges R, Freiman TM, Feuerstein TJ. Gabapentin increases the hyperpolarization-activated cation current Ih in rat CA1 pyramidal cells. Epilepsia 2003; 44:150–156

Surges R, Kukley M, Brewster A, Rüschenschmidt C, Schramm J, Baram TZ, Beck H, Dietrich D. Hyperpolarization-activated cation current I h of dentate gyrus granule cells is upregulated in human and rat temporal lobe epilepsy. Biochem Biophys Res

Commun 2012; 420:156–160

Tate CG. Practical considerations of membrane protein instability during purification and crystallisation. Methods Mol Biol 2010; 601:187–203

Taylor KA, Glaeser RM. Electron diffraction of frozen, hydrated protein crystals. Science 1974; 186:1036–1037

Terstappen GC, Reggiani A. In silico research in drug discovery. Trends Pharmacol Sci 2001; 22:23–26

Thompson RF, Walker M, Siebert CA, Muench SP, Ranson NA. An introduction to sample preparation and imaging by cryo-electron microscopy for structural biology. Methods 2016

Vaca L, Stieber J, Zong X, Ludwig A, Hofmann F, Biel M. Mutations in the S4 domain of a pacemaker channel alter its voltage dependence. FEBS Lett 2000; 479:35–40

Vacquier VD. The isolation of intact cortical granules from sea urchin eggs: Calcium ions trigger granule discharge. Dev Biol 1975; 43:62–74

Villa E, Schaffer M, Plitzko JM, Baumeister W. Opening windows into the cell: Focused-ion-beam milling for cryo-electron tomography. Curr Opin Struct Biol 2013; 23:771–777

Wahl-Schott C, Biel M. HCN channels: Structure, cellular regulation and physiological function. Cell Mol Life Sci 2009; 66:470–494

Wallin E, Heijne G Von. Genome-wide analysis of integral membrane proteins from eubacterial, archaean, and eukaryotic organisms. Protein Sci 2008; 7:1029–1038

Wan W, Briggs JAG. Cryo-Electron Tomography and Subtomogram Averaging. In: JAbeison J, Simon M, Verdine G, Pyle A, eds. Methods in Enzymology. Academic Press, 2016: 329–367

Wang J, Chen S, Nolan MF, Siegelbaum SA. Activity-dependent regulation of HCN pacemaker channels by cyclic AMP: Signaling through dynamic allosteric coupling. Neuron 2002; 36:451–461

Wang L, Sigworth FJ. Liposomes on a streptavidin crystal. A system to study membrane proteins by cryo-EM. In: Abelson J, Simon M, Verdine G, Pyle A, eds. Methods in

Enzymology. Academic press, 2010: 147–164

Wang S, Li S, Ji G, Huang X, Sun F. Using integrated correlative cryo-light and electron microscopy to directly observe syntaphilin-immobilized neuronal mitochondria in situ. Biophys Reports 2017; 3:8–16

Wildey MJ, Haunso A, Tudor M, Webb M, Connick JH. High-Throughput Screening. In: Robert G, ed. Annual Reports in Medicinal Chemistry, 1st ed. Academic press, 2017

Williams PA, White AM, Clark S, Ferraro DJ, Swiercz W, Staley KJ, Dudek FE. Development of spontaneous recurrent seizures after kainate-induced status epilepticus. J Neurosci 2009; 29:2103–2112

Williams SR. Synchrony and the single neuron. Nat Neurosci 2013; 16:1714–1715

Williams SR, Stuart GJ. Site independence of EPSP time course is mediated by dendritic I(h) in neocortical pyramidal neurons. J Neurophysiol 2000; 83:3177–3182

Wilt BA, Burns LD, Wei Ho ET, Ghosh KK, Mukamel EA, Schnitzer MJ. Advances in Light Microscopy for Neuroscience. Annu Rev Neurosci 2009; 32:435–506

Winkler H, Taylor KA. Marker-free dual-axis tilt series alignment. J Struct Biol 2013; 182:117–124

Winn MD, Ballard CC, Cowtan KD, Dodson EJ, Emsley P, Evans PR, Keegan RM, Krissinel EB, Leslie AGW, McCoy A, McNicholas SJ, Murshudov GN, Pannu NS, Potterton EA, Powell HR, Read RJ, Vagin A, Wilson KS. Overview of the CCP4 suite and current developments. Acta Crystallogr Sect D Biol Crystallogr 2011; 67:235–242

Wolff G, Hagen C, Grünewald K, Kaufmann R. Towards correlative super-resolution fluorescence and electron cryo-microscopy. Biol Cell 2016; 108:245–258

Wu M, De Camilli P. Supported Native Plasma Membranes as Platforms for the Reconstitution and Visualization of Endocytic Membrane Budding. In: Wilson L, Tran P, eds. Methods in Cell Biology. Santa Barbara, Paris: : Elsevier Inc., 2012: 1–18

Wu X, Liu H, Liu J, Haley KN, Treadway JA, Larson JP, Ge N, Peale F, Bruchez MP. Immunofluorescent labeling of cancer marker Her2 and other cellular targets with semiconductor quantum dots. Nat Biotechnol 2003; 21:41–46

Xu R, Chen CC, Wu L, Scott MC, Theis W, Ophus C, Bartels M, Yang Y, Ramezani-Dakhel H, Sawaya MR, Heinz H, Marks LD, Ercius P, Miao J. Three-dimensional coordinates of individual atoms in materials revealed by electron tomography. Nat Mater 2015; 14:1099–1103

Ying SW, Tibbs GR, Picollo A, Abbas SY, Lea Sanford R, Accardi A, Hofmann F, Ludwig A, Goldstein PA. PIP2-mediated HCN3 channel gating is crucial for rhythmic burst firing in thalamic intergeniculate leaflet neurons. J Neurosci 2011; 31:10412–10423

Zagotta WN, Olivier NB, Black KD, Young EC, Olson R, Gouaux E. Structural basis for modulation and agonist specificity of HCN pacemaker channels. Nature 2003; 425:200–205

Zamoon J, Nitu F, Karim C, Thomas DD, Veglia G. Mapping the interaction surface of a membrane protein: Unveiling the conformational switch of phospholamban in calcium pump regulation. Proc Natl Acad Sci U S A 2005; 102:4747–4752

Zhang P. Correlative Cryo-electron Tomography and Optical Microscopy of Cells. Curr Opin Struct Biol 2013; 23:763–770

Zhang P, Khursigara CM, Hartnell LM, Subramaniam S. Direct visualization of Escherichia coli chemotaxis receptor arrays using cryo-electron microscopy. Proc Natl Acad Sci U S A 2007; 104:3777–3881

Zhang R, Xie X. Tools for GPCR drug discovery. Acta Pharmacol Sin 2012; 33:372–384

Zhao HL, Yao XQ, Xue C, Wang Y, Xiong XH, Liu ZM. Increasing the homogeneity, stability and activity of human serum albumin and interferon-α2b fusion protein by linker engineering. Protein Expr Purif 2008; 61:73–77

Zhou H-X, Cross TA. Influences of Membrane Mimetic Environments on Membrane Protein Structures. Annu Rev Biophys 2013; 42:361–392

9. Acknowledgment

First and foremost, I would like to express my deepest gratitude towards my supervisor Prof. Dr. Heinz Beck, for his excellent supervision, unwavering support and tremendous encouragement over the past four years, and not in the least for creating such a nourishing environment for all the group members to thrive and explore the beauty of science. I have been extremely fortunate to have him as my supervisor. Without his unfailing support, the completion of this thesis would have been impossible.

I would also like to extend my sincere appreciation to Prof. Ulrich Benjamin Kaupp, for being my second supervisor and Prof. Dr. Susanne Schoch-McGovern and Prof. Dr. Dirk Dietrich, for being part of the Thesis Committee.

Sincere gratitude also goes to our collaborators: Prof. Dr. Elmar Behrmann for his unparalleled support and insightful advice in this project, Zhuoyan Chen, for his invaluable contribution to EM experiments, and Antje Baumgartner for her laboratory assistance. This research would never reach this far without their generous help and support.

Furthermore, I would like to acknowledge all the members of AG Beck, for contributing critical insights and making my time here so pleasurable and unforgettable. In particular, I would like to extend an enormous ‘thank you’ to Dr. Dominik Holtkamp, who never wavered in his support for the patch-clamp experiments. To Christina Selenz and Lydia Fischer, for great friendships and practical advice. I would further like to acknowledge Margit Reitze, Nicole Schönfelder, and Sabrina Walch for administrative assistance.

Many thanks should also go to AG Schoch, AG Kunz, and AG Mody, especially to Dr. Polina Gulakova and Dr. Balint Szalontai, whose help cannot be underestimated with the molecular biology experiments. I am also grateful for the technical support provided by the Microscopy Core Facility and Nanobodies Core Facility at the University Hospital of Bonn. Last but not least, the support and funding from the Chinese Scholarship Council are genuinely appreciated.

Special thanks to my families, who have been an eternal source of inspiration and happiness for me. I am so grateful for their unconditional love, now and forever.